2021

Electrical Sensing in Non-Excitable Cells to Promote Galvanotaxis and Tissue Survival

Anyesha Sarkar
South Dakota State University

ELECTRICAL SENSING IN NON-EXCITABLE CELLS TO PROMOTE GALVANOTAXIS AND TISSUE SURVIVAL

BY

ANYESHA SARKAR

A dissertation submitted in partial fulfillment of the requirements for the

Doctor of Philosophy

Major in Biological Sciences

Specialization in Biology

South Dakota State University

2021

DISSERTATION ACCEPTANCE PAGE

Anyesha Sarkar

This dissertation is approved as a creditable and independent investigation by a candidate for the Doctor of Philosophy degree and is acceptable for meeting the dissertation requirements for this degree. Acceptance of this does not imply that the conclusions reached by the candidate are necessarily the conclusions of the major department.

Mark Messerli
Advisor Date

Radhey Kaushik
Department Head Date

Nicole Lounsbery, PhD
Director, Graduate School Date

ACKNOWLEDGEMENTS

I am very grateful to my academic advisor Dr. Mark Messerli for his immense patience, sound advice, motivation, and wisdom in training me to be a scientific researcher. I would also like to thank my peers in the lab for constantly providing a nurturing environment for learning and pushing me to do my best. I greatly appreciate the contribution of my co-authors Brian Kobylkevich, Dr. David Graham, Dr. Suman Ranjit, and Brady Carlberg in our publications that helped cement our scientific findings. My graduate committee members, Dr. Michael Hildreth, Dr. Todd Letcher, Late Dr. Donald Auger and Prof. J.D. Ackman have always aided and guided me to take the right course of action throughout my program. Finally, I will be forever indebted to my parents for their monumental sacrifice, motivation and support in pursuing my academic career.

TABLE OF CONTENTS

ABBREVIATIONS

μL	Microliters
μm	Microns
2D	2-Dimensional
3D	3-Dimensional
BFGFR	Basic Fibroblast Growth Factor Receptor
BSA	Bovine Serum Albumin
$CaCl_2$	Calcium Chloride
CHO	Chinese Hamster Ovary
CO2	Carbon Dioxide
ConA	Concanavalin A
DC	Direct Current
DMEM	Dulbecco's Modified Eagle's Medium
e.g.	For Example
ECM	Extracellular Matrix
EEO	Electroendosmosis
EF	Electric Field
EFR	Electric Field Receptor
EGFP	Enhanced Green Fluorescent Protein
EGFR	Epidermal Growth Factor Receptor
EKP	Electrokinetic Perfusion
ENaC	Epithelial Sodium Channel
EOF	Electro-osmotic Flow
EP	Electrophoresis
ES	Electrical Stimulation

ex/em	Excitation/Emission
FBS	Fetal Bovine Serum
FCS	Fluorescence Correlation Spectroscopy
FR	Fish Ringer's
GO	Gene Ontology
HCO_3^-	Bicarbonate Ion
HEPES	4-(2-hydroxyethyl)-1-piperazineethanesulfonic acid
HM	High Molecular
hr(s)	Hour(s)
IACUC	Institutional Animal Care & Use Committee
IL1, IL6, IL8	Interleukins 1, 6 & 8
KCl	Potassium Chloride
kD	kilodalton
K_{ir} 2.1	Inward-Rectifying Potassium channel 2.1
L	Liter
LM	Low Molecular
LSM-FCS	Laser Scanning Microscopy-Fluoresce Correlation Spectroscopy
M	Molar
mA	Milliampere
MC	Methylcellulose
MES	2-(N-morpholino)ethanesulfonic acid
mg	Milligram
min(s)	Minute(s)
mJ/s	Millijoules/Second
ml	Milliliter
mM	Millimolar

mPa•s	Millipascal Seconds
mV/mm	Millivolts/Millimeters
Na^+	Sodium Ion
nAChR	Nicotinic Acetylcholine Receptor
NaCl	Sodium Chloride
nm	Nanometers
PDGF	Platelet Derived Growth Factor
PDP	Pressure-driven perfusion
Pen-Strep	Penicillin-Streptomycin
pHEMA	polyhydroxyethylmethacrylate
PI	Propidium Iodide
PSF	Point Spread Function
RSA	Relative Solvent Accessibility
s	Seconds
SLB	Supported Lipid Bilayers
TAPS	[tris(hydroxymethyl)methylamino]propanesulfonic acid
tdTomato-GPI	Tandem-Dimer Tomato-glycosylphosphatidylinositol
TGFRβ1	Transforming Growth Factor Receptor
TNFα	Tumor Necrosis Factor
Trypsin-EDTA	Ethylenediaminetetraacetic acid
YFP-GPI	Yellow Fluorescent Protein-glycosylphosphatidylinositol

SYMBOLS

%	Percentage
~	Approximately
°C	Degrees Celsius
α	Alpha
β	Beta
±	Plus-Minus
Δ	Delta (change in)
⊕	Mobile Positive Charge

LIST OF FIGURES

LIST OF TABLES

ABSTRACT

ELECTRICAL SENSING IN NON-EXCITABLE CELLS TO PROMOTE GALVANOTAXIS AND TISSUE SURVIVAL

ANYESHA SARKAR

2021

Weak DC fields have been shown to induce polarity, cell migration and cell proliferation in 2D cultures *in vitro*. To understand the mechanism by which non-excitable cells sense such weak EFs, we have investigated the mechanism of cathode-directed water flow (electro-osmosis) in the boundary layer of cells by reducing it with neutral, viscous polymers. Our results indicate that low molecular weight polymers decrease cathodal migration and promote anodal migration in a concentration dependent manner. High molecular weight polymers do not affect directionality and can be explained using porosity and hydraulic permeability between the polymers. These results provide the first evidence for controlled reversal of galvanotaxis using viscous agents.

We present a molecular flux model to describe electromigration of plasma membrane macromolecules and compare its predictions to electromigration of a lipid-anchored surface protein, tdTomato-GPI, under different experimental conditions. We also describe a method for identifying the physical properties of the plasma membrane proteins in zebrafish keratocytes to predict likely candidates for the cell surface electric field receptor that directs cathodal galvanotaxis, and to predict the asymmetric distribution of proteins in other cell types.

In vivo, fluid flow through the vasculature generates mass transfer in the extracellular space and promotes cell proliferation and tissue survival. In the absence of sufficient flow, supply of nutrients and growth factors, and removal of waste products are limited by diffusion, resulting in the development of necrotic tissue. We propose that electrically driven water flow can overcome diffusion by generating interstitial flow to promote viability of the tissue. We have compared the

efficacy of pressure driven perfusion with different types of electrokinetic perfusion toward reducing cell mortality in 3D cultures of Matrigel extracellular matrix. We report that electrokinetic perfusion significantly reduced mortality more consistently than pressure driven perfusion at similar flow rates. We conclude that electrokinetic perfusion has significant advantages over pressure driven perfusion for promoting tissue survival prior to neovascularization and angiogenesis.

INTRODUCTION

Skin is the largest organ of the human body and the first line of defense against disease and pathogens. Skin is composed of epithelial cells that are non-electrically excitable, meaning they do not possess voltage gated channels in their plasma membrane and cannot generate action potentials unlike electrically excitable cells such as muscles or neurons. But, weak endogenous DC electric fields (EFs) have been established as critical components of generating cellular polarity, migration (galvanotaxis) or growth (galvanotropism), embryonic development, tissue and organ regeneration, and epidermal wound healing (Funk, 2015; Levin and Stevenson, 2012; McCaig et al., 2005; Messerli and Graham, 2011; Minc and Chang, 2010; Pu et al., 2015; Robinson and Messerli, 2003a; Wang et al., 1989; Zhao, 2009). These electrical properties have also been manipulated in clinical practice for decades to promote healing of chronic, epidermal wounds by applying brief pulses during electrical stimulation (ES) (Gardner et al., 1999; Frykberg and Banks, 2015; Kloth and Zhao, 2010). However, the mechanism(s) by which these non-electrically excitable cells sense weak EFs remains unknown.

In culture, DC EFs as small as 10 mV/mm, can polarize epithelial and neuronal cells (Hinkle et al., 1981; Huang et al., 2009b; Nishimura et al., 1996; Stump and Robinson, 1983). EFs in the range of 40-200 mV/mm, measured near epidermal wounds (Messerli and Graham, 2011), polarize cells and direct growth and migration of cells and cell sheets most commonly toward the cathode (Cohen et al., 2014; Funk, 2015; Huang et al., 2009a; Nuccitelli, 2004). Electromigration models propose that weak EFs direct cells to the cathode by causing cell surface signaling receptors to accumulate on the cathode side of the cell (McLaughlin and Poo, 1981; Robinson, 1985), resulting in cell structure modification in a manner similar to cell polarization during chemotaxis (McCaig et al., 2005). But there is little understanding of how negatively charged cell surface macromolecules migrate to the negatively charged cathode.

In aqueous solutions, DC EFs electrophorese mobile charge carriers to the pole of opposite charge. This forms the basis for macromolecule separation during gel and capillary electrophoresis. However, adjacent to negatively charged surfaces, like glass capillary tubes (Grossman, 1992) or plasma membranes (McLaughlin and Poo, 1981), the larger number of mobile charge carriers are inorganic cations, like Na^+, which are electrophoresed to the cathode. Electrophoresed cations drag their shells of hydration toward the cathode, resulting in electrically driven water flow, termed electro-osmosis or electro-osmotic flow (EOF). Hundreds of eukaryotic cell types possess negative surface potentials (Mehrishi and Johann, 2002; Slivinsky et al., 1997), leading to cathodal EOF. The electro-osmotic force on surface proteins toward the cathode is proposed to be stronger than the opposing electrophoretic force toward the anode, as many surface proteins accumulate on the cathode side of cells (Brown and Loew, 1994; Fang et al., 1998; Huang et al., 2009a; McLaughlin and Poo, 1981; Orida and Poo, 1978; Poo and Robinson, 1977; Stollberg and Fraser, 1988; Tank et al., 1985; Zhao et al., 1999a) and polarize the cytoplasmic cell motility machinery to the cathode (Pu and Zhao, 2005; Pu et al., 2015; Sato et al., 2009a).

Increasing extracellular viscosity is hypothesized to decrease electromigration of surface proteins whether electrophoresis or electro-osmosis dominates and will decrease EOF directly resulting in random cell migration in applied DC EFs. Despite these predictions, two attempts to impair galvanotaxis by increasing extracellular viscosity using neutral polymers did not affect the direction or speed of cell growth (Jaffe and Poo, 1979) or cell migration (Allen et al., 2013), leading to the conclusion that EOF is not driving cathode-directed galvanotaxis. Considering the size of pores that exist between different sized polymers (Jee et al., 2014), we propose that polymers can alter viscosity in a size dependent manner within the boundary layer near the cell surface where EOF is generated. To test this hypothesis, we have employed a wide range of neutral viscous polymers in attempts to increase viscosity in the boundary layer of cells and influence galvanotaxis.

Next, we wanted to gain greater insight into the dynamics of electromigration to guide our efforts with identifying cell surface macromolecules that act as the putative electric field receptor(s) (EFR), capable of sensing the weak EFs and direct electromigration in multiple cell types. Electromigration of surface macromolecules on cells (Fang et al., 1999; Giugni et al., 1987; Huang et al., 2009b; Huang et al., 2017; Lin et al., 2017; McLaughlin and Poo, 1981; Orida and Poo, 1978; Poo and Robinson, 1977; Yan et al., 2009; Zhao et al., 1999b; Zhao et al., 2002a) and supported lipid bilayers (SLB) (Groves and Boxer, 1995; Han et al., 2009; Liu et al., 2011) is consistent with the electromigration model, where phospholipids with small, charged head groups, electromigrate according to their electrophoretic mobility, and larger, membrane-associated macromolecules that extend outside the lipid bilayer, electromigrate via the combination of their electrophoretic and electro-osmotic mobilities. These findings indicated that the asymmetric distribution of membrane receptors could lead to asymmetric migration toward one of the electrical poles (Patel and Poo, 1982; Stump and Robinson, 1983) based on their physical properties and the properties of their local surroundings (McLaughlin and Poo, 1981).

Therefore, we have derived an electromigration model using net flux of surface macromolecules. We have performed timelapse imaging to monitor electromigration of a fluorescent surface protein in order to predict electromigration of other surface macromolecules and compare them to the time course of cell turning during galvanotaxis. We also describe the size and charge of proteins from the plasma membrane proteome of zebrafish keratocytes to identify candidates for the EFR in this model migratory system.

Water flow promoting cell surface macromolecule redistribution and directed migration led us to investigate the effect of water flow in intercellular spaces and mass transfer in tissues. *In vivo*, mass transfer is performed mostly through blood and lymphatic vessels, and to a lesser extent, interstitial flow occurs in the extracellular space (Swartz and Fleury, 2007). These forms of fluid flow expose cells to gases, nutrients, and growth factors while removing metabolic wastes, cellular

detritus, and death signals. Mass transfer is one of the greatest challenges to tissue engineering in the absence of blood flow (Lovett et al., 2009; Novosel et al., 2011) that can cause degenerative diseases and pose challenges during tissue transplantation when sparse or damaged vessels limit repair and regrowth (Frykberg and Banks, 2015; Novosel et al., 2011; Siemionow and Arslan, 2004). These challenges might be overcome with artificially generated interstitial flow to promote cell survival during periods of neovascularization and angiogenesis that are required for tissue survival.

In the absence of flow, mass transfer is a limiting factor in cell culture when mortality most commonly occurs through starvation (Kroemer and Levine, 2008), stress induced necrosis (Elmore, 2007), or apoptosis in response to hypoxia, metabolically induced low pH, or low growth factors (Elmore, 2007; Grilo and Mantalaris, 2019). Artificial perfusion of media as low as 0.07 μm/s is reported to overcome diffusion limitations in 2D culture and increase cell proliferation by 40% (Park et al., 2011). While pressure promotes perfusion through 3D cell cultures, it also causes compaction of the tissue and increases hydraulic resistance (McCarty and Johnson, 2007; Shi et al., 2009). Charged hydrogels that mimic the native extracellular matrix show greater hydraulic resistance to physiological saline compared to neutral gels (Mattern et al., 2008). Moreover, pressure driven perfusion (PDP) is limited by drag. Therefore, flow velocity through narrow pathways is slow and may be insufficient to promote survival, while the velocity through wider pathways is faster and may damage cells through shear stress. These limitations of pressure driven perfusion may be overcome using electrokinetic perfusion (EKP).

Applied EFs through isotropic, charged gels generate EOF and electrophoresis without gel deformation (Grimshaw et al., 1989; Ou et al., 2014). In 3D tissues, relatively weak EFs generate EOF that is comparable in speed to endogenous velocities of interstitial flow, 0.1-2 μm/s (Garcia et al., 1996; Garcia et al., 2003; Rupert et al., 2013b; Swartz and Fleury, 2007). EOF velocity is more uniform in narrow pathways where PDP is limited by drag. In 3D culture, we hypothesize

that EKP will help cells overcome diffusion limitations and reduce cell mortality. To test this hypothesis, we have induced interstitial flow through 3D cultures in Matrigel, using pressure or electricity. We controlled the average interstitial flow rates in the gels and compared efficacy of the two methods in reducing cell mortality. Our results indicate that steady and intermittent EKP generate interstitial flow and reduce cell mortality.

CHAPTER 1

REVERSING DIRECTION OF GALVANOTAXIS BY CONTROLLED INCREASES IN BOUNDARY LAYER VISCOSITY

ABSTRACT

Weak external electric fields (EFs) polarize cellular structure and direct most migrating cells (galvanotaxis) toward the cathode, making it a useful tool during tissue engineering and healing of epidermal wounds. However, the biophysical mechanisms for sensing weak EFs remain elusive. We have reinvestigated the mechanism of cathode-directed water flow (electro-osmosis) in the boundary layer of cells, by reducing it with neutral, viscous polymers. We report that increasing viscosity with low molecular weight polymers decreases cathodal migration and promotes anodal migration in a concentration dependent manner. In contrast, increased viscosity with high molecular weight polymers does not affect directionality. We explain the contradictory results in terms of porosity and hydraulic permeability between the polymers rather than in terms of bulk viscosity. These results provide the first evidence for controlled reversal of galvanotaxis using viscous agents and position the field closer to identifying the putative electric field receptor, a fundamental, outside-in signaling receptor that controls cellular polarity for different cell types.

INTRODUCTION

Applied EFs are used in clinical practice to promote healing of chronic, epidermal wounds (Frykberg and Banks, 2015; Kloth and Zhao, 2010). The practice is supported by successful clinical trials spanning decades (Gardner et al., 1999) and nonclinical research showing that endogenous DC EFs are critical components of embryonic development, tissue and organ regeneration, and epidermal wound healing (Levin and Stevenson, 2012; McCaig et al., 2005; Messerli and Graham, 2011; Robinson and Messerli, 2003a; Zhao, 2009). Despite its use in the clinic, the mechanism(s) by which non-electrically excitable cells sense weak EFs remains unknown.

In culture, weak DC EFs, in the range of 40-200 mV/mm which have been measured near epidermal wounds (Messerli and Graham, 2011), polarize cells and direct growth and migration of cells and cell sheets most commonly toward the cathode (Cohen et al., 2014; Funk, 2015; Huang et al., 2009a; Nuccitelli, 2004). Weak EFs are thought to direct cells to the cathode by causing cell surface signaling receptors to accumulate on the cathode side of the cell (McLaughlin and Poo, 1981; Robinson, 1985), resulting in cell structure modification in a manner similar to cell polarization during chemotaxis (McCaig et al., 2005). However, there is little understanding of the biophysical mechanism by which negatively charged cell surface macromolecules migrate to the negatively charged cathode.

In aqueous solutions, DC EFs electrophorese mobile charge carriers to the pole of opposite charge, Fig. 1. This forms the basis for macromolecule separation during gel and capillary electrophoresis. However, adjacent to negatively charged surfaces, like glass capillary tubes (Grossman, 1992) or plasma membranes (McLaughlin and Poo, 1981), the larger number of mobile charge carriers are inorganic cations, like Na^+, which are electrophoresed to the cathode.

Electrophoresed cations drag their shells of hydration toward the cathode, resulting in electrically driven water flow, termed electro-osmosis or electro-osmotic flow (EOF). Hundreds of eukaryotic cell types possess negative surface potentials (Mehrishi and Johann, 2002; Slivinsky et al., 1997), leading to cathodal EOF.

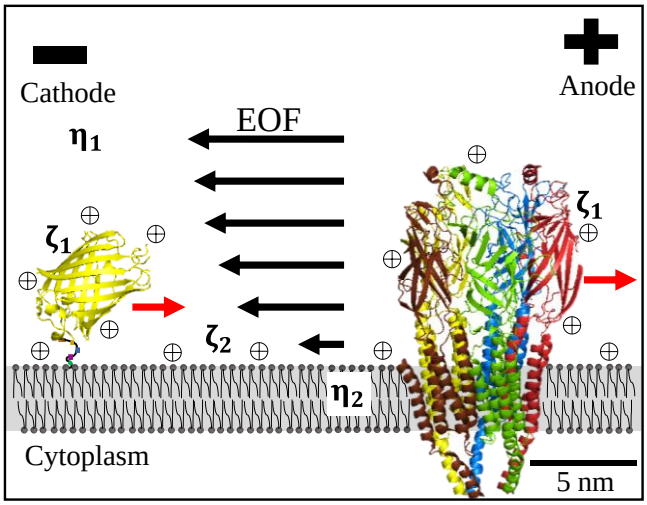

Figure 1. **External DC EFs generate opposing forces on plasma membrane surface proteins.** Electrophoretic forces direct net negatively charged proteins, yellow fluorescent protein with a lipid anchor and the transmembrane nicotinic acetylcholine receptor, toward the anode (red arrows). Electrophoresis of mobile cations ⊕ and their shells of hydration, directs water flow to the cathode (EOF) and generates a force on surface exposed proteins toward the cathode.

The electro-osmotic force on surface proteins toward the cathode is proposed to be stronger than the opposing electrophoretic force toward the anode as many surface proteins accumulate on the cathode side of cells (Brown and Loew, 1994; Fang et al., 1998; Huang et al., 2009a; McLaughlin and Poo, 1981; Orida and Poo, 1978; Poo and Robinson, 1977; Stollberg and Fraser, 1988; Tank et al., 1985; Zhao et al., 1999a) and polarize the cytoplasmic cell motility machinery to the cathode (Pu and Zhao, 2005; Pu et al., 2015; Sato et al., 2009a). However, attempts to reduce the electro-osmotic force by increasing media viscosity did not reduce cathodal migration (Allen et al., 2013; Jaffe and Poo, 1979).

McLaughlin and Poo (1981) modelled the net velocity (u_1) of an electromigrating cell surface macromolecule (Eq. 1) as the difference between electrophoretic and electro-osmotic forces and influenced by drag force exerted by the plasma membrane (eq. 9 from McLaughlin and Poo, 1981). E_θ is the applied DC EF strength and $\in_r \in_0$ is the permittivity of the media. The other variables are the physical parameters of the cell membrane and cell surface macromolecule that

determine the magnitude of the three forces listed above, where a_1 and a_2 are the equivalent radii of the macromolecule in the extracellular space and embedded in the lipid bilayer, η_1 and η_2 are the viscosity of the extracellular media and the lipid bilayer, and ζ_1 and ζ_2 are the surface zeta potentials of the extracellular domain of the macromolecule and the cell surface, respectively. Fig. 1 includes location for the viscosity and zeta potential terms where ζ_1 could represent any surface protein.

Eq. 1 $$u_1 = E_\theta \in_r \in_0 \frac{a_1(\zeta_1 - \zeta_2)}{a_1\eta_1 + a_2\eta_2}$$

Eq. 1 indicates that macromolecules with larger extracellular domains and smaller lipid bilayer spanning domains will electromigrate at rates closer to the EOF rate which reaches 150 μm/min in normal saline according to Eq. 2, for a 125 mV/mm EF applied to a cell with an average zeta potential of -33.7 mV (Slivinsky et al., 1997).

Eq. 2 $$\text{EOF rate} = E_\theta \in_r \in_0 \frac{\zeta_2}{\eta_1}$$

Increasing extracellular viscosity (η_1) is hypothesized to decrease electromigration of surface proteins whether ζ_1 (electrophoresis) or ζ_2 (electro-osmosis) dominates (Eq.1) and will decrease EOF directly (Eq. 2). Therefore, polarized electromigration of cell surface macromolecules will decrease, and cell migration direction will become random in applied DC EFs. Despite these predictions, two attempts to impair galvanotaxis by increasing extracellular viscosity did not affect the direction or speed of cell growth (Jaffe and Poo, 1979) or cell migration (Allen et al., 2013), leading to the conclusion that EOF is not driving cathode-directed galvanotaxis. Those efforts involved use of only a high molecular weight (HM) polymer (~400 kD) over a wide viscosity range 0.001-300 Pa•s (Jaffe and Poo, 1979) and only a single sized polymer at low viscosity 50 mPa•s (Allen et al., 2013). Considering that HM polymers give rise to large pores

between the polymers with little change to viscosity within those pores (Jee et al., 2014) we propose that they are less effective than low molecular weight (LM) polymers in altering viscosity within the boundary layer near the cell surface where EOF is generated. To test this hypothesis, we have employed a wide range of neutral viscous polymers in attempts to increase viscosity in the boundary layer of cells and influence galvanotaxis.

MATERIALS AND METHODS

Keratocyte culture and EF Application

Adult zebrafish (*Danio rerio*) were handled and anesthetized before scale removal according to IACUC protocol #15-022A. Keratocyte culture (Graham et al., 2013) and EF application (Huang et al., 2009a) were performed as described previously, using an enclosed chamber with dimensions of 22 mm x 7.5 mm x 0.3 mm.

Viscosity manipulation

Viscosity of media was manipulated by mixing methyl cellulose (MC) (Methocel A, Sigma-Aldrich, St. Louis MO) into normal fish Ringer's (FR) media. Centrifugation was used to remove air bubbles and insoluble matter. Viscosity was increased using a range of MC with different molecular weights and a concentration range for the 38 kD MC. The weight average molecular weights of the different MCs are 38 kD, 54 kD, 140 kD, 200 kD, and 400 kD (Sarkar, 1979). Final viscosity of the media was determined using an AR2000 rotating disk viscometer (TA Instruments, New Castle, DE) calibrated with high and low viscosity standards (Cannon Instrument Company, State College, PA).

Cell motility and particle velocimetry analysis

Time-lapse images of migrating keratocytes were collected each minute for 65 or 125 minutes at ambient temperature, 21^{o}C. The electric field was applied after 5 minutes of random migration. Movement was tracked and quantified using ImageJ image analysis software (Rasband, 1997-2012). Single cells chosen for analysis did not contact other cells or debris and remained within the field of view during the entirety of the experiment. The mean cosine Θ was calculated as described previously (Huang et al., 2009a) and a Student's t-test was used to compare means.

Small immersed particles of neutral MC were used to measure bulk fluid flow in viscous media during EF application, instead of positively or negatively charged microspheres as the microsphere velocity would have been affected by electrophoresis. ImageJ was used to track and determine particle velocity for high viscosity media made with low and high molecular weight polymers. Shear stress on the cells was determined by multiplying the shear rate by the dynamic viscosity. Shear rate was calculated by dividing particle/fluid speed (μm/s) by 10 μm, assuming that the measured particles were within 10 μm of the plasma membranes, even though the chamber height was 300 μm and the particles could have been much farther away.

Whole cell electrophoresis

Cell surface potentials were determined by monitoring cell velocity during application of an electric field. Chambered dishes, as described above, were coated with polyhydroxyethylmethacrylate (pHEMA) to reduce EOF along the inner surfaces of the chamber. 40 mg of pHEMA was added to a 2 ml Eppendorf tube of EtOH and vortexed for 1 minute before solubilizing at 37˚C overnight. Solubilized pHEMA was then pipetted into the trough of chambers and allowed to dry in a humidified 37˚C incubator to form a layer of pHEMA hydrogel. This was repeated until pHEMA coated the bottom of the chamber. The top surface of pHEMA was allowed to hydrate in media for a few hours before use. The chamber was capped with a plastic, hydrophobic coverslip. Cells were not allowed to touch down to the pHEMA during measurements as this created measurable resistance to whole cell electrophoresis.

Fish keratocytes and CHO cells were detached from the culture dish bottom with divalent free fish Ringer's or divalent free Ringer's to prevent loss of surface proteins and surface charge that occurs during protease treatment. Cells were concentrated with brief centrifugation and resuspended in normal fish Ringer's or Ringers prior to measurements.

Imaging of Fluorescent Membrane Macromolecules

Electromigration studies of cell surface ConA receptors and yellow fluorescent protein (YFP) bound to an external lipid anchor, glycosylphosphatidylinositol (GPI) with an N-glycosylated site, were performed on spherical CHO cells at room temperature. Newly plated, spherical cells with less formed cytoskeletons help ensure that a large fraction of cell surface macromolecules are freely diffusible in the plasma membrane and not immobilized by the cytoskeleton. Spherical CHO cells also have less tendency to migrate than fully adhered cells. Electromigration of ConA receptors was studied by using confocal fluorescence imaging of tetramethylrhodamine ConA at a low final concentration of 2 μg/mL to minimize capping and crosslinking (Yahara and Edelman, 1975). Also 50 μg/ml ConA inhibits electromigration of surface ConA receptors (Poo et al., 1979). Plasma membrane TMR-ConA (ex 559 nm, em 625/50 nm) and YFP-GPI (ex 515 em 542/40) distribution were determined at the beginning of experiments and also 20 min after application of a 1000 mV/mm EF using an Olympus FV1200 confocal system with an IX81 inverted microscope. For each treatment, a total of 30-50 cells from at least two different chambers were analyzed before and after EF application. EF magnitude alone does not favor EOF over electrophoretic forces, see Eq. 1 above. A Student's t-test was used to compare fluorescent intensity ratios.

Fluorescence Correlation Spectroscopy

Single point FCS measurements were performed for fluorescein-labelled dextran (3 kD) and ovalbumin (45 kD) using a Zeiss LSM510 ConfoCor 3 system with Axiovert 200M microscope. The samples were excited with the 488 nm line of an Argon ion laser and the laser power was controlled using an acousto-optic modulator. The samples (final concentration of 20 nM) were placed on a coverslip (No. 1.5) on top a 40X 1.2 NA water immersion objective. The laser was reflected to the objective using a dichroic mirror that reflects the 488 nm laser line but transmits the higher wavelength fluorescence. Fluorescence was collected using the same objective,

passed through the dichroic mirror, and focused to the detector after passing through a 505-610 nm band pass filter and a pinhole (2.27 airy units) to reject out of focus light. The signal was collected using an Avalanche Photo Diode. The acquisition of fluorescence intensity traces and the calculation of the correlation functions were performed using the ConfoCor section of LSM-FCS software provided with the microscope. Average FCS decays were calculated from 6 runs of 45 s each. The average correlation functions were then fitted using Origin 9 software (OriginLab, Northampton, MA). The width (w_0) of the point spread function (PSF) was calculated using 30 nM solution of monomeric EGFP in DPBS buffer. The FCS decay from EGFP was fitted to the following FCS equation and the diffusion coefficient (D) was fixed at 90 $\mu m^2/s$ (Petrasek and Schwille, 2008).

Eq. 3
$$G(\tau) = G(0) * \left(1 + \frac{4D\tau}{{w_0}^2}\right)^{-1} * \left(1 + \frac{4D\tau}{{z_0}^2}\right)^{-1/2}$$

The value of the axial width of the PSF (z_0) was fixed at 1.5 μm and G(0) represented the amplitude of the correlation function. The calculated width (w_0 value :0.31 μm) was then used to calculate the diffusion coefficient of the other fluorophores in different MC solutions. The FCS decays from the samples showed a complex behavior and the shape of the single diffusion component FCS decay was unable to describe the shape of these FCS decay curves as reported earlier for diffusion in MC (Jee et al., 2014). Thus, they were fitted with a dual diffusion component FCS decay equation in a global fit using the following equation.

Eq. 4
$$G(\tau) = G_1(0) * \left(1 + \frac{4D_1\tau}{{w_0}^2}\right)^{-1} * \left(1 + \frac{4D_1\tau}{{z_0}^2}\right)^{-1/2} + G_2(0) * \left(1 + \frac{4D_2\tau}{{w_0}^2}\right)^{-1} * \left(1 + \frac{4D_2\tau}{{z_0}^2}\right)^{-1/2}$$

Here, $G_1(0)$ and $G_2(0)$ are the amplitude of the correlation functions at short lag time (τ) as associated with diffusion coefficients D_1 and D_2. Prior to the fitting and plotting, the FCS decays were normalized to the amplitude of one at the shortest lag time (τ) to determine the shifts in decay

times. In these global fits, the faster diffusion component D_1, reflecting diffusion between the MC polymers, was varied, while the slow diffusion coefficient D_2, reflecting fluorescent molecules bound within an MC polymer, was kept constant to obtain the best fit (Jee et al., 2014).

The PyMOL Molecular Graphics System, Version 2.0 Schrödinger, LLC was used to help generate Figures 1 and 5.

RESULTS

Methyl cellulose (MC) is a neutral, viscous polymer, manufactured at different molecular weights with different molecular radii (Keary, 2001). We measured viscosity of MC solutions to ensure that the predicted viscosity, according to the manufacturer's instructions, matched the true viscosity. After mixing and removal of insoluble matter in experimental media, we found that MC deviated from predicted viscosity by hundreds of mPa•s at higher concentrations and higher molecular weights. Based on the measured viscosities, the estimated final concentrations (weight/volume) of the polymers are listed in Table 1 to within 0.5% (Sigma-Aldrich, 1997).

Table 1. Estimated final concentrations of Methylcellulose.

Experimental Conditions	Estimated MC Concentration (weight/volume)	Applied Field (mV/mm)	Total Experiments	Total Cell Number	Mean Migration Speed (μm/min)	Mean Cosine Θ
Fish Ringer's alone	none	none	4	106	3.7	-0.02 ± 0.06
Fish Ringer's alone	none	125	7	158	4.3	-0.82 ± 0.04
14.9 ± 0.1 mPa•s, 38 kD MC	2.0%	125	5	81	2.4	-0.67 ± 0.10
97.2 ± 0.8 mPa•s, 38 kD MC	3.5%	125	5	152	1.7	-0.22 ± 0.13
200 ± 4 mPa•s, 38 kD MC	4.5%	125	6	160	1.0	+0.61 ± 0.12
473 ± 14 mPa•s, 38 kD MC	5.5%	125	8	255	0.9	+0.35 ± 0.13
226 ± 9 mPa•s, 54 kD MC	3.5%	125	7	152	2.0	-0.23 ± 0.15
307 ± 2 mPa•s, 140 kD MC	2.0%	125	6	100	3.0	-0.44 ± 0.20
508 ± 1 mPa•s, 200 kD MC	1.5%	125	4	56	4.1	-0.83 ± 0.12
334 ± 5 mPa•s, 400 kD MC	1.0%	125	5	85	3.7	-0.88 ± 0.03

Galvanotaxis of zebrafish keratocytes, (illustrated in Fig. 2A), was measured in media with different concentrations of MC polymers with different molecular weights. Directionality was determined by measuring the mean cosine $\Theta = (\Sigma_i \cos \Theta_i)/n$, which reflects the mean angle of the path of migration with respect to the cathode-anode axis. A peak cathodal response is -1 and a peak

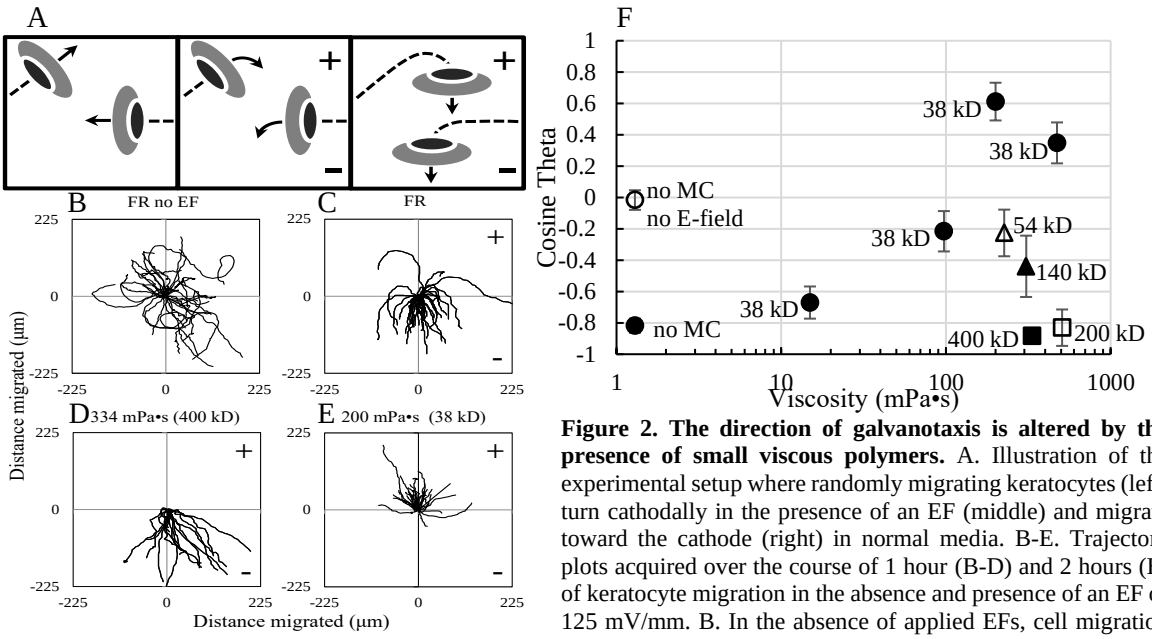

Figure 2. The direction of galvanotaxis is altered by the presence of small viscous polymers. A. Illustration of the experimental setup where randomly migrating keratocytes (left) turn cathodally in the presence of an EF (middle) and migrate toward the cathode (right) in normal media. B-E. Trajectory plots acquired over the course of 1 hour (B-D) and 2 hours (E) of keratocyte migration in the absence and presence of an EF of 125 mV/mm. B. In the absence of applied EFs, cell migration occurs randomly with respect to the point of cellular origin. C. In FR and in the presence of an applied EF, cells migrate toward the cathode. D. In high viscosity media, made with HM polymers, cells migrate cathodally. E. In high viscosity media, made with LM polymers, cells migrate anodally. F. Small polymers impaired cathodal migration (38 kD, 54 kD and 140 kD) or reversed migration toward the anode at higher concentration (38 kD), while larger polymers (200 and 400 kD) did not alter cathodal migration.

anodal response is +1. In fish Ringer's (FR) alone (bulk viscosity of 1.2 mPa•s), keratocytes migrate randomly in the absence of an applied EF (Fig. 2B and Table 1), with a mean cosine Θ value near zero, -0.02 ± 0.06. However, they display robust cathodal migration in response to an EF of 125 mV/mm (Fig. 2C). EF exposed cells in FR show a robust cathode-directed migration with a mean cosine Θ value, of -0.82 which is consistent with an earlier report (Huang et al., 2009a).

In attempts to reduce boundary layer EOF, we increased external viscosity using a range of high molecular weight (HM) MC polymers. First, bulk viscosity was increased to 334 mPa•s and 508 mPa•s using MC with weight average molecular weights of 400 kD and 200 kD, respectively. Despite the increased viscosity, neither migration speed nor cathodal directionality (Fig. 2D and Table 1) changed significantly compared to FR alone ($p>0.1$ for both, students t-test), with mean cosine Θ values of -0.88 and -0.83, respectively. We conclude that these results are highly consistent with previous reports (Allen et al., 2013; Jaffe and Poo, 1979) which had been used to form the basis for discounting EOF as a mechanism driving cathodal migration.

While HM MC did not affect cathodal migration, we found that LM MC polymers had dose-dependent effects on migration speed (Table 1) and cathodal directionality. Increasing viscosity to 307 mPa•s with 140 kD MC and 226 mPa•s with 54 kD MC caused decreased cathodal migration from -0.82 to -0.44 and -0.23, respectively. Using the lowest molecular weight MC (38 kD) that is commercially available, cathodal migration decreased to -0.67 and -0.22 with viscosities of 14.9 mPa•s and 97.2 mPa•s, respectively. Greater increases in viscosity, to 200 and 473 mPa•s with the 38 kD MC, caused cells to completely reverse direction of migration (Fig. 2E) with mean cosine Θ values of +0.61 and +0.35, respectively. A summary plot of mean cosine Θ values (Fig. 2F) shows the varying impact of the different polymers on directed migration. Comparison of results from samples with high viscosity, ≥ 200 mPa•s, indicate that the LM polymers reversed migration toward the anode while the HM polymers did not alter cathode directed migration compared to normal FR. The stark difference in response between the LM polymers and the HM polymers should allay concerns of nonspecific chemical effects of MC, considering the polymers are the same except for their size. We conclude that changes to the bulk viscosity alone are not sufficient to account for reversal of migration during galvanotaxis.

In addition to electro-osmosis at the cell surface, there is electro-osmosis against the charged surface of the electrophoretic chamber (tissue culture plastic) and it is obvious in viscous media. In order to address concerns that bulk flow may direct migration, small insoluble particles of neutral MC that remained in solution were used to estimate fluid flow in the chambers during applied EFs. In LM MC at 200 mPa•s, 4 chambers showed only cathode-directed flow while 2 showed flow in both directions. In LM at 473 mPa•s, 5 chambers showed only cathode-directed fluid flow and 3 showed flow in both directions. In HM at 334 mPa•s, 2 chambers showed cathode-directed flow, 2 showed anode-directed flow and 1 showed both. While cathodal fluid flow is most likely due to electro-osmosis along the culture chamber surfaces, anodal fluid flow may be due to shifting of the height of the agarose bridges leading to subtle pressure changes on either side of the chamber. Regardless of direction, the average flow rate was very slow; 7.5 and 18.1 μm/min in FR

with 200 and 473 mPa•s LM, respectively, and 12.7 μm/min for FR with 334 mPa•s HM, producing shear stresses on the cells of 2.5 mPa, 14.3 mPa and 7.1 mPa, respectively. These shear stresses are about 300-1000 times less than those required to direct migration of fish keratocytes in culture (Allen et al., 2013). We conclude that the bulk fluid flow observed in our experiments is negligible in directing migration. Additionally, anodally migrating keratocytes were more often, migrating against the direction of the bulk fluid flow induced shear stress.

Eq. 1, first presented by McLaughlin and Poo (1981), is based on the Stokes-Einstein relation and indicates that an increase in external viscosity will only decrease cathode-directed migration and not reverse migration to the anode. Therefore, we explored the possibility that diffusion in porous media of MC mixtures does not follow the Stokes-Einstein relation. To a limited extent this has already been done. Unlike diffusion in viscous solutions with very small molecular weight viscous agents, diffusion in solutions of polymers of MC does not follow a purely Stokes-Einstein relation (Jee et al., 2014). To validate this for macromolecules, we measured diffusion coefficients for fluorescein-labelled dextran (3 kD) and ovalbumin (45 kD) in different solutions of MC using fluorescence correlation spectroscopy (FCS). The resulting decay curves from the samples showed a complex behavior, similar to previous measurements in MC (Jee et al., 2014). Therefore, the curves were fitted with a dual diffusion component (see Eq. 4 on Pg. 14). The fast terms (D_1) for diffusion of fluorescent dextran and ovalbumin between MC polymers are only reduced to about half of their values in FR alone (Fig. 3A and B). According to the Stokes-Einstein relation, a 200-fold increase in viscosity should decrease the diffusion coefficients to 0.5% of their values in FR alone. However, they were only decreased to about 40%, an 80-fold deviation from Stokes-Einstein. We conclude that for the concentrations we used to reverse galvanotaxis, MC reduced diffusion and therefore electrical mobility by only a factor of 2-3, not by a factor of 200 as predicted according to Stokes-Einstein. The best fit models for the fluorescence autocorrelation

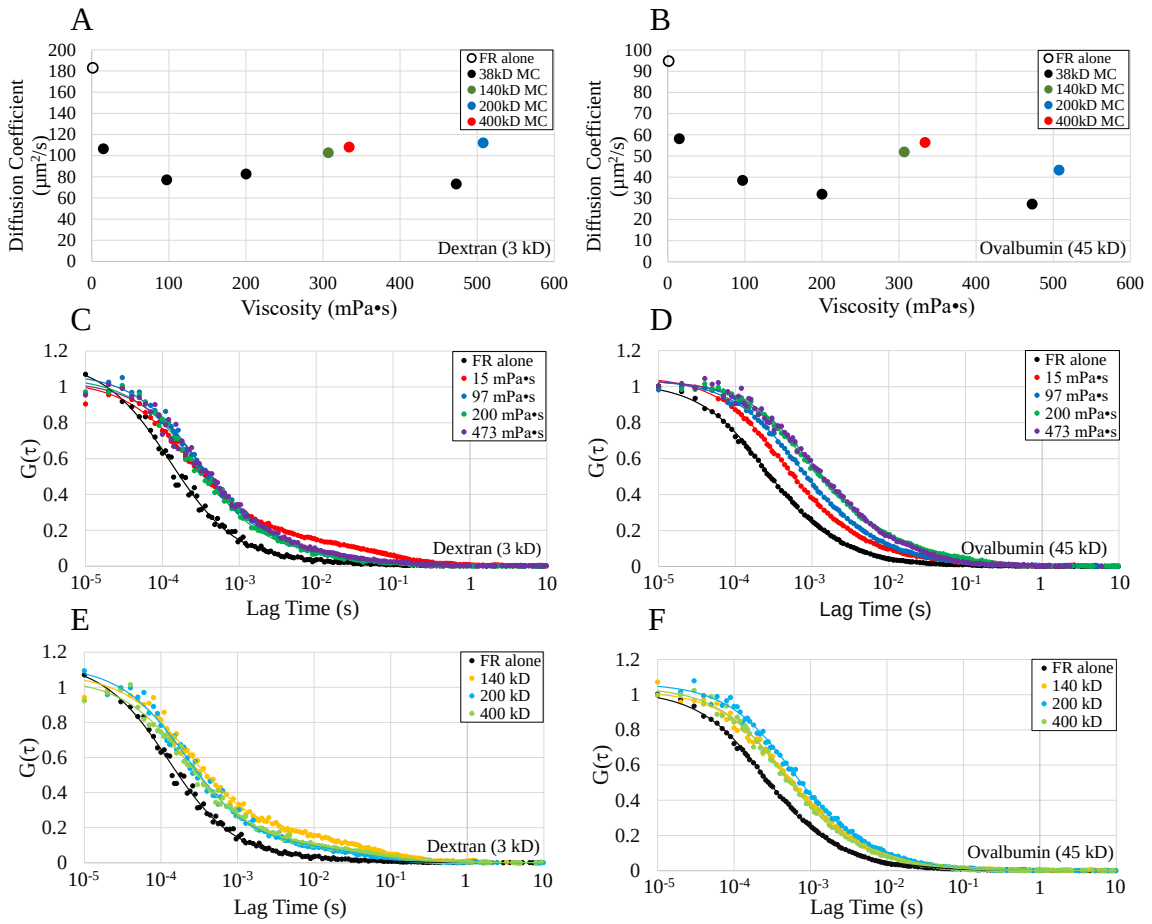

Figure 3. Diffusion of fluorescein-labelled dextran and ovalbumin in MC solutions does not follow a Stokes-Einstein relation. A, B. Measured diffusion coefficients for dextran (A) and ovalbumin (B) are hindered the most by the smallest MC polymer (38 kD) at 473 mPa•s, but only to values that are 40% and 30%, respectively, compared to their values in FR alone. Standard errors are smaller than the vertical dimensions of the data markers. C, D. The autocorrelation curves and modelled fit for dextran (C) and ovalbumin (D) over a viscosity range of 1.2 mPa•s to 473 mPa•s for the 38 kD MC. E, F. The autocorrelation curves and modelled fit for dextran (E) and ovalbumin (F) in FR alone and HM polymers, 307 mPa•s of 140 kD, 508 mPa•s of 200 kD, and 334 mPa•s of 400 kD.

curves are displayed for the 38 kD MC (Fig. 3C and D) and the HM MC solutions (Fig. 3E and F). It appears than in MC, diffusion is hindered, being constrained to spaces between polymers, a feature common to other porous media like agarose gels or the cytoplasm of cells (Amsden, 1998; Deen, 1987; Di Rienzo et al., 2014). While these results indicate that Eq. 1 does not accurately describe electromigration of surface macromolecules in viscous solutions of MC, it still does not explain reversed galvanotaxis. According to our hypothesis, reversed electromigration of cell

surface receptors to the anode would occur if LM MC solutions reduce electro-osmosis or hydraulic permeability to a greater extent than they reduce electrophoresis.

Hydraulic permeability (K) between globular polymers like MC may be similar to solutions of monodisperse spherical particles. In these solutions, hydraulic permeability is proportional to the power of the diameter (d) of the spheres and the power of porosity or void fraction ($\in$) between the spheres according to the Kozeny-Carman formula (Eq. 5) and the Rumpf and Gupte expression (Eq. 6) (Zaman and Jalali, 2010). Therefore, hydraulic permeability would be 4 fold smaller for a polymer half the diameter of a HM MC. The reduced void fraction is more challenging to compare considering that only the void fraction between the plasma membrane and the first layer of MC polymers is relevant. The void fraction within 15 nm of the membrane is 25% smaller for a polymer half the diameter of the HM MC polymer used in this study. Taken together, a reasonable estimate is that the hydraulic permeability near the membrane would be $10 < K < 100$ fold smaller when using LM MC compared to HM MC used in this study.

Eq. 5 $$K = \frac{\in^3 d^2}{180(1-\in)^2}$$

Eq. 6 $$K = \frac{\in^{5.5} d^2}{5.6}$$

In other porous media like agarose gels, hydraulic permeability has been shown to be reduced to a greater extent than diffusion when void fraction is reduced (Johnson et al., 1996). A step increase in agarose concentration, which reduced pore size and void fraction, decreased hydraulic permeability through an agarose gel by greater than a factor of 10, while diffusivity of macromolecules ranging between 14-105 kD with radii between 2-6 nm, was reduced by only a factor of 2 (Johnson et al., 1996). Therefore, a smaller void fraction between neutral polymers can reduce electro-osmotic force by a significantly greater amount than it reduces electrophoretic force.

In combination, the diffusion measurements we report in MC, along with these earlier results in porous media, support the idea that the closer packing of the smaller LM MC will pose

significantly greater reduction in EOF than the HM MC. We conclude that when pore sizes between MC polymers are of similar dimension to the size of diffusing solutes, electro-osmosis of surface macromolecules to the cathode is reduced to a greater extent than electrophoresis of surface macromolecules to the anode. Net negatively charged surface proteins directed toward the cathode by electro-osmosis which promoted cathode migration, now have a greater chance to be electrophoresed to the anode to promote anodal migration.

The most convincing evidence that EOF is strong enough to promote cathodal accumulation of negatively charged surface molecules is obtained by monitoring surface macromolecule redistribution in an applied EF. These experiments have been performed on a range of different eukaryotic cells (Brown and Loew, 1994; Fang et al., 1998; McLaughlin and Poo, 1981; Orida and Poo, 1978; Poo and Robinson, 1977; Stollberg and Fraser, 1988; Tank et al., 1985; Zhao et al., 1999a) as the principles of electrophoresis and electro-osmosis are common. According to our hypothesis, reduction of EOF with LM polymers should reduce cathodal accumulation of surface macromolecules to an extent that is significantly greater than HM polymers. We used Chinese hamster ovary (CHO) cells to follow redistribution of fluorescent TMR-ConA and YFP-GPI on the surface of cells, as zebrafish keratocytes possess rapid membrane turnover making it difficult to distinguish between intracellular or extracellular localization of fluorescent markers. In addition, electromigration of surface markers could not be performed on CHO cells under normal physiological temperatures at which they migrate. Viscosity of MC mixtures is temperature dependent, being one of the few viscous polymers that gels with increasing temperature (Sarkar, 1979). The higher concentrations of MC, used here, gel below 30^{o} C so experiments were performed at ambient room temperature, 21^{o} C.

Electrical potentials of both zebrafish keratocytes and CHO cells were determined to ensure that they were negative. Cell surface electrical potentials for zebrafish keratocytes -7.4 ±

0.9 mV (n = 34) were slightly weaker than the surface potentials for CHO cells, -16.3 ± 2.7 mV (n = 37). However, these negative values are still within the narrow range common to other eukaryotic cells at neutral pH (Mehrishi and Johann, 2002; Slivinsky et al., 1997) and indicate cathode-directed EOF.

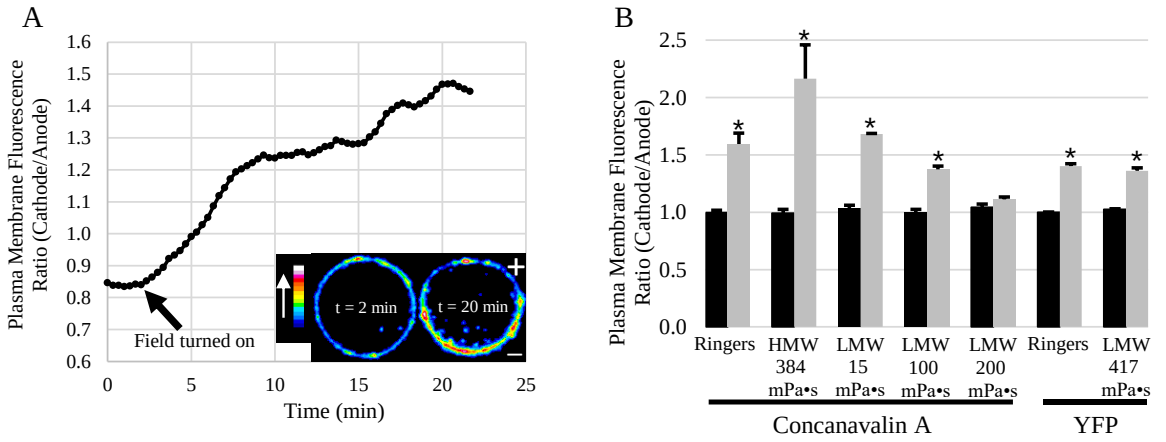

Figure 4. Electric fields direct ConA receptors and YFP-GPI accumulation toward the cathode. A. Time course of ConA receptor electromigration in 384 mPa•s of 400 kD MC, displayed as a ratio of the plasma membrane ConA fluorescence (cathode facing / anode facing). Color bar indicates relative brightness of TMR-ConA. B. Summary plot of the plasma membrane fluorescence ratio before EF application (black) and 20 min after EF application (gray). Cathodal accumulation of cell surface ConA receptors occurs in Ringer's and Ringer's with HM or low levels of LM (38kD). However, cathodal electromigration of ConA receptors is reduced in 38 kD MC at 100 mPa•s and inhibited at 200 mPa•s. Under similarly viscous conditions with LM, the small YFP-GPI accumulates at the cathode. (* = $p < 0.05$).

Fluorescently labelled ConA was used to follow rapid redistribution of glycosylated cell surface macromolecules before and after application of a 1000 mV/mm EF. A time course for ConA redistribution (Fig. 4A) is shown with before and after images (inset). In FR immediately before EF exposure (black), CHO cells possessed an average future cathode/ future anode (C/A) plasma membrane fluorescence ratio of 1.00 ± 0.02 (n=32) indicating symmetrical distribution of ConA receptors (Fig. 4B). Measurements after 20 min in the EF indicate that the ConA bound receptors redistributed in greater abundance to the cathode, with a C/A fluorescence ratio of 1.60 ± 0.09 (n=32). Similarly, in the highest molecular weight MC (400 kD) at 384 mPa•s, ConA receptors accumulated on the cathodal side of the cells relatively quickly (Fig. 4A). The measured C/A ratio of 2.16 ± 0.30 (n=44) after EF application was twice as great compared to 1.00 ± 0.04

(n=30) measured before EF application. However, conditions that reduced cathodal migration, 38 kD MC at 100 mPa•s, showed decreased electromigration of ConA receptors (Fig. 4B). Moreover, conditions which reversed migration to the anode showed no significant asymmetric redistribution of ConA receptors after 20 min in the EF, 1.11 ± 0.02 (n=88), compared to 1.04 ± 0.03 (n=76) before EF application ($p > 0.1$, students t-test). These results indicate that LM reduces cathodal accumulation of surface macromolecules in a concentration-dependent manner, corresponding to the concentration-dependent inhibition of cathodal galvanotaxis and ultimate reversal of migration toward the anode.

ConA binds to α-D-mannosyl and α-D-glucosyl groups from glycoproteins and glycolipids, so macromolecules over a wide size range are labelled and may be freely diffusing in the plasma membrane or anchored to the cytoskeleton or restricted to a small membrane domain. Therefore, reversed electromigration of a single surface protein to the anode may be hidden, now that bulk electromigration to the cathode (electro-osmosis) has been impaired for many different surface proteins. To determine whether a population of a single type of small, freely diffusing, surface bound protein could still migrate through the smaller pores of the LM and not simply be stuck in place by the MC, yellow fluorescent protein bound to a glycosylphosphatidylinositol anchor (YFP-GPI) was monitored during EF application. In the presence of an EF, the 3 nm by 4 nm YFP (26 kD) with weak negative charge, electromigrated to the cathode with an average C/A fluorescence ratio of 1.40 ± 0.02 (n = 25) compared to 1.00 ± 0.01 (n=14) before EF application (Fig. 4B). In the presence of the 38 kD MC at 417 mPa•s, the YFP-GPI displayed weaker accumulation but still migrated toward the cathode with a C/A fluorescence ratio of 1.36 ± 0.03 (n = 38) compared to 1.03 ± 0.02 (n=15) before EF application. We conclude that despite the high viscosity, EOF is still occurring within nanometers of the plasma membrane between the LM polymers and still directs small proteins with weak surface charge, like YFP-GPI, to the cathode.

DISCUSSION

We conclude that MC polymers have high porosity and act more like sieves or porous gels (Grossman and Soane, 1991; Kim and Morris, 1994) than very small viscous agents e.g. glycerol. We also conclude that viscosity alone or changes in osmolality are insufficient to explain our results. High viscosity with large polymers did not alter galvanotaxis and the greatest number of MC polymers altered osmolality of the media by only 0.5% which is relatively insignificant considering keratocytes can withstand a 75% reduction in osmolality without affecting galvanotaxis (Allen et al., 2013). We propose that in order to impair EOF in the cellular boundary layer, viscosity must be increased in the cellular boundary layer, within nanometers of the plasma membrane, whether the cell surface is closer to being a 'hard' surface (Bocquet and Charlaix, 2010) or a 'soft' surface (Ohshima, 1995). The smaller polymers can more effectively reduce hydraulic permeability next to the membrane. An illustration of the 38 kD and 400 kD MC polymers based on their hydrodynamic radii at 20° C (Keary, 2001; Kobayashi et al., 1999) is drawn to scale in Fig. 5 along with a number of other surface proteins known to migrate cathodally in weak EFs.

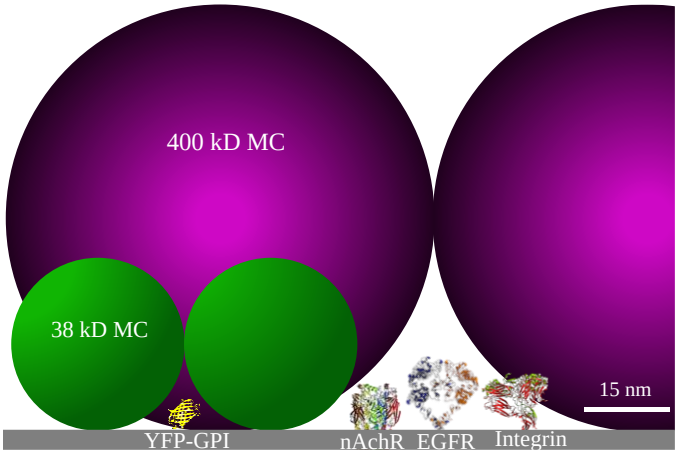

Figure 5. Plasma membrane surface in the presence of HM (purple) and LM (green) MC polymers. Surface macromolecules known to electromigrate to the cathode including the nicotinic acetylcholine receptor (nAChR), epidermal growth factor receptor (EGFR), Integrins and YFP-GPI extend from the plasma membrane by less than 15 nm.

The void fraction against the surface of the plasma membrane is much greater for the larger polymer than the smaller polymer, leading to greater hydraulic permeability through which EOF can continue to drive membrane proteins to the cathode. However, the smaller MC polymers can pack more closely against the plasma membrane, reduce the void fraction and reduce EOF to a

greater extent. The smallest MC is still relatively large, giving rise to pores that are larger than the surface proteins shown (Fig. 5). The diffusion results (Fig. 3) confirm that the smallest MC does little to impair diffusion and therefore electrophoresis of macromolecules. These conditions would promote electrophoresis over electro-osmosis and negatively charged surface receptors should migrate to the anode like negatively charged proteins in an electrophoretic gel. Anodal accumulation of the cell surface receptors should lead to anodal migration, according to earlier hypotheses (McLaughlin and Poo, 1981; Robinson, 1985). We conclude that these conditions are met in neutral porous media when the pore sizes are close to the size of the diffusing solutes (Jee et al., 2014; Johnson et al., 1996).

Based on the new results presented here and consistent with the original mathematical model for electrophoresis and electro-osmosis near the surface of cells (McLaughlin and Poo, 1981), we propose that a small surface macromolecule, with greater net negative surface charge than YFP-GPI, accumulates at the cathode side of the cell when EOF is unimpaired and directs cell migration to the cathode. Conversely, when EOF is significantly attenuated by small viscous polymers, electrophoresis becomes the dominant force. Under these conditions, the small surface macromolecule is able to navigate through the pores of the LM polymers, accumulating on the anode-facing side of the plasma membrane, and directs cell migration to the anode. With further experimentation using LM polymers, the surface EF receptor and its signaling pathway, possibly through cGMP and lipids (Sato et al., 2009a), might be identified, clarifying the fundamental process of symmetry breaking at the cellular level and enabling greater control over cellular polarity during artificial tissue and organ fabrication and epidermal wound healing.

CHAPTER 2

ELECTROMIGRATION OF CELL SURFACE MACROMOLECULES IN DC ELECTRIC FIELDS DURING CELL POLARIZATION AND GALVANOTAXIS

ABSTRACT

DC electric fields (EFs) can often induce cellular polarity, and direct migration of cells toward one of the electrical poles. The mechanism(s) by which cells sense weak EFs is not established. We present here a molecular flux model to describe electromigration of plasma membrane macromolecules and compare its predictions to electromigration of a lipid-anchored surface protein, tdTomato-GPI, under different experimental conditions. Gradients of tdTomato-GPI are assembled based on its electrophoretic and electro-osmotic mobilities and collapsed by its own diffusion. The flux model predicts greatest cathodal accumulation for tdTomato-GPI under slightly acidic conditions, and weak cathodal accumulation under alkaline conditions. Predictions by the flux model align closely with measurements of the electromigration of tdTomato-GPI except at pH 6, the only condition examined in which the protein exhibits a net positive surface charge. We use the model to predict the time course and relative steady state for asymmetric accumulation of other surface macromolecules based on their physical properties. We also describe a method for identifying the physical properties of the plasma membrane proteins in zebrafish keratocytes, in order to predict likely candidates for the electric field receptor in this model migratory system that exhibits cathodal galvanotaxis, and to predict the asymmetric distribution of proteins in other cell types. We provide a physical basis for predicting the dynamics of electromigration for numerous cell surface macromolecules and provide evidence for supporting the role of electromigration in directing cell polarity, migration and growth in response to weak EFs.

INTRODUCTION

In response to extracellular DC electric fields (EFs), cells polarize, and migrate (galvanotaxis) or grow (galvanotropism) toward one of the electrical poles (Funk, 2015; McCaig et al., 2005; Messerli and Graham, 2011; Minc and Chang, 2010; Pu et al., 2015; Wang et al., 1989; Zhao, 2009). Such fields are involved with generating epithelial and embryonic polarity and are also used to promote healing of chronic epidermal wounds (Frykberg and Banks, 2015; Kloth and Zhao, 2010; Levin and Stevenson, 2012; Pu et al., 2015; Robinson and Messerli, 2003b). EFs as small as 10 mV/mm, are sufficient to polarize epithelial and neuronal cells (Hinkle et al., 1981; Huang et al., 2009b; Nishimura et al., 1996; Stump and Robinson, 1983). A longstanding debate over the mechanism(s) by which cells sense weak, DC EFs involves two competing hypotheses, electromigration of cell surface macromolecules and membrane depolarization (McCaig et al., 2009; McLaughlin and Poo, 1981; Robinson, 1985; Weaver and Astumian, 1990). The electromigration model depends on electrical force parallel to the plane of the plasma membrane (McLaughlin and Poo, 1981), while the membrane depolarization model depends on electrical force perpendicular to the plane of the plasma membrane (McCaig et al., 2009; Weaver and Astumian, 1990; Zhao, 2009). Both hypotheses depend on sensing weak EFs by a putative electric field receptor (EFR) which directs cell polarity, however, no ubiquitous EFR has been identified.

In attempts to identify the EFR in different cell types, random and targeted screens have been employed including gene knockdown using mutagenesis (Gao et al., 2015; Sato et al., 2009b; Zhao et al., 2002b; Zhao et al., 2006) or siRNA (Nakajima et al., 2015). Other attempts have included screens with pharmacological agents (Djamgoz et al., 2001; McCaig, 1989; Palmer et al., 2000; Pullar and Isseroff, 2005; Riding and Pullar, 2016; Sun et al., 2013; Trollinger et al., 2002; Zhao et al., 2006; Zhu et al., 2015). Disruption of many different genes and signaling pathways has only reduced EF-directed polarity. However, in a few cases, galvanotaxis was reversed by altering physical properties of the surface of cells, including modification of surface charge (Huang

et al., 2016; Huang et al., 2017; Rajnicek et al., 1998; Saltukoglu et al., 2015), and reduction of electro-osmotic water flow next to the plasma membrane (Kobylkevich et al., 2018). The mechanisms by which these alterations reversed galvanotaxis are consistent with the electromigration model and not the membrane depolarization model. Considering the success in reversing galvanotaxis by targeting physical features of cells, we have directed our attention towards studying the electromigration model of galvanotaxis to gain greater insight into the dynamics of electromigration and to guide our efforts with identifying additional candidates for the EFR in multiple cell types.

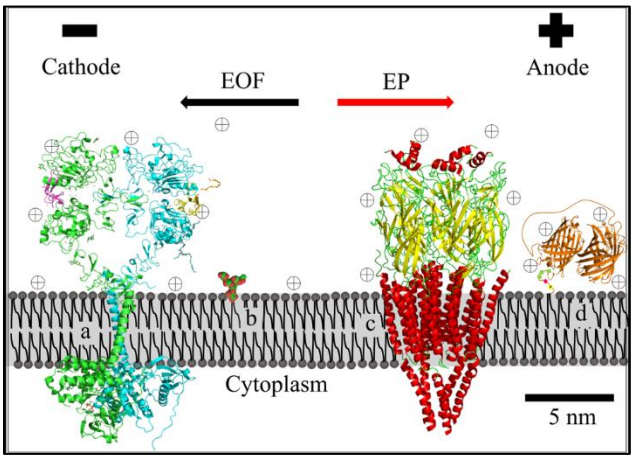

Figure 6. Electromigration in the plasma membrane is dependent on electrophoresis and electro-osmosis. Electrophoresis (EP) attracts macromolecules with a net negative charge toward the anode (red arrow). Mobile cations (⊕) near the negatively charged cell surface, Na^+ being the most abundant, move to the cathode and drag their shell of hydration generating an electrically induced water flow, referred to as electro-osmotic flow (EOF) (black arrow). Electromigration of surface macromolecules is dependent on both forces and drag from the membrane and cytosolic domains. Representative macromolecules with negative surface charges are a) EGFR, b) ganglioside GM1, c) nAChR, and d) tdTomato-GPI.

McLaughlin and Poo (1981) presented the first mathematical model to describe electromigration and accumulation of plasma membrane surface macromolecules based on electrophoresis, electro-osmosis and local drag, illustrated in Fig. 6. Electrophoresis (EP) of negatively charged surface macromolecules is toward the anode. Simultaneously, mobile cations in the vicinity of the negatively charged cell surface, are attracted to the cathode. The cations carry their shell of hydration generating water flow, electro-osmotic flow (EOF), towards the cathode. Electromigration of surface macromolecules on cells (Fang et al., 1999; Giugni et al., 1987; Huang et al., 2009b; Huang et al., 2017; Lin et al., 2017; McLaughlin and Poo, 1981; Orida and Poo, 1978; Poo and Robinson, 1977; Yan et al., 2009; Zhao et al., 1999b; Zhao et al., 2002a) and supported lipid bilayers (SLB) (Groves and Boxer, 1995; Han et al., 2009; Liu et al., 2011) is consistent with this model, where

phospholipids with small, charged head groups, electromigrate according to their electrophoretic mobility, and larger, membrane-associated macromolecules that extend outside the lipid bilayer, electromigrate via the combination of their electrophoretic and electro-osmotic mobilities. The explanations by the parsimonious models, that followed, indicated that the asymmetric distribution of membrane receptors for trophic factors or that promote cell adhesion, could lead to asymmetric migration toward one of the electrical poles (Patel and Poo, 1982; Stump and Robinson, 1983). Cathodal migration might be driven by cathodal localization of the EFR and stabilization of the leading edge of migration (Zhao et al., 1999b) or might be driven by anodal localization of the EFR and stabilization of the trailing edge of migration (Allen et al., 2013; Huang et al., 2017). In either case, the model indicates that potential EFRs could be predicted based on their physical properties and the properties of their local surroundings (McLaughlin and Poo, 1981). To date, only a short list of potential EFRs has been suggested despite the fact that approximately 30% of the human proteome consists of plasma membrane spanning proteins (Almen et al., 2009).

A significant criticism of the electromigration model is that accumulation of surface macromolecules is too slow to polarize cells in the short periods of time in which they become polarized (Hart et al., 2013). Also, EFs of ~10 mV/mm, near the threshold of detection for galvanotaxis and galvanotropism, have never been shown to concentrate surface macromolecules to one electrical pole. Additionally, no model describes electromigration when electro-osmosis is decreased by a porous medium (Kobylkevich et al., 2018), or accounts for drag by cytoplasmic domains of membrane macromolecules, or allows for time course modeling of electromigration. Therefore, we have derived an electromigration model using net flux of surface macromolecules. We have performed timelapse imaging to monitor electromigration of a fluorescent surface protein in order to predict electromigration of other surface macromolecules and compare them to the time course of cell turning during galvanotaxis. We also describe the size and charge of proteins from the plasma membrane proteome of zebrafish keratocytes in order to identify candidates for the EFR in this model migratory system.

MATERIALS AND METHODS

Imaging Electromigration of a Fluorescent Membrane Protein

Electromigration of a representative cell surface protein was determined during modification to field strength, protein charge and cell surface zeta potential. The fluorescent, tandem dimer Tomato protein was chosen with a glycosylphosphatidylinositol anchor (tdTomato-GPI) (Johnson et al., 2015) as its lipid anchor is in the outer leaflet of the lipid bilayer (Paulick et al., 2007) and the attached protein is extracellular. Also, tdTomato is relatively small compared to other surface proteins, its surface charge can be estimated over the pH range used (pH 6-9), it has good photostability and its fluorescence is relatively unaffected in the same experimental pH range (Shaner et al., 2004). Chinese hamster ovary (CHO) cells, transfected with tdTomato-GPI, were cultured in phenol red-free Dulbecco's Modified Eagle's Medium (DMEM) with 10% FBS and 1% Pen-Strep. Cells were removed from the culture flask after 3 minutes of exposure to 0.05% trypsin-EDTA, cultured in electrophoretic chambers with cross-sectional area 0.75 cm by 0.03 cm, and allowed to recover for at least 45 min. in a 37^{o}C, 5% CO_2 incubator prior to imaging. This was enough time to enable cells to adhere but also to retain a relatively spherical shape for imaging protein electromigration.

Electromigration of tdTomato-GPI was monitored at ambient temperature, 21^{o}C, in modified Ringer's (in mM: 145 NaCl, 3 KCl, 2 $CaCl_2$, 5 glucose). Modified Ringer's was buffered to different pH with 10 mM Good buffers, pH 6 with MES, pH 7 or 8 with HEPES, and pH 9 with TAPS. Images of the distribution of surface tdTomato-GPI were collected with an Olympus FV1200 confocal system mounted on an IX81 inverted microscope. The plasma membrane distribution of fluorescent tdTomato-GPI (excitation 559 nm, emission 625/50 nm) was imaged in the absence and presence of EFs. Time course measurements were acquired every 30 s, to determine the amount of time required for redistribution to reach steady state. It was determined that even large cells reached steady state within 20 min. Therefore, images of tdTomato-GPI

distribution were acquired before exposure to EF and after 20 min. in an EF, for the different experimental conditions. For each treatment, images from an average of over fifty cells were collected from both control and experimental conditions, using at least two different experimental chambers.

ImageJ analysis software (Rasband, 1997-2018) was used to determine the average pixel intensity of tdTomato-GPI in the plasma membrane at the extreme surfaces of the cell facing the cathode and anode. The region for measurement on the spherical cells included an arc with a height approximately 15% of the cell diameter. The ratio of the average tdTomato fluorescence is reported as the (average cathodal edge fluorescence)/ (average anodal edge fluorescence). An unpaired t-test was used to compare fluorescent intensity ratios and the means ± S.E. are reported.

Determination of Cell Surface Zeta Potential and tdTomato-GPI Surface Charge

The average cell surface zeta potential was determined for the tdTomato-GPI expressing CHO cells as described earlier (Kobylkevich et al., 2018). A few modifications were made. After CHO cells were detached from the bottom of the dish with divalent-free Ringer's they were rinsed once with experimental Ringer's set to the final pH and then resuspended in Ringer's set to the final pH for the experiment. This helped ensure that cells were in Ringer's solution of known pH.

The average surface charge of tdTomato-GPI was determined by summing the charges of the tdTomato protein and its GPI membrane anchor at the different pH levels that were used. The amino acid sequence of tdTomato was loaded in NetSurfP 2.0 (Klausen et al., 2018) and the relative solvent accessibility (RSA) values, from 0 (embedded) to 1 (exposed), were selected from the returned data. An RSA cutoff ≥ 0.1 was chosen to identify exposed and charged amino acid side groups in order to calculate net surface charge of tdTomato. This cutoff is set, based on the success of supercharging GFP at an amino acid with a 0.1 RSA value without affecting the folding of GFP,

indicating that the charge is solvent accessible and not embedded (Lawrence et al., 2007; Thompson et al., 2012).

The pKa of amino acid side groups and amino terminal were used from estimates determined from protein and peptide datasets (Kozlowski, 2016). The pKa for lysine in proteins, 9.1, was determined to be much lower than its pKa in peptides, 10.5, which may be due to the common occurrence of post-translational modification of lysine in proteins (Kozlowski, 2016). Considering that the surface exposed lysines on tdTomato are not reported to be modified, we used the higher pKa value for lysine in peptides (Kozlowski, 2016).

Modeling of Electromigration

A finite difference method using small, iterative steps in space and time was coded in MATLAB script (MathWorks, Natick MA), to solve the derived equations that describe the relative concentration of a surface protein. Cells were modeled as spheres with an average diameter of 15 μm and the applied EF strength was calculated parallel to the surface of the sphere. One condition of the model is that 100% of the surface proteins are freely mobile in the plane of the membrane unless stated otherwise. A second condition of the model is that the cell surface zeta potential remains uniform and that surface proteins are diffuse and do not influence charge of other surface proteins.

The size of tdTomato was determined first by calculating the volume equivalent sphere for the cylindrical Tomato protein and then altering the radius of that sphere to account for the orientation and drag of the cylindrical shape of the protein (Hölzer and Sommerfeld, 2008). The size of an individual tdTomato protein was modeled as a sphere with 1.4 nm radius. The drag of the two Tomato proteins was considered to dominate and the short tether between them was considered relatively negligible. Therefore, two volume equivalent spheres were used for the tdTomato protein during modeling. Similar estimates and calculations were performed to determine the radii of volume equivalent spheres for the GPI lipids (0.6 nm), transmembrane α-helix (0.87

nm), epidermal growth factor receptor (EGFR) extracellular domain (3.2 nm), EGFR intracellular domain (2.3 nm) and ganglioside GM1 extracellular domain (0.88 nm).

Estimates were used for the diffusion coefficients of surface macromolecules and the plasma membrane viscosity. The diffusion coefficient measured for enhanced green fluorescent protein, EGFP-GPI, expressed in CHO cells, ranges between 0.75-1.1 $\mu m^2/s$ at room temperature (Saha et al., 2015). Based on the diffusion coefficient of EGFP-GPI and simulations of changes to protein mobility with increasing size of extracellular domains (Guigas and Weiss, 2015), we estimate that the diffusion coefficient of tdTomato-GPI is close to 0.52 $\mu m^2/s$. However, diffusion coefficients can vary considerably depending on plasma membrane protein density (Frick et al., 2007; Guigas and Weiss, 2015; Peters and Cherry, 1982). The diffusion coefficient used for EGFR is 0.3 $\mu m^2/s$ (Ma et al., 2011; Miyagi and Maruyama, 2010) and the diffusion coefficient for Ganglioside GM1 is 0.47 $\mu m^2/s$ which involved an attached fluorescent label (Goins et al., 1986).

Plasma membrane viscosity also varies over a wide range depending on cell type and temperature, e.g. 270 mPa•s for human ovarian cancer cells at 22^{o}C (Lopez-Duarte et al., 2013), 2150 mPa•s for porcine lens cells at 20^{o}C (Sherin et al., 2017) or 100-600 mPa•s for amphibian photoreceptors at 20^{o}C (Poo and Cone, 1974). In this study we held the viscosity of CHO cells to be about 450 mPa•s at 21^{o}C when used with the diffusion coefficient estimate for tdTomato-GPI described above. Cytosolic viscosity near the plasma membrane was estimated to be 1 mPa•s, similar to the viscosity of extracellular media (Bicknese et al., 1993).

Plasma Membrane Protein Identification

Surface exposed proteins of zebrafish keratocytes were extracted from the zebrafish proteome 'GCF_000002035.5_GRCz10_protein' that was downloaded from the NCBI website https://www.ncbi.nlm.nih.gov/genome/annotation_euk/Danio_rerio/104/. Surface proteins were organized into three categories including transmembrane, integral and GPI-anchored, and estimates of their physical properties were determined in order to predict their direction of electromigration

in plasma membranes in response to applied EFs. Descriptions of the programs used for protein localization, comparison, and identification of physical properties are listed in Appendix A, pg. 83.

Annotation of Gene Ontology (GO) Terms

In order to annotate the functional categories present in each of the three groups of surface proteins, the RefSeq protein IDs were submitted to bioDBnet (Mudunuri et al., 2009), to retrieve their Gene IDs. Gene IDs were submitted to bioDBnet to obtain the corresponding Gene Ontology (GO) terms based on three categories: cellular component, biological processes and molecular function. We consider the molecular function category most relevant for this work.

RESULTS

Electromigration Flux Model

Applied EFs induce electromigration and gradient formation of cell surface macromolecules. The rate and magnitude of gradient formation is dependent on a molecule's net flux (J) in the plane of the membrane, eq. 7. In an applied EF, the combined effect of a molecule's electrophoretic flux ($E \bullet C \bullet \mu_{ep}$) and electro-osmotic flux ($E \bullet C \bullet \mu_{eo}$) builds the gradient, where E is field strength, C is the local concentration, and μ_{ep} and μ_{eo} are electrophoretic and electro-osmotic mobilities, respectively. Most commonly, electrophoretic and electro-osmotic forces are in opposite directions for negatively charged surface proteins. Diffusive flux, ($D \bullet \Delta C/\Delta x$), tends to collapse the gradient. The flux model can be applied to multiple geometric shapes including the surface of spheres or disks, in order to model electromigration on rounded or flattened regions of cells, respectively.

Eq. 7 $$J = E \bullet C(\mu_{ep} - \mu_{eo}) - D\Delta C/\Delta x$$

Electrophoretic mobility is proportional to the extracellular surface exposed charge (z) of the macromolecule, its diffusion coefficient (D) in the plane of the membrane and Faraday's constant (F), and inversely proportional to the gas constant (R) and temperature (T) according to the Einstein relation.

Eq. 8 $$\mu_{ep} = zDF/RT$$

Charge (z) can be estimated from molecular structure, and diffusion coefficient (D) for plasma membrane macromolecules of many sizes has been measured using fluorescence tracking techniques. Diffusion coefficients for membrane macromolecules can also be estimated using the

Saffman-Delbrück model (Saffman and Delbrück, 1975; WeiB et al., 2013). Macromolecules with lower diffusion coefficients would tend to have weaker electrophoretic mobility and slow the collapse of gradients by having lower diffusive flux, eq. 7.

Electro-osmotic mobility of a plasma membrane, surface exposed macromolecule, is dependent on electrically generated water flow at the cell surface. Drag forces opposing electro-osmotic migration are exerted on regions of the macromolecule embedded in the plasma membrane and surrounded by cytosol. Therefore, electro-osmotic mobility is dependent on the relative size of a macromolecule in these three regions and the local viscosities. The drag relationship is determined using Stokes' drag for the different regions of the macromolecule. The force (F_1) on the external domain of the macromolecule will depend on the difference between electro-osmotic flow (EOF) and molecular velocity (v_1). Opposing drag forces are exerted on transmembrane macromolecules by the plasma membrane (F_2) and cytosolic fluid (F_3). At equilibrium, the net force on the macromolecule equals zero, as shown in eqs. 9 and 10.

Eq. 9 $$F_1 - F_2 - F_3 = 0$$

Eq. 10 $$6\pi\alpha_1\eta_1(EOF - v_1) - 6\pi\alpha_2\eta_2 v_2 - 6\pi\alpha_3\eta_3 v_3 = 0$$

Different regions of the macromolecule can be approximated to volume equivalent spheres (Hölzer and Sommerfeld, 2008) for use in Stokes' drag equation. Also, the velocity of the three components of the transmembrane macromolecule are equal i.e. v1 (extracellular) = v2 (intramembranous) = v3 (cytosolic). Therefore, the velocity of the macromolecule is proportional to EOF and local drag.

Eq. 11 $$v_1 = EOF \bullet \frac{\alpha_1\eta_1}{\alpha_1\eta_1+\alpha_2\eta_2+\alpha_3\eta_3}$$

According to eq. 11, the velocity of the macromolecule increases toward the electro-osmotic flow rate when the size of the extracellular domain (α_1) is relatively large in comparison to its domains in the plasma membrane (α_2) and cytosol (α_3). Also, under normal conditions the viscosity of the plasma membrane (η_2) poses significantly greater drag compared to the viscosities outside (η_1) or inside (η_3) cells.

EOF near a cell surface is proportional to electrical permittivity ($\varepsilon_r\varepsilon_0$) and zeta potential of the cell surface (ζ), and is inversely proportional to medium viscosity (η_1) (Soderman and Jonsson, 1996) as shown in eq. 12. Cell surface zeta potential can be measured using whole cell electrophoresis and medium viscosity can be measured (Kobylkevich et al., 2018). Eq. 11 is combined with eq. 12 to solve electro-osmotic mobility (μ_{eo}).

Eq. 12
$$EOF = E \bullet \frac{\epsilon_r \epsilon_0 \zeta}{\eta_1}$$

Eq. 13
$$v_1 = E \bullet \frac{\epsilon_r \epsilon_0 \zeta}{\eta_1} \bullet \frac{\alpha_1 \eta_1}{\alpha_1\eta_1+\alpha_2\eta_2+\alpha_3\eta_3}$$

Eq. 14
$$\mu_{\mathrm{eo}} = \frac{v_1}{\mathrm{E}} = \frac{\epsilon_r \epsilon_0 \zeta}{\eta_1} \bullet \frac{\alpha_1 \eta_1}{\alpha_1\eta_1+\alpha_2\eta_2+\alpha_3\eta_3}$$

Equations 7, 8 and 14 are useful for helping to determine equilibrium between electrophoretic mobility and electro-osmotic mobility, and therefore enable prediction whether a protein will electromigrate cathodally or anodally. In the case when there is no net molecular flux in the presence of an EF, no concentration gradient exists and eq. 7 simplifies to $\mu_{ep} = \mu_{eo,}$ or:

Eq. 15
$$\frac{\mathrm{zDF}}{\mathrm{RT}} = \frac{\epsilon_\mathrm{r} \epsilon_0 \zeta}{\eta_1} \bullet \frac{\alpha_1 \eta_1}{\alpha_1\eta_1+\alpha_2\eta_2+\alpha_3\eta_3}$$

Eq. 16 $$z = \frac{RT\epsilon_r\epsilon_0\zeta}{DF} \bullet \frac{\alpha_1}{\alpha_1\eta_1+\alpha_2\eta_2+\alpha_3\eta_3}$$

Eq. 16 is useful for predicting the surface macromolecules that are most likely to accumulate on the cathode side or the anode side of the cell based on their physical properties. Macromolecules with extracellular surface charge more negative than 'z' will migrate anodally as their electrophoretic mobility will be greater than their electro-osmotic mobility. Appendix A, Table 4 provides a complete list of the variables and constants used to derive this model.

Electromigration of tdTomato-GPI

In order to test the flux model, we compared its predictions to the measured electromigration of a known cell surface protein, tdTomato-GPI, illustrated in Fig. 6, (molecule 'd'). The cellular distribution of tdTomato-GPI was determined on spherical CHO cells using laser scanning confocal microscopy, before and after exposure to EFs. Electromigration of tdTomato-GPI was altered by applying EFs of different magnitude and by performing the experiments in saline at different pH. Measurements on single cells at neutral pH indicate that tdTomato-GPI electromigrates to the cathode, Fig. 7.

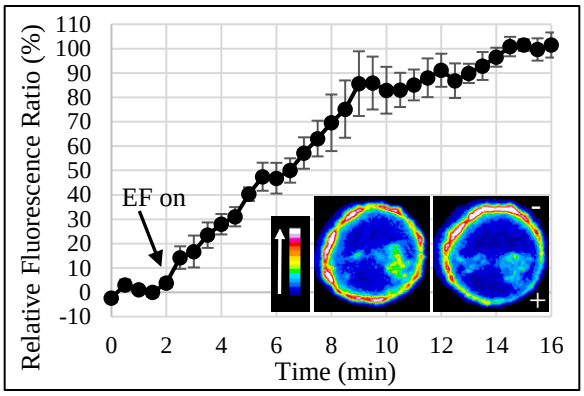

Figure 7. Cathodal electromigration of tdTomato-GPI reaches steady state rapidly.

The average relative cathode/ anode fluorescence ratio for surface tdTomato-GPI was determined before and during electromigration. EFs were applied immediately after acquiring the 2 min. time point. The time to reach 90% of steady state is 7 min. Error bars represent the S.E (n=5). The inset shows pseudo-colored localization of tdTomato-GPI on a single cell before EF application (left) and after reaching steady state (right) in an applied EF. The white arrow next to the color bar indicates increasing brightness/density of tdTomato-GPI.

Comparison of the steady state plasma membrane fluorescence at the edges of the cells yielded cathode/anode fluorescence ratios of 1.1 ± 0.03 at 100 mV/mm, 1.3 ± 0.05 at 300 mV/mm

and 1.96 ± 0.12 at 1000 mV/mm, Fig. 8A. The average cell diameter for the different conditions was 15.1 ± 0.3 µm (n=72) for 100 mV/mm, 14.9 ± 0.3 µm (n=66) for 300 mV/mm and 15.0 ± 0.2 µm (n=66) for 1000 mV/mm. In EFs of 100-300 mV/mm, the cathode/anode fluorescence ratio of tdTomato-GPI was not always greater than 1, Fig. 8B. However, increased EF strength at 1000 mV/mm caused nearly all cells to show a cathode/anode fluorescence ratio greater than 1. We conclude that at lower field strengths, the rapid diffusion of tdTomato-GPI dominates, giving rise to a more nearly random distribution of the protein on the cell surface, especially for cells with less negative zeta potentials.

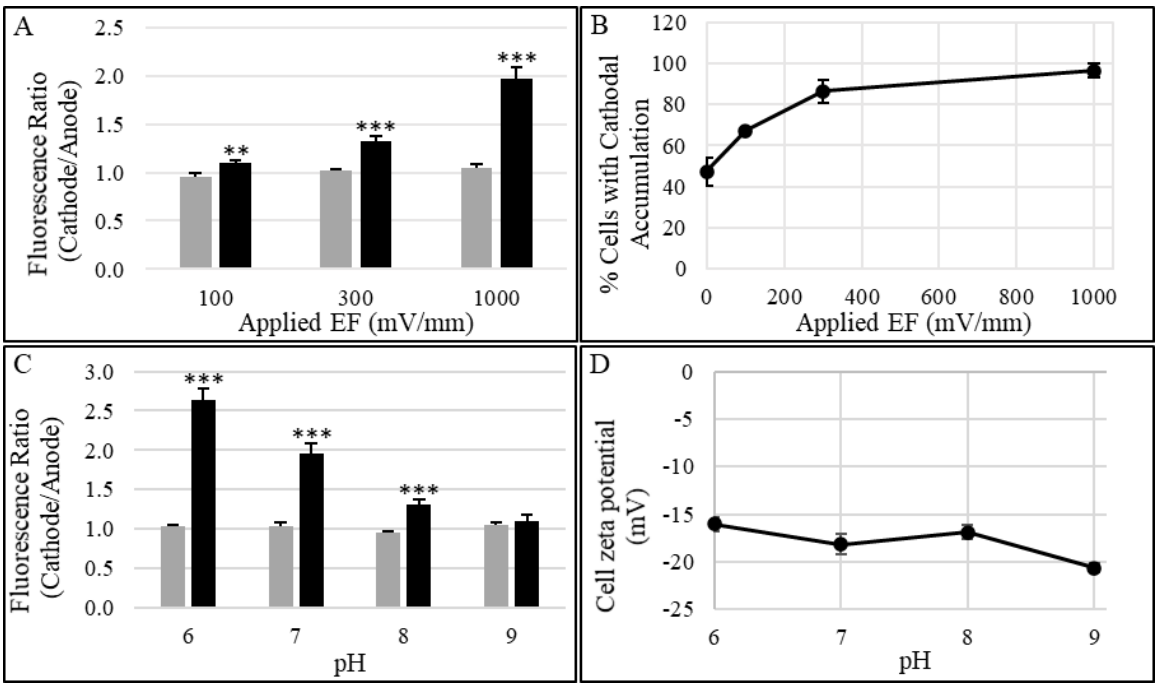

Figure 8. Steady state electromigration of tdTomato-GPI is affected by voltage and pH. A. Relative accumulation of tdTomato-GPI before (gray) and after (black) exposure to EFs of different strength. The asymmetry is expressed as a ratio of the cathode/anode plasma membrane fluorescence. B. Greater field strength is associated with a greater percentage of cells showing cathodal accumulation. C. Cathodal accumulation of tdTomato-GPI decreases with increasing pH. D. The zeta potential of tdTomato-GPI expressing CHO cells changes by a few mV over the pH range 6-9. ** $p < 0.005$, *** $p < 0.0001$.

A second method used to perturb extracellular accumulation of tdTomato-GPI was performed by altering its surface charge by changing the pH of the surrounding media. The net predicted surface charge on tdTomato-GPI changed from +1.7, -3.3, -4.2, -5.9 over the pH range 6, 7, 8 and 9, respectively, increasing electrophoretic mobility to the anode with increasing pH. The cathodal accumulation of tdTomato-GPI was greatest at pH 6 and decreased with increasing

pH, Fig. 8C. The average cell diameter for the experimental conditions with EF was 15.5 ± 0.3 μm (n=63) for pH 6, 15.0 ± 0.2 μm (n=66) for pH 7, 15.2 ± 0.3 μm (n=56) for pH 8 and 15.3 ± 0.4 μm (n=39) for pH 9. The pH also influenced the measured average zeta potential of the cells, Fig. 8D. However, the average zeta potential of the tdTomato-GPI expressing CHO cells differed by less than a few mV at different pH, consistent with the fact that a majority of protein surface charge is determined by chemical moieties with pKa values outside this pH range (Mehrishi and Johann, 2002).

Using measured and predicted parameters of tdTomato-GPI and the plasma membrane surface we performed a best fit match between eq. 7 and the steady state accumulation of tdTomato-GPI. Steady state values of the cathode/anode ratio of tdTomato-GPI in different field strength and pH were given equal weight when minimizing the sum of the squares of the differences to find the best match, except for results acquired at pH 6 which showed significant deviation.

The time course of the concentration changes at 1 min. intervals is shown in Fig. 9A, for the 15 μm diameter, modeled spherical CHO cell, using an EF of 100 mV/mm with the cathode on the right side. The cathode/anode ratio of tdTomato-GPI localization was determined using the extreme 15% on each edge of the cell facing the electrical poles.

There is relatively close alignment between the predicted and measured steady state cathode/anode ratios of tdTomato-GPI, Fig. 9B&C, when membrane viscosity is 450 mPa•s and the diffusion coefficient of tdTomato-GPI is 0.652 $\mu m^2/s$. The greatest deviation between the modeled and the measured values occurs at pH 6 where the predicted cathode/anode ratio is 14.2 and the measured ratio is only 2.6. At pH 6, tdTomato-GPI possesses a net positive charge so both electrophoresis and electro-osmosis are driving the macromolecule to the cathode. However, the cationic tdTomato may be adhering to surrounding negatively charged macromolecules thus impeding electromigration of tdTomato-GPI to the cathode. A related anomaly was reported during electromigration of the cationic lipid, DiI, that accumulated at the anode side of cells in applied EFs (McLaughlin and Poo, 1981). The unexpected, backward electromigration of DiI to the pole

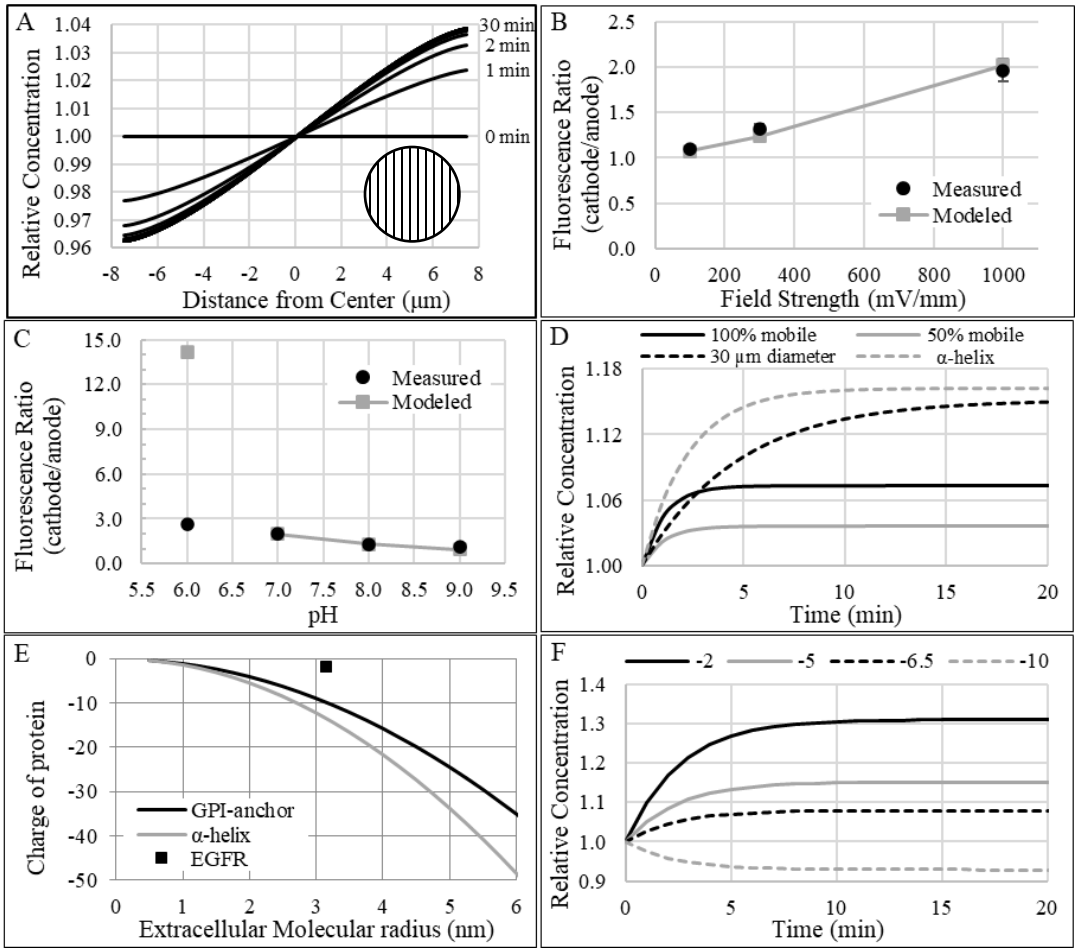

Figure 9. Modeled results of cell surface protein electromigration. A. Predicted relative surface concentration changes for tdTomato-GPI on a spherical cell in the presence of a 100 mV/mm EF at 1 min. intervals with the cathode on the right. Inset shows the orientation of the 0.1 μm zones on the cell surface used for modeling. B. Best fit alignment of the flux model with steady state electromigration of tdTomato-GPI in different EF strength. C. Best fit alignment of the flux model with steady state electromigration of tdTomato-GPI in different pH. D. Time course of the change of the cathode/anode fluorescence ratio for 100% and 50% mobile fractions of tdTomato-GPI on a 15 μm diameter cell, on a larger 30 μm diameter cell, and after the exchange of the GPI anchor for a single, transmembrane α-helix. E. Equilibrium prediction between electrophoretic and electro-osmotic mobilities of proteins with a single GPI anchor and proteins with a single transmembrane α-helix. The graph displays the extracellular surface charge of the macromolecule necessary for electrophoresis to be in equilibrium with electro-osmosis when the extracellular domain increases in size. Monomeric EGFR without glycosylation is plotted for reference. F. Time course prediction for the electromigration of monomeric EGFR when surface glycosylation sites possess no sialic acids (-2), a sialic acid on one-third of the sites (-5), a sialic acid on half of the sites (-6.5) and a sialic acid on all fully glycosylated sites (-10), yielding the net surface charge as indicated.

of similar charge, was explained due to its adherence to surrounding negatively charged surface proteins that migrated to the anode under the conditions used (McLaughlin and Poo, 1981).

A smaller deviation between the modeled and the measured values occurs at pH 9, Fig. 9C, where the model predicts a weak reversal of tdTomato-GPI to the anode, i.e. cathode/anode ratio

of 0.95. At pH 9, the measured cathode/anode ratio for tdTomato-GPI was 1.1 ± 0.06 when exposed to an EF of 1000 mV/mm and was not significantly different from the cathode/anode ratio in the absence of EFs, 1.05 ± 0.04 ($p > 0.4$, two-tailed t-test). While electromigration was significantly reduced at pH 9, Fig. 9C, it was not measurably reversed as predicted by the model. Exploration of anodal electromigration of tdTomato-GPI at pH 10 was not possible as cells detached from the bottom of the chamber and showed plasma membrane ruffling at the higher pH.

The values used in the model closely predict the steady state cathode/anode fluorescence ratio of tdTomato-GPI at 100, 300 and 1000 mV/mm. Therefore, it should be reliable to help predict steady state values that occur at 10 mV/mm near the threshold for galvanotaxis. At this very weak field strength, the model predicts an average cathode/anode ratio of 0.7% above unity on a 15 μm diameter cell at pH 7.

Further predictions by the model were performed using a 100 mV/mm EF and similar values for diffusion coefficient and membrane viscosity as used above. Fig. 9D shows predicted time courses of the change in cathode/anode fluorescence ratio for a 15 μm diameter cell with 100% and 50% mobile fractions of tdTomato-GPI, for a cell with twice the diameter, i.e. 30 μm, and for a surface tdTomato protein with a single α-helix, transmembrane domain, rather than a single GPI lipid anchor. These predictions are based on the fact that 100% of the macromolecule of interest is freely diffusing in the plasma membrane. Fig. 9D shows that when only 50% of tdTomato-GPI is freely diffusing and 50% is immobilized, that the time course remains similar, but the steady state cathode/anode ratio of the macromolecule is reduced.

The time to reach 90% of steady state ($t_{90\%}$) for the best fit model on 15 μm average diameter CHO cells, used in this study, takes only a few minutes, Fig. 9D. However, on a larger cell with a diameter of 30 μm, steady state is reached in about 10 minutes and the ratio is about twice as great compared to a 15 μm diameter cell. Previous studies monitoring electromigration of ConA receptors reported that steady state was reached within about 10 min on cells with diameters of 20-40 μm (Poo, 1981). These observations indicate that the time course and magnitude of steady

state of electromigration is largely dependent on cell dimensions. Change in direction of migrating human keratinocytes appears to reach steady state within 15 min. (Nishimura et al., 1996). Similar studies on zebrafish keratocytes show that a steady state response is reached at about 20 min. after application of 125 mV/mm EFs, Fig. 10. We conclude that significant electromigration of surface macromolecules precedes or occurs at the same time as significant changes in directed migration of cells.

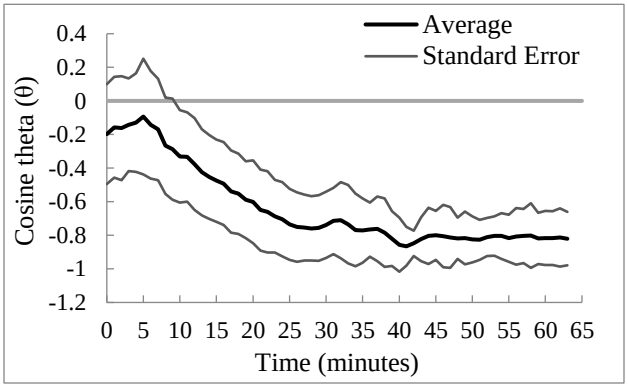

Figure 10. Time course for the cathodal migration of zebrafish keratocytes. Directional migration was monitored by calculating the mean cosine theta on a minute-by-minute basis. The EF was applied beginning at 5 min. The mean cosine theta (black) is plotted between the S.E. (gray).

The time course for electromigration of tdTomato was also predicted as if it had a single, transmembrane α-helix, Fig. 9D. The transmembrane α-helix would have approximately twice the drag imposed by the plasma membrane, considering the cylindrical α-helix spans the bilayer and possesses an outer diameter of approximately 1.2 nm (Nelson and Cox, 2008) while the GPI anchor is inserted in the outer leaflet of the bilayer and possesses a total diameter of about 0.9 nm (Kucerka et al., 2006). Proteins of similar size as tdTomato with a single transmembrane α-helix, possess diffusion coefficients half as large as the same protein with a GPI anchor in place of the transmembrane helix (Zhang et al., 1991). Based on these modifications to the model, redistribution of tdTomato with a single, transmembrane α-helix, is predicted to reach steady state within 10 minutes at 100 mV/mm and increase the cathode/anode ratio to 16% above unity compared to 7.3% above unity for the GPI-anchored protein. We conclude that for this example, increasing drag in the plasma membrane has a greater effect in reducing electrophoretic mobility than it does in reducing electro-osmotic mobility. We then applied the model to more complex cell surface macromolecules.

Using eq. 10, we predicted the magnitude of the protein surface charge required to generate an electrophoretic mobility equal and opposite to electro-osmotic mobility when only extracellular protein size was changed. Fig. 9E displays a curve for GPI-anchored surface proteins and surface proteins with a single transmembrane α-helix. The figure shows that a more rapid increase (nonlinear) in negative surface charge is required to balance the increase in extracellular, outer radius. When extracellular surface charge for a macromolecule is less negative than a point on the curve, electro-osmotic mobility to the cathode will dominate, e.g. EGFR. Electrophoretic mobility to the anode will dominate when surface charge is more negative. Surface proteins with a single, transmembrane α-helix, require greater negative surface charge to electromigrate to the anode than GPI-anchored proteins.

In attempts to compare the flux model with electromigration of known proteins we predicted the redistribution of monomeric, epidermal growth factor receptor (EGFR), a protein with intracellular and extracellular domains of nearly equal size, that electromigrates to the cathode in applied EFs and enhances cathodal migration in the presence of epidermal growth factor (EGF) (Fang et al., 1999; Yan et al., 2009; Zhao et al., 1996; Zhao et al., 1999b; Zhao et al., 2002a). EGFR appears to electromigrate to the cathode within 10-15 min. (Fang et al., 1999; Zhao et al., 1999b). The added challenge is that human EGFR possesses eleven canonical N-glycosylation sites and twelve O-glycosylation sites except none of the predicted O-sites are glycosylated (Cummings et al., 1985). Of the N-glycosylation sites in model human A431 cells, only eight sites are fully glycosylated, two are not glycosylated and one is partially glycosylated (Zhen et al., 2003). Terminal addition of negatively charged, N-acetylneuraminic acid, i.e. sialic acid, varies considerably between sites (Zhen et al., 2003). However, only one-third to one-half of the EGFRs in these cells contain sialic acids and those that are sialylated, have no more than 1 or 2 sialic acids per protein (Cummings et al., 1985). Glycosylation increases extracellular size and promotes stronger electro-osmotic mobility. However, addition of negatively charged sialic acids increases the protein's electrophoretic mobility. In the absence of sialic acids the flux model predicts that

EGFR accumulates to the cathode, Fig. 9F, with a cathode/anode ratio of 1.3 at 100 mV/mm, reaching steady state in less than 10 minutes, in close agreement with previous reports on migrating cells (Fang et al., 1999; Zhao et al., 1999b). In the presence of greater amounts of sialic acids, the cathode/anode ratio decreases. According to the flux model, at least 7 of the glycosylation sites on a single protein require a negatively charged sialic acid before electrophoretic mobility dominates electro-osmotic mobility, assuming cellular zeta potential does not change. If all eight of the fully glycosylated sites contain a negatively charged sialic acid, EGFR would electromigrate anodally, Fig. 9F, albeit forming a less steep, anode high gradient compared to EGFR without sialic acids or even with three sialic acids. This conclusion is consistent with the role of EGFR in promoting a greater migratory response to the cathode in the presence of EGF (Zhao et al., 1999b) or activated EGFR (Yan et al., 2009). In addition, application of the flux model to the threshold EF strength of 10 mV/mm, indicates a cathode/anode ratio 2.7% greater than unity in the absence of sialic acids on EGFR.

Other surface macromolecules like lipids may also be redistributed by weak EFs. Lipid rafts polarize to the leading edge of cathode and anode directed cells (Lin et al., 2017). Assuming a negative cell surface zeta potential as measured on CHO cells in this study, the flux model predicts cathodal migration for ganglioside GM1, considering the weak extracellular surface charge and combined size of extracellular sugars. Anodal migration of ganglioside GM1 could occur on cells with less negative cell surface zeta potentials.

Electromigration of other membrane proteins has been characterized during galvanotaxis. Some of these proteins have been listed in Table 2 along with their physical properties. The structural images in the top row show the insertion of the proteins in the Outer and Inner leaflets of the plasma membrane lipid bilayer. The table lists the information for the monomers of EGFR and bFGFR even though the structures of the dimers are shown. EGFR (Fang et al., 1999; Zhao et al., 1999b) and nAChR (Chernyavsky et al., 2005; Stollberg and Fraser, 1990) electromigrate

Table 2. A comparison of the physical properties of representative plasma membrane spanning proteins.*Total estimated mass is the sum of the protein mass and the polysaccharide mass from the protein's external predicted glycosylation sites. PDB IDs for protein structure: ENaC (6BQN), nAChR (2BG9), EGFR (3NJP (extracellular), 2JWA (membrane), 2GS6 (intracellular)), bFGFR (1FQ9 (extracellular), 3ky2 (intracellular)), TGFR β1 (1M9Z (extracellular), 6B8Y (intracellular)), K ir 4.2 (3SPI for K ir 2.2), Na/K pump (3KDP).

	ENaC	nAChR	EGFR	bFGFR	TGFRβ1	K_{ir} 4.2	Na/K Pump
Reference proteins	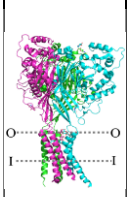	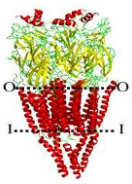	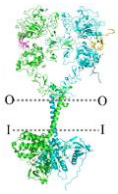	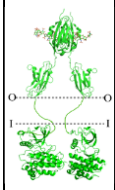	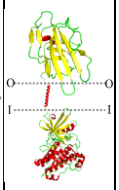	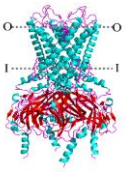	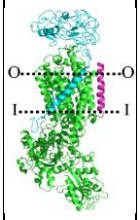
Transmembrane domains	6	20	1	1	1	8	12
Total protein mass (kD)	223	277	134	82	56	170	154
Protein mass (ext.) (kD)	157	142	69	29	14	23	38
Protein mass (int.) (kD)	50	78	62	48	41	128	88
External surface charge	-13	-6	-2	-8	-1	-19	-11
Ext. glycosylation sites	56	30	24	11	13	8	16
Total estimated mass (kD)*	252	192	113	52	30	38	68

cathodally within 15 min. Cathodal accumulation of ENaC (Yang et al., 2013) can be measured within an hour and robust cathodal accumulation of bFGFR and TGFRβ1 occurs more slowly, although lower levels appear after brief application of EFs (Zhao et al., 1999b). The inward rectifying K^+ channel, K_{ir} 4.2, does not electromigrate to either pole (Nakajima et al., 2015). All cathodal migrating proteins have large extracellular domains with relatively weak surface charge compared to K_{ir} 4.2 which has a very small extracellular domain and large transmembrane and intracellular domains. Glycosylation sites and new estimates for glycoprotein molecular weight have been listed as if all predicted sites are glycosylated with 2.5 kD sugars for N-linked sugars and 1.2 kD sugars for O-linked sugars.

Proteomic Analysis

a. Physical Properties of Surface Proteins on Zebrafish Keratocytes

In attempts to identify candidates for the EFR on zebrafish keratocytes, a model system for galvanotaxis, we screened the zebrafish proteome and identified the plasma membrane surface

proteins using TOPCONS and CELLO programs. Proteins were sorted into 3 categories including 6,496 transmembrane proteins, 269 extracellular integral membrane proteins and 214 GPI-anchored proteins. Proteins containing both transmembrane domains and GPI-anchors are listed as transmembrane proteins. In an attempt to restrict proteins to epidermal keratocytes, the protein pool was confined to similar proteins found in human keratinocytes (Reemann et al., 2014), another migratory model system with high protein homology to zebrafish (Howe et al., 2013).

This reduced the protein pool to 5,038 transmembrane proteins, 152 integral membrane proteins and 120 GPI-anchored proteins. Additional screening was performed to remove proteins with high similarity e.g. isoforms of a receptor or channel subunit, resulting in a final list of proteins including 2,169 transmembrane, 118 integral membrane and 83 GPI-anchored proteins.

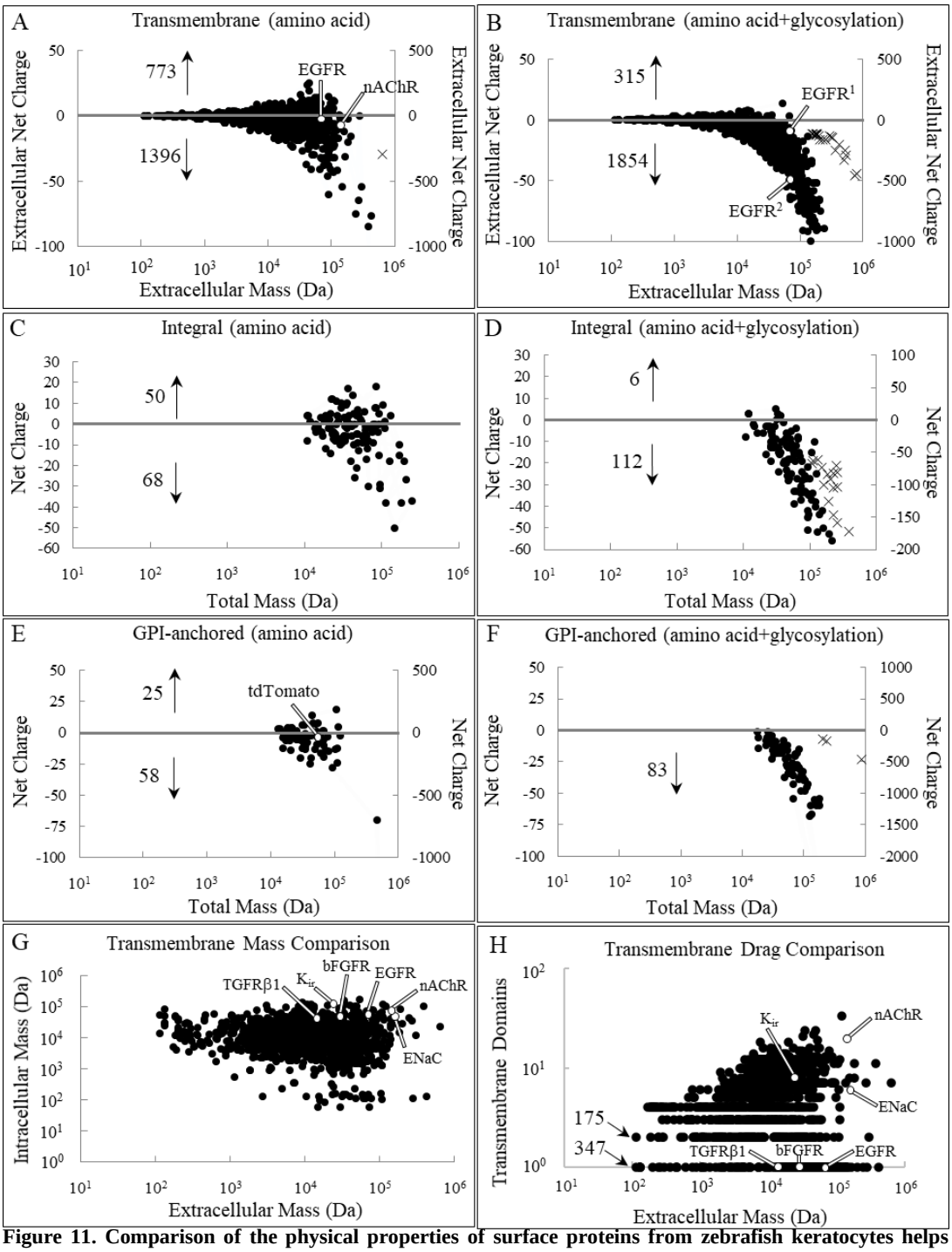

Figure 11. Comparison of the physical properties of surface proteins from zebrafish keratocytes helps predict the direction of protein electromigration. Distribution of the extracellular surface charge and mass for surface proteins classified as transmembrane (A), integral (C) and GPI-anchored (E). (●) left y-axis data points, (×) right y-axis data points. For reference, the cathode migrating, non-glycosylated EGFR and nAChR are added to A and the cathode migrating tdTomato-GPI is added to E. Estimated changes in extracellular charge and mass after glycosylation of all potential N- and O- sites for transmembrane (B), integral (D) and GPI-anchored (F) proteins. In B, $EGFR^1$ represents glycosylated EGFR with a single sialic acid on each full length, N-linked sugar, and $EGFR^2$ represents glycosylated EGFR with three sialic acids on each N-linked sugar and one sialic acid on each O-linked sugar. G. Transmembrane protein distribution comparing the masses of the extracellular and the intracellular domains. H. Transmembrane protein distribution comparing extracellular mass and the number of transmembrane domains.

The location and primary structure of the proteins are used to determine molecular weight of extracellular and intracellular domains, and net charge of the extracellular domains, Fig. 11A, C & E. Two y-axes are used to plot the charge. While many proteins possess weak charge, displayed by ● using the left y-axis, some proteins contain very high charge, displayed by × using the right y-axis. Based on extracellular primary structure alone, 24% of the transmembrane proteins have a net positive charge while 12% are neutral, possessing a net charge with ± 0.5 of zero. 34% of extracellular, integral membrane proteins have a net positive charge and 7% are neutral. 24% of the GPI-anchored proteins have a predicted net positive charge from amino acids alone, and 6% of the proteins are neutral. The nonglycosylated forms of EGFR and nAChR have been highlighted as reference points in Fig. 11A, and tdTomato-GPI has been highlighted in Fig. 11E.

In order to get an idea for the impact of glycosylation on the protein populations, all potential external N-linked glycosylation sites were populated with a 2.5 kD sugar (An and Lebrilla, 2011; Imperiali and O'Connor, 1999) and capped with 3 negatively charged sialic acids, and all external potential O-linked sites were populated with a 1.2 kD sugar (An and Lebrilla, 2011; Van den Steen et al., 1998) and capped with 1 negatively charged sialic acid, Fig. 11B, D and F. These modifications were performed to obtain a range for the impact of glycosylation. While these modifications increased the protein mass and the negative surface charge of the extracellular domains of transmembrane proteins, 8% still showed a net positive extracellular surface charge, and 7% remained neutral. We conclude that of all the parameters required to determine electromigration for a surface protein, the amount of glycosylation and amount of charge due to glycosylation are the most difficult to predict.

Electro-osmotic mobility increases with increasing extracellular protein size and decreases with increasing intracellular protein size and the number of transmembrane domains, eq. 8. Fig. 11G displays the distribution of extracellular domain mass to intracellular domain mass. The proteins from Table 2 have been added to Fig. 11G and reflect a strong association between extracellular size and electro-osmotic mobility. From right to left on Fig. 11G, proteins with the

largest extracellular domains like nAChR, EGFR and ENaC have high electro-osmotic mobilities, and are known to accumulate cathodally compared to bFGFR, TGFRβ1 and K_{ir} 4.2 that have smaller extracellular domains.

Transmembrane domains increase drag and reduce electro-osmotic mobility significantly greater than intracellular domains due to the drag imposed by the viscosity of the plasma membrane. While 16% of the zebrafish keratocyte plasma membrane proteins have only a single transmembrane α-helix, Fig. 11H, 50% have 4 or fewer. Despite large numbers of transmembrane domains, the nAChR which has 20, electromigrates to the cathode (Chernyavsky et al., 2005; Stollberg and Fraser, 1990), due to its large extracellular domains and weak extracellular charge, Table 2. Extracellular size appears to have a stronger association with electro-osmotic mobility than drag imposed by the plasma membrane.

b. Summary of Gene Ontology (GO)

GO terms for molecular function, listed in Table 3, were determined to help categorize the range of functions for the surface proteins identified above. Only categories that contained greater than 1% of the proteins in their group are listed. Also, proteins are not exclusive to a single GO category. G-protein coupled receptors are the most numerous of the transmembrane proteins, comprising 16% of that group. Many other proteins overlap within the 'G-protein coupled' and 'transmembrane signaling' category and are associated with promoting chemotaxis and asymmetric cellular signaling thus enabling the establishment of cell polarity, e.g. chemokine binding, neurotransmitter receptor binding, kinase binding, calcium ion binding, and collagen binding activities. Proteins within the 'ion channel' and 'transmembrane transport' category are associated with either ion homeostasis, intracellular signaling or cell migration through selective ion channels such as K^+, Ca^{2+}, and Na^+. Transmembrane proteins within the 'structural molecule', 'peptidase', 'hydrolase' and 'protein binding' categories have overlapping functions associated with cell-cell

adhesion, structural integrity, and cytoskeleton formation or hydrolysis, necessary for adhesion and migration in tissues.

Table 3. Gene ontology terms for surface proteins of zebrafish epidermal keratocytes show functional categories in highest abundance.

Transmembrane Molecular Function	#	**Integral Protein Molecular function**	#	**GPI-anchored Molecular function**	#
G-protein coupled activity	348	Miscellaneous	17	Peptidase activity	14
Transmembrane transporter activity	188	Ion binding activity	15	Ion binding activity	12
Transferase activity	153	Hydrolase activity	13	Hydrolase activity	12
Miscellaneous	116	Peptidase activity	9	Receptor binding activity	11
Ion binding activity	106	Transferase activity	9	Miscellaneous	7
Transmembrane signaling activity	88	Nucleotide binding activity	6	Protein binding activity	5
Oxidoreductase activity	83	Protein binding activity	4	Nucleotide binding activity	3
Ion channel activity	78	Oxidoreductase activity	3		
Hydrolase activity	64	Receptor binding activity	3		
Structural molecule activity	63				
Nucleotide binding activity	40				
Peptidase activity	37				
Protein binding activity	34				
Without GO terms	907	Without GO terms	60	Without GO terms	37

The integral membrane proteins are most abundant in ‘ion binding activity’, making up about 13% of the categorized proteins. This category of proteins is mostly associated with cellular signaling via binding to metal ions and cofactors, such as zinc, calmodulin, NADP, glycosyl group transfer activity and nitric oxide synthase activities. ‘Peptidase activity’ is the most abundant category within the GPI-anchored proteins, making up about 17% of the total. Proteins within the ‘peptidase’, ‘hydrolase’ and ‘peptide binding’ categories overlap and are associated with cytoskeleton formation or hydrolysis and cell signaling via cofactor binding, such as endopeptidase activity, ester bond hydrolysis, glycosyl bond hydrolysis and metal ion binding activities. During categorization, 42% of the transmembrane proteins, 51% of the integral membrane proteins and

45% of the GPI-anchored proteins are either missing a corresponding gene ID, missing a GO term or well-defined GO term, or possess a combination of all three limitations for identifying their function. In summary, all three categories contain plasma membrane surface proteins that appear to be involved with signaling or structural integrity that could be involved with generating cellular polarity or directed migration.

DISCUSSION

We have measured electromigration of a plasma membrane surface protein under different conditions and used modeling to understand the roles of its physical properties in directing its electromigration. We have also used bioinformatics tools to collect and predict physical properties for other surface proteins to expand our understanding of surface protein electromigration and its involvement with directing galvanotaxis and galvanotropism. The electromigration model has often been compared to the membrane depolarization model, a model that has included activation of transmembrane voltage sensors, alteration of transmembrane enzyme function or changing of the electrochemical gradient of ions across the plasma membrane (McCaig et al., 2009; Robinson, 1985; Weaver and Astumian, 1990). However, in DC EFs near 10 mV/mm, the lower threshold for migratory cells, an electrical potential difference of only 10 - 300 μV exists between two edges of a cell, 1-30 μm apart. Such weak depolarizations perpendicular to the plane of the plasma membrane are insufficient to activate plasma membrane voltage sensors or voltage-gated ion channels considering their poor sensitivity near resting membrane potential (Bezanilla, 2000; Murata et al., 2005; Sasaki et al., 2006). However, even in weak EFs, charge continues to move parallel to the cell surface, promoting electrophoresis and electro-osmosis, resulting in electromigration of surface macromolecules.

The molecular flux model presented here can predict the asymmetric steady state redistribution of tdTomato-GPI on spherical CHO cells for different field strengths and within the pH range from 7-9, Fig. 9B+C. The flux model essentially compares charge and size. Charge is compared between the extracellular surface of the macromolecule and the overall surface of the cell. Size is compared between the extracellular region of the electromigrating macromolecule, and its domains embedded within the plasma membrane and cytosol. The greater the negative extracellular surface charge of the macromolecule, the greater the electrophoretic mobility toward

the anode, eq. 8 and Fig. 8C. The greater the dimensions of the extracellular domain of the macromolecule, the greater the drag to move the macromolecule by electro-osmosis, eq. 14. In the absence of extracellular glycosylation, an overwhelming majority of surface proteins are predicted to electromigrate to the cathode due to their large extracellular domains and weak net extracellular charge, Fig. 11A, C & E. Extracellular glycosylation itself adds size and drag to promote electro-osmotic mobility, eq. 14. However, the addition of negative charge by terminal sialylation of N- or O-linked sugars can alter the balance to strengthen electrophoretic mobility toward the anode, eq. 8. We attempted to provide a range of molecular size and charge in Fig. 11, by adding terminal sialic acids to N- and O-linked sugars by modeling all potential N-linked sites with 3 negatively charged sialic acids and all potential O-linked sites with 1 negatively charged sialic acid. For many proteins, this is a substantial overestimation. For example, the cathode migrating EGFR has full N-glycosylation on only 8/11 potential sites and no sugars on its 12 predicted O-linked sites in the model A431 human epidermal cell line (Cummings et al., 1985). Of the predicted N-linked sites, most were without sialic acids and only 1-2 sialic acids were measured on any single EGFR protein (Cummings et al., 1985; Zhen et al., 2003), consistent with cathodal migration of EGFR on A431 cells (Guigni et al., 1987). Similarly, multiple subunits of the nAChR (Lindstrom et al., 1979) and the ENaC (Hughey et al., 2003) possess varying degrees of glycosylation and few sialic acids. All three surface proteins electromigrate to the cathode in applied EFs and are predicted to do so by the flux model due to the low amount of extracellular, negative surface charge. Even with the overestimation of N- and O-linked glycosylation shown in Fig. 11, it is surprising to see that there are a significant number of proteins with predicted net positive extracellular charge, indicating cathode-directed electrophoresis and electro-osmosis for those proteins. Of all parameters that are required to determine the dynamics of electromigration of surface proteins, the extent of surface glycosylation is the most challenging to predict.

Cell surface proteoglycans containing heparan sulfate or chondroitin sulfate have significant negative charge and accumulate anodally (Huang et al., 2017) due to their high

electrophoretic mobility. Heparan sulfate proteoglycans (HSPGs) can be unusually large with protein cores ranging from 30-400 kD with an additional 40-300 sugar residues on their heparan sulfate chains extending 20-150 nm (Sarrazin et al., 2011) making them very challenging to model. In addition, many proteoglycans are immobilized through connections to the cytoskeleton or extracellular matrix (Sarrazin et al., 2011). Very high electro-osmotic flow would be necessary to overcome the electrophoretic mobility and direct freely diffusing HSPGs to the cathode. Despite possessing anodal localization of HSPGs in applied EFs, galvanotaxis for some cell types is unresponsive to their absence (Huang et al., 2017). Also, reversing electromigration of HSPGs cannot be responsible for reversing migration of zebrafish keratocytes in the presence of low molecular weight viscous polymers because electrophoresis is enhanced in comparison to electro-osmosis and cells should have continued migrating in the same direction if electrophoresis was already dominating (Kobylkevich et al., 2018).

Over the pH range 6-9 we were able to modify the surface charge of the amino acids of tdTomato-GPI. Greater negative charge at alkaline pH reduced cathodal accumulation, Fig. 8C. A good fit to the steady state flux model occurred between pH 7-9, Fig. 9C. However, at pH 6, when tdTomato-GPI is predicted to possess a net positive charge, electromigration toward the cathode was weaker than predicted by the flux model, perhaps by interacting with the abundant local negatively charged macromolecules as described above. We conclude that alteration of molecular charge using pH can be used to alter direction of cellular migration by changing the net charge on the EFR as long as it does not alter zeta potential of the cell. Considering that the negative zeta potentials of cells are largely generated by very acidic residues (Mehrishi and Johann, 2002) electro-osmotic mobility will change very little and pH changes will have greater effect in altering electrophoretic mobility of surface macromolecules. Consistent with this hypothesis, an earlier study reported inhibition of cathodal migration of keratocytes by lowering pH over the narrow range of 6.2 to 5.8, (Allen et al., 2013). Such a dramatic shift in directed migration points to a chemical moiety with a pKa in that pH range such as histidine which has a pKa of 5.8 - 6.0

(Kozlowski, 2016) and not more acidic pKa values found in sialic acids, heparan sulfate, or chondroitin sulfate. At even lower pH, where histidine side groups are more completely positively charged, the protein may adhere to other negatively charged proteins, thus preventing electromigration and impairing reversal of cell migration to the anode as reported (Allen et al., 2013).

Other experimental procedures that alter zeta potential can have a very confusing impact on electromigration. For example, studies using inorganic Ca^{2+} channel blockers like Gd^{3+}, La^{3+} or Co^{2+} to interfere with galvanotaxis (Guo et al., 2015; Huang et al., 2009b; McCaig, 1989; Nuccitelli and Smart, 1989), may have also interfered with macromolecular surface charge and cell surface zeta potential. In relatively low levels, divalent and trivalent cations are known to reduce and even reverse the zeta potential of cells to positive values (Kinraide et al., 1998). While zeta potential can be measured, it is difficult to determine how the multivalent cations alter surface charge of specific surface macromolecules. In a second example, removing heparan sulfate from the surface of cells was shown to reduce cathodal migration by about 50% in fetal neural progenitor cells and eliminate cathode migration in brain tumor initiating cells (BTIC) (Huang et al., 2017). However, based on the flux model presented here, an alternative conclusion could be that cell surface zeta potential was significantly reduced by removing the negative charges of heparan sulfate. Therefore, electro-osmotic mobility would decrease, promoting stronger electrophoretic mobility and anodal migration of other surface macromolecules. Consistent with this idea is that further removal of negatively charged chondroitin sulfate did reverse electromigration of BTICs toward the anode (Huang et al., 2017). In addition, a large anodal accumulation of negatively charged heparan sulfate could increase the magnitude of the local negative surface potential and increase electro-osmosis on the anodal side of the cell. This would place even greater electro-osmotic flow on surface proteins to the cathode as reported using supported lipid bilayers (Liu et al., 2011).

Another important feature for macromolecule electromigration depends on the comparison between the size of its extracellular domain, and its intramembranous and cytosolic domains, eq. 14. Extracellular electro-osmotic flow has greater effect on proteins with larger extracellular domains. Even though viscosity of the lipid bilayer is significantly greater than external media, the membrane drag only exists for very small fractions of most transmembrane proteins. Nearly 50% of plasma membrane spanning proteins possess only one transmembrane α-helix (Almen et al., 2009). Also, most cytosolic domains have little impact on electro-osmosis. For example, EGFR has a cytosolic domain nearly the same size as its extracellular domain, however, the electro-osmotic mobility of monomeric EGFR is less than 1% different, compared to a similar transmembrane protein with no cytosolic domain. Plasma membrane drag increases for G-protein-coupled receptors that possess 7 transmembrane helices and certain transporters and ion channels that possess 10-24 transmembrane α-helices (Almen et al., 2009). Despite the increased drag, the nAChR and the ENaC with 20 and 6 transmembrane domains respectively, are known to migrate cathodally (Chernyavsky et al., 2005; Stollberg and Fraser, 1988; Yang et al., 2013) likely due to their large extracellular domains, Table 2. In contrast, the K_{ir} 4.2 channel does not appear to electromigrate to either electrical pole (Nakajima et al., 2015), most likely due to the absence of large extracellular domains, Table 2.

The most mobile macromolecules in the plasma membrane are those that are freely diffusing and not bound to cytoskeletal elements, corralled, or bound to other macromolecules. To help visualize variations in mobility, we modeled electromigration for tdTomtato-GPI under conditions where 100% and 50% of the population were freely mobile, Fig. 9D. While we kept these values constant for the duration of the model, they could be dynamic as bonds break and reform. The flux model does not account for this feature. Transient immobilization could increase the amount of time for electromigration to reach steady state (Schneider et al., 2018), helping to explain the fact that the predicted time for tdTomato-GPI to reach steady state, Fig. 9D, is much shorter than the

measured time, Fig. 7. The ENaC is another good example of delayed electromigration. ENaCs appear to modulate cathodal migration, however, cells begin migrating cathodally before cathodal accumulation of ENaCs can be detected (Yang et al., 2013). After 1 hour, the ENaC fluorescence is 14% higher on the cathode than the anode side of cells. ENaCs are commonly associated with cytoskeletal elements (Mazzochi et al., 2006), therefore halting electromigration of a fraction of the ENaC population. The freely diffusing fraction of the population would electromigrate toward the cathode. If the proteins alternated between an immobile state and a freely diffusing state, steady state asymmetry would be reached as predicted by the flux model, however it would take a greater amount of time to reach the steady state. Assuming a small fraction of ENaCs were mobile at any time, it is likely that accumulation to the cathode and removal from the anode was not easily distinguished on the high background of immobilized ENaCs.

The flux model also helps to predict the effects of pulsed EF on migrating cells. Short intermittent pulses of EF are sufficient to direct cathodal migration (Li et al., 2018) and cathodal outgrowth (Patel and Poo, 1984). Electro-osmosis is generated rapidly after application of an EF, reaching steady state in less than 1 ms (Kuang et al., 2009). Therefore, continuous DC EFs are not required to direct migration or outgrowth. A pulsed EF with a 10% duty cycle, i.e. 100 ms on and 900 ms off, could be offset by a 10-fold voltage increase in field strength, and an EF with a 1% duty cycle, i.e. 10 ms on and 990 ms off, could be offset by a 100-fold voltage increase. Also, lower, intermittent voltage application could generate gradients as long as gradient formation was not overwhelmed by diffusion and gradient collapse. This supports the idea that high voltage, brief electrical pulses, as used in the clinic, may be just as effective in promoting directed migration and wound closure as weak, DC EF, as long as the pulses have an equivalent, time-averaged DC component (Gardner et al., 1999).

Validation of the flux model enables us to make testable predictions for other surface proteins. For example, robust cathodal migration of corneal epithelial cells, keratinocytes and lung

cancer cells is dependent on cathodal accumulation and activation of EGFR (Fang et al., 1999; Yan et al., 2009; Zhao et al., 1999b; Zhao et al., 2002a). Using the model, we predict that at threshold EF of 10 mV/mm, monomeric EGFR accumulates with a cathode/anode ratio that is 2.7% greater than unity for the nonglycosylated, nonsialylated EGFR. At this low threshold, only a small fraction of cells is responding to the EF. We propose that cells with only the greatest difference between surface protein charge and negative cell surface zeta potential are able to respond to such weak EFs. For the other cells, electro-osmotic and electrophoretic mobilities are more equivalent, and diffusion can collapse gradient formation and prevent directed migration.

Applied EFs have also been shown to redistribute epithelial proteins common to their apical to basolateral organization (Cao et al., 2014). The transepithelial potential of the epidermis is positive (anode) on the basolateral side and negative (cathode) on the apical side (Barker et al., 1982; Hotary and Robinson, 1994). ENaCs accumulate on the apical side of epithelia (Hanukoglu and Hanukoglu, 2016) and Na^+-K^+ pumps most commonly accumulate on the basolateral side of epithelia (Bystriansky and Kaplan, 2007). The polarized localization of these two proteins is the minimum requirement to obtain the epidermal transepithelial potential (Messerli and Graham, 2011). While it is known that the ENaCs electromigrate to the cathode (Yang et al., 2013) consistent with their location in the apical membrane, electromigration of the Na^+-K^+ pump is not known. According to the flux model, and the physical properties of the Na^+-K^+ pump, we predict that it will electromigrate toward the anode, considering the small extracellular domains and the combined high negative surface charge of those domains, Table 2. Even greater electrophoresis to the anode is predicted when considering the high amount of negatively charged sialic acids on the β-subunit of the Na^+-K^+ pump (Munakata and Schmid, 1982; Omori et al., 1983). We hypothesize that the physical properties of these two proteins and their role in generating the transepithelial potential form a positive feedback loop to help establish and maintain electrical polarity of the epidermal epithelium. Such a feedback loop would be very important in helping to maintain cellular polarity during cell division, when adherens junctions are remodeled to accommodate

cytokinesis (Le Bras and Le Borgne, 2014), or during wound healing when the epithelium has been compromised. Cellular signaling between gap junctions in epithelial cells or other cell types may make these tissues very sensitive to applied EF (Gosak et al., 2017).

The flux model and the proteomic screen have also been useful for helping to narrow the broad range of possibilities for the EFR on zebrafish keratocytes. Under normal conditions, keratocytes migrate cathodally (Graham et al., 2013; Huang et al., 2009b). More robust cathodal migration ($\cos\theta = -0.96$) is reported in the presence of growth factors (Huang et al., 2009b) than in their absence ($\cos\theta = -0.82$) (Kobylkevich et al., 2018), supporting a weak role for growth factor receptors. However, in the presence of a low molecular weight viscous agent, when electro-osmosis is reduced and electrophoresis can dominate, the keratocytes reverse direction and migrate anodally (Kobylkevich et al., 2018). We hypothesize that a negatively charged, cathode migrating macromolecule, reversed direction to the anode when electro-osmotic flow was reduced with the viscous polymer. According to the three protein datasets mentioned in pg. 48, in the absence of glycosylation, 35.8% of the proteins that remain positively charged at physiological pH will continue migrating cathodally despite the reduction in electro-osmosis. Similarly, proteins with high extracellular negative charge that were already migrating to the anode, will display greater anodal accumulation in the viscous medium. However, there are still hundreds of surface proteins with signaling capacity or roles in extracellular adhesion that may reverse electromigration direction from cathode to anode when electro-osmosis is reduced.

CONCLUSION

We hypothesize that multiple surface macromolecules with different degrees of influence promote directed migration in applied EFs. Careful measurements and/or predictions of the physical properties of cells and cell surface macromolecules must be performed to determine the role of any particular macromolecule in directing cellular polarity during galvanotaxis and galvanotropism. The flux model presented here, supports the electromigration model for galvanotaxis and helps to identify or support migration direction for other EFR candidates.

CHAPTER 3

ELECTROKINETIC PERFUSION THROUGH 3D CULTURE REDUCES CELL MORTALITY

ABSTRACT

Cell proliferation and survival are dependent on mass transfer. *In vivo*, fluid flow promotes mass transfer through the vasculature and interstitial space, providing a continuous supply of nutrients and removal of cellular waste products. In the absence of sufficient flow, mass transfer is limited by diffusion and poses significant challenges to cell survival during tissue engineering, tissue transplantation and treatment of degenerative diseases. Artificial perfusion may overcome these challenges. In this work, we compare the efficacy of pressure driven perfusion with electrokinetic perfusion toward reducing cell mortality in 3D cultures of Matrigel extracellular matrix. We characterize electro-osmotic flow through Matrigel to identify conditions that generate similar interstitial flow rates to those induced by pressure. We also compare changes in cell mortality induced by continuous or pulsed electrokinetic perfusion. We report that continuous electrokinetic perfusion significantly reduced mortality throughout the perfusion channels more consistently than pressure driven perfusion at similar flow rates, and pulsed electrokinetic perfusion decreased mortality just as effectively as continuous electrokinetic perfusion. We conclude that electrokinetic perfusion has significant advantages over pressure driven perfusion for promoting tissue survival prior to neovascularization and angiogenesis.

INTRODUCTION

Mass transfer is one of the greatest challenges to tissue engineering (Lovett et al., 2009; Novosel et al., 2011). *In vivo,* mass transfer is performed mostly through blood and lymphatic vessels, and to a lesser extent, interstitial flow occurs in the extracellular space (Swartz and Fleury, 2007). These forms of fluid flow enhance cellular exposure to gases, nutrients, and growth factors while removing metabolic wastes, cellular detritus, and death signals. Challenges with mass transfer are also associated with degenerative diseases and during tissue transplantation when sparse or damaged vessels limit repair and regrowth (Frykberg and Banks, 2015; Novosel et al., 2011; Siemionow and Arslan, 2004). These challenges might be overcome with artificially generated interstitial flow to promote cell survival during periods of neovascularization and angiogenesis that are required for tissue survival.

In the absence of flow, mass transfer is a limiting factor in cell culture when mortality most commonly occurs through apoptosis in response to hypoxia, metabolically induced low pH, or low growth factors (Elmore, 2007; Grilo and Mantalaris, 2019). Starvation can cause autophagy (Kroemer and Levine, 2008) and more severe physical and chemical stresses can promote necrosis (Elmore, 2007). Artificial perfusion of media as low as 0.07 μm/s is reported to overcome diffusion limitations in 2D culture and increase cell proliferation by 40% (Park et al., 2011). While pressure promotes perfusion through 3D cell cultures, it also causes compaction of the tissue and increases hydraulic resistance (McCarty and Johnson, 2007; Shi et al., 2009). Charged hydrogels that mimic the native extracellular matrix show greater hydraulic resistance to physiological saline compared to neutral gels (Mattern et al., 2008). Moreover, pressure driven perfusion (PDP) is limited by drag. According to Poiseuille's Law, average flow velocity changes with the square of the distance between the walls of a particular pathway. Given the same pressure gradient across a tissue (Δpressure / length), narrow pathways in the tissue have greater resistance to flow and slower flow velocity than larger diameter pathways with lower resistance and faster flow. Therefore, flow

velocity through narrow pathways is slow and may be insufficient to promote survival, while the velocity through wider pathways is faster and may damage cells through shear stress. These limitations of pressure driven perfusion may be overcome using electrokinetic perfusion (EKP).

Applied electric fields (EFs) through isotropic, charged gels generate electro-osmotic flow (EOF) and electrophoresis without gel deformation (Grimshaw et al., 1989; Ou et al., 2014). In 2D culture, applied EFs generate EOF within nanometers of the boundary layer of cells, sufficient to redistribute surface macromolecules within minutes and activate mechanosensitive ion channels via shear stress (Graham et al., 2013; Kobylkevich et al., 2018; Sarkar et al., 2019). In 3D tissues, relatively weak EFs generate EOF that is comparable in speed to endogenous velocities of interstitial flow, 0.1-2 μm/s (Garcia et al., 1996; Garcia et al., 2003; Rupert et al., 2013b; Swartz and Fleury, 2007). EOF velocity is more uniform in narrow pathways where PDP is limited by drag. In 3D culture, we hypothesize that EKP will help cells overcome diffusion limitations and reduce cell mortality. To test this hypothesis, we have induced interstitial flow through 3D cultures in Matrigel, using pressure or electricity. We controlled the average interstitial flow rates in the gels and compared efficacy of the two methods in reducing cell mortality. Our results indicate that steady and intermittent EKP generate interstitial flow and reduce cell mortality.

MATERIALS AND METHODS

Measurement of electro-osmotic flow

EOF through Matrigel (Corning, New York) that was cast in IBIDI channel slides (IBIDI μ-slide VI 0.4 Collagen IV), was measured at ambient temperature in experimental media by tracking the dye front of neutral Texas red dextrans (3, 10, or 70 kDa). Microbial transglutaminase (Moo Gloo RM Transglutaminase, Modernist Pantry) at a final concentration of 100 μg/ml was used to crosslink Matrigel in modified Ringer's (MR) to provide strength. Addition of the transglutaminase solution diluted Matrigel to 88%. The dye front of Texas red dextran (ex./em. 595/615 nm) was tracked in the presence of DC EFs (Lambda Electronics Inc., Melville, N.Y.) and pulsed EFs using a 611 stimulator (Phipps and Bird, Inc. Richmond, VA) for 50% duty cycle and an arbitrary function generator (AFG 3021, Tektronix, Inc., Portland, OR) controlling a voltage amplifier (Model MDT693, Thorlabs Inc., Newton, NJ) for 25% duty cycle. Time-lapse images of the dye front were acquired using an Olympus FV1200 Confocal system with an IX81 inverted microscope. A MATLAB script (MathWorks, Natick MA) was used to track the dye front in successive frames and calculate the net flow velocity. EOF was calculated by subtracting the velocity of the dye in the absence of EFs from the velocity of dye in the presence of EFs. More details are provided in the Appendix B. Statistical significance was determined using unpaired t-tests.

3D Culture

Chinese hamster ovary (CHO) cells, cultured in phenol-red free Dulbecco's Modified Eagle's Medium (DMEM) with 10% FBS and 1% Pen-Strep were concentrated and mixed with the Matrigel stock. Prior to mixing, cell counts were made with a hemocytometer (Fisher Scientific) enabling determination of a final cell density of ~4.5×10^7 cells/mL or approximately 8% by volume. The mixture of Matrigel, cells, and transglutaminase was loaded into IBIDI channel slides and

allowed to gel at room temperature for 10 min. before transferring to a 37°C CO_2 incubator to complete crosslinking for 2 hours. The final Matrigel dilution is estimated to be near 54% of its original concentration. Transglutaminase in MR was added to the channel wells to promote crosslinking at the gel edges. After crosslinking, transglutaminase was rinsed from the gels with two volumes of experimental media using EOF at 1000 mV/mm for ~40 minutes each time.

Cell assays in 3D culture

Cell mortality was assessed after 48 hours in the absence of perfusion (control) and in the presence of PDP or EKP. Mortality was monitored using the cell-impermeant Propidium Iodide (PI, 20 μM) which stains nucleotides of apoptotic, autophagic, and necrotic cells as they lose membrane integrity (Chen et al., 2010; Walsh et al., 1998). Disintegrated nuclei or ruptured cells would be diluted by greater than 10-fold (Han et al., 2006; Maul and Deaven, 1977) and would be below the threshold of detection. Cells in 3D culture were exposed to PI using EOF as described above. Images of PI-stained cells (ex./em. 535/615 nm DNA bound) were collected 30 μm from the bottom of the channels using an optical section 14.5 ± 4.6 μm thick with the confocal system described above. ImageJ software was used to measure the percent area of the field of view that was covered by PI stain. Three regions of each channel were sampled twice near the inlet, center, and outlet regions to assess PI staining throughout the channel. Six channels total from at least two different experiments were used for each of the conditions that were studied. In the absence of 48 hr. perfusion, the inlet and outlet of the channel refer to the perfusion direction used to remove the transglutaminase and load the PI. For consistency, each region of the experimental channels was compared to the same region of the control channels. Relative mortality was calculated after 48 hr. as a ratio of the percent area of PI-stained cells after perfusion with the percent area of PI-stained cells from the nonperfused, control cells. The average mortality of the same batch of cells at 0 hr. was subtracted from both 48 hr. measurements. Statistical significance was calculated using unpaired t-tests.

PDP was applied through the 3D cultures with programmable syringe pumps (NE 1002X, New Era Pump Systems, Inc, Farmingdale, NY) at 300 μL/day or 60 μL/day, equivalent to 10 and 2 times the empty volume of the IBIDI channel. The experimental setup is described in Appendix B. Pressurized flow occasionally dislodged Matrigel so a protective low electroendosmosis (EEO) agarose gel (1%) was placed in the upstream well just before connecting the chambers to the syringes. Control experiments were performed using the same batch of cells in IBIDI channels. Both sides of control channels possessed equal volumes of CO_2 equilibrated, sterile media in tubing but the upstream syringes were not pressurized.

DC EFs at 300 mV/mm or 60 mV/mm were applied to cells using 9V battery banks. Battery banks and the pulsed power supplies were each connected to a series resistance substitution box (RS-500, Elenco, Wheeling, IL). The high series resistance was used so that applied EFs across the cells could be kept relatively constant despite subtle changes in the channel resistance. Pulsed EFs were increased by a factor of 2 and 4 for the 50% and 25% duty cycles, respectively, to maintain time averaged EFs of 300 mV/mm. More details describing the experimental setup are described in Appendix B.

Velocity Profiles

To directly compare velocity profiles between PDP and EKP we modelled flow between two planes using the planar Poiseiulle equation (Fox and McDonald, 1992) and equation 25 from Soderman and Jonsson (Soderman and Jonsson,1996), respectively. Excel was used to calculate the pressure generated profiles and a MATLAB script was used to calculate the EOF profiles.

RESULTS

Electro-osmotic flow through Matrigel

EOF through crosslinked Matrigel was tracked by monitoring progression of the dye front of neutral Texas Red-linked dextrans. Fig. 12A illustrates the experimental setup used to apply EOF through the Matrigel in the IBIDI channel and image movement of the fluorescent dye front.

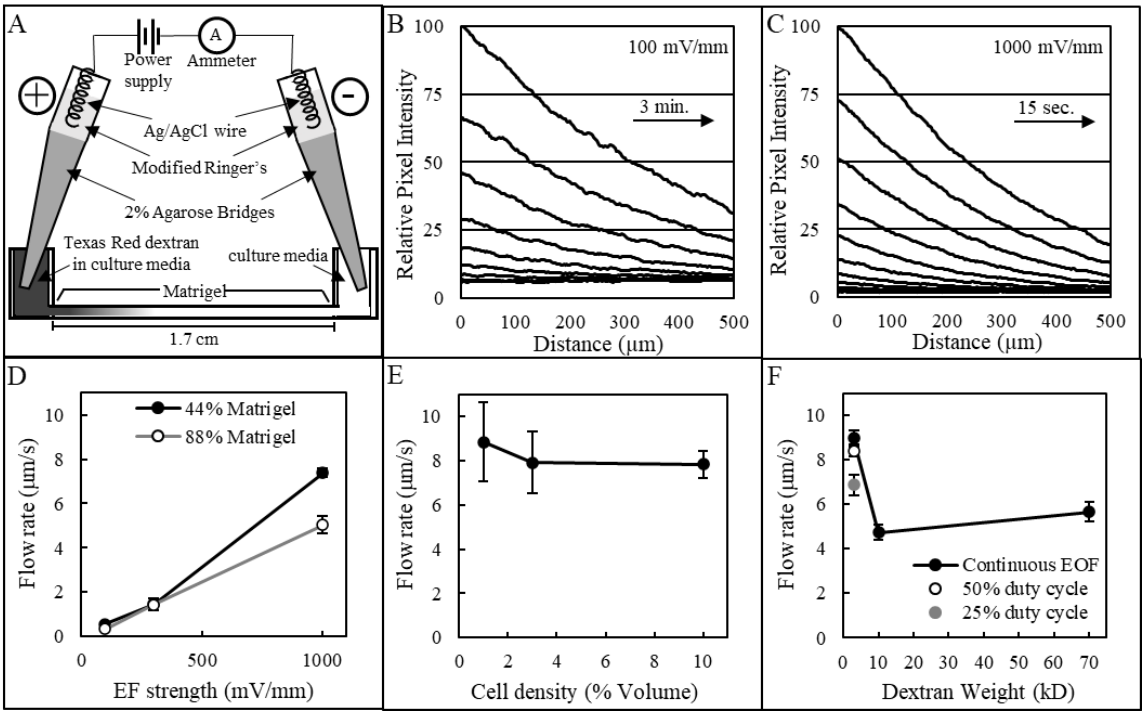

Figure 12. Electro-osmotic flow through Matrigel measured with neutral fluorescent dextrans. A. The experimental setup used to measure electro-osmotic flow through Matrigel filled IBIDI lanes included a power supply connected to the chamber via Ag/AgCl wires and 2% low EEO agarose bridges. Current was monitored and maintained by altering the applied voltage using an ammeter in series. B. The flow profile of 3kDa Texas Red dextran at 100 mV/mm is shown moving from left to right, as shown by the black arrow. Flow profiles are shown at 3 min intervals for better visualization. C. The flow profile of 3kDa Texas Red dextran at 1000 mV/mm is shown moving from left to right, as shown by the black arrow. Flow profiles are shown at 15s intervals. D. EOF is dependent on EF strength and Matrigel density. Texas Red dextran (3 kDa) was used to measure EOF in Matrigel at three different field strengths. 88% Matrigel possesses lower EOF than 44% Matrigel. E. EOF is independent of cell concentration when cell density is ≤ 10% by volume. F. 10kD and 70kD Texas Red dextrans showed slightly lower velocities than EOF measured with the 3kD dextran in 50% Matrigel. Monophasic pulsed EFs with a 50% duty cycle showed similar average flow velocity compared to continuous EFs but flow velocity during pulsed EFs with a 25% duty cycle was lower. Error bars represent S.E.M.

Examples of the profiles of the dye front are shown in Fig. 12B+C during exposure to 100 and 1000 mV/mm, respectively. The average movement of the dye front was determined at the steepest region. The profile lines in 1B and C are reported at 3min and 15s intervals, respectively.

EOF was determined for the most concentrated crosslinked Matrigel, 88%, and half its concentration, 44%, during exposure to EFs of different magnitude, Fig. 12D. The average EOF in 44% Matrigel increased from 0.6 ± 0.1 μm/s at 100 mV/mm, to 1.5 ± 0.3 μm/s at 300mV/mm, to 7.4 ± 0.2 μm/s at 1000 mV/mm. In 88% Matrigel EOF was lower by 24%, on average, i.e. 0.4 ± 0.1, 1.4 ± 0.1, and 5.0 ± 0.4 μm/s, for 100, 300 and 1000 mV/mm, respectively, Fig. 12D.

To determine the influence of cell density on EOF velocity, similar measurements were performed through crosslinked 50% Matrigel loaded with CHO cells. EOF velocity at 1000 mV/mm did not change significantly when Matrigel was loaded with 1%, 3% or 10% cells by volume, Fig. 12E ($p>0.05$ for all 3 comparisons), indicating that EOF is dominated by the charge on the Matrigel macromolecules at these cellular densities.

Movement of larger neutral fluorescent dextrans was tracked to determine how well larger macromolecules could penetrate the crosslinked 50% Matrigel. The average velocity for 10 kD and 70 kD dextrans at 1000 mV/mm was significantly lower, 4.7 ± 0.3 and 5.7 ± 0.4 μm/s, respectively, than EOF for the 3 kD dextran, 8.9 ± 0.4 μm/s, Fig. 12F. We conclude that movement of the larger dextrans was impeded but still maintained relatively high mobility through the Matrigel.

In addition to continuous DC EFs, we measured EOF velocity in response to monophasic, pulsed EFs with 0.5 ms duration. Pulses with a 50% duty cycle showed an average EOF velocity of 8.4 ± 0.3 μm/s that was not significantly different than continuous EOF, Fig. 12F. However, the 25% duty cycle showed slightly lower EOF, 6.9 ± 0.5 μm/s ($p < 0.01$), compared with continuous EOF.

Electromigration of charged solutes

PDP generates unidirectional mass transfer while EKP generates bidirectional transfer. EKP through negatively charged gels generates both electrophoretic and electro-osmotic forces on solutes. Eq. 17 describes the sum of the forces due to electrophoresis of a solute i.e. the product of

solute charge (q) and applied electric field (E), and due to electro-osmosis using Stokes' drag where solute radius (α), fluid viscosity (η), and solute velocity (v) relative to EOF are involved. Diffusion of macromolecules through low density, porous Matrigel and low density collagen gels is similar to diffusion in water,(Kihara et al., 2013; Miura and Tanaka, 2009) therefore a correction for tortuosity is not included.(Faraji et al., 2011)

Eq. 17 $$\sum F = qE + 6\pi\alpha\eta(EOF - v)$$

During equilibrium, the sum of the forces equals zero and the velocity of the charged solute equals zero.

Eq. 18 $$0 = qE + 6\pi\alpha\eta * EOF$$

Rearranging the terms yields the relationship for the relative charge (z) to radius ratio in eq. 19, where z is the absolute charge (q) divided by the unit of charge on an electron (e).

Eq. 19 $$\frac{z}{\alpha} = -\frac{6\pi\eta * EOF}{E * e}$$

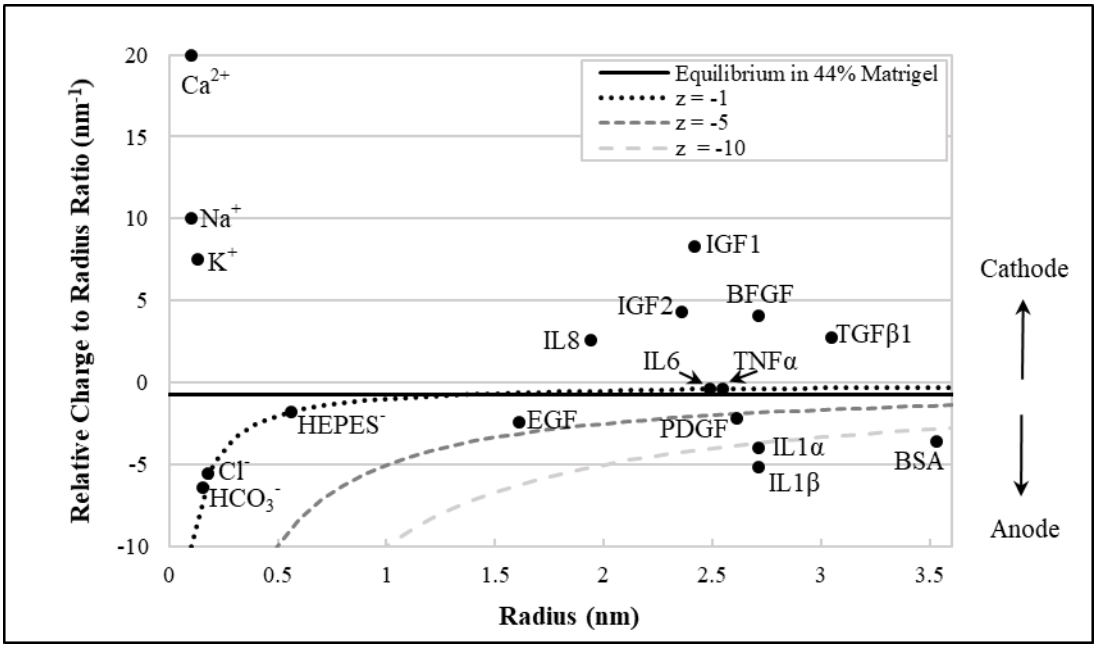

Figure 13. Electromigration of charged solutes is dependent on size and net surface charge. Solutes plotted above equilibrium between electrophoresis and electro-osmosis (solid black line) are predicted to migrate toward the cathode while solutes below the line are predicted to migrate toward the anode. Dotted lines illustrate the change in z/α ratio when the hydrodynamic radius of the solute increases and relative charge (z) remains constant. IGF – insulin-like growth factor, BFGF – basic fibroblast growth factor, TGFβ1 – transforming growth factor, EGF – epidermal growth factor, PDGF – platelet derived growth factor, IL1, IL6, IL8 – Interleukins 1, 6 & 8, TNFα - Tumor Necrosis Factor, BSA – bovine serum albumin, $HEPES^-$ - anionic form of H^+ buffer, Ca^{2+}, Na^+, K^+, Cl^- HCO_3^-- inorganic ions.

Eq. 19 describes equilibrium between electrophoresis and electro-osmosis and is useful for predicting the direction of electromigration for specific solutes. Solutes with a z/α ratio greater than equilibrium will migrate toward the cathode while solutes with a z/α ratio less than equilibrium will migrate toward the anode. The z/α ratios of representative solutes, i.e. inorganic ions, growth factors and cytokines, are plotted in Fig. 13. Surface charge of proteins was determined using relative solvent accessibility of charged residues (Sarkar et al., 2019) and size was approximated using the Hydrodynamic Radius Converter (Fluidic Analytics Ltd, Cambridge, UK) assuming proteins were in a globular conformation.

Equilibrium between the forces of electrophoresis and electro-osmosis in 44% Matrigel is indicated by the solid black line, Fig. 13. A higher negative charge density of the extracellular matrix will make equilibrium more negative. Solutes with neutral or net positive charge will migrate toward the cathode, Fig. 13. Negatively charged solutes with a z/α ratio less negative than equilibrium will also migrate toward the cathode, e.g. cytokines IL-6 and TNFα. However, negatively charged solutes with a z/α ratio more negative than equilibrium will migrate toward the anode, e.g. Cl^-, epidermal growth factor (EGF), pro-inflammatory cytokines IL-1α & 1β. These results indicate that EOF will dominate migration of neutral and positively charged solutes toward the cathode under physiological conditions. However, electrophoresis will dominate electromigration of negatively charged solutes toward the anode. As a result, media at both ends of the 3D culture must be replaced during EKP to maintain solute homogeneity.

Electrokinetic perfusion decreases cell mortality in 3D culture

We compared cell mortality between 3D cultures exposed to no perfusion, PDP and EKP. Cells were cultured in crosslinked Matrigel loaded into IBIDI channel slides, illustrated in Fig. 14A. PDP at 300 and 60 μL/day generated flow rates of 2.3 and 0.5 μm/s, respectively, Fig. 14B, while EKP using EFs of 300 mV/mm and 60 mV/mm generated EOF of 1.5 ± 0.4 and 0.4 ± 0.4

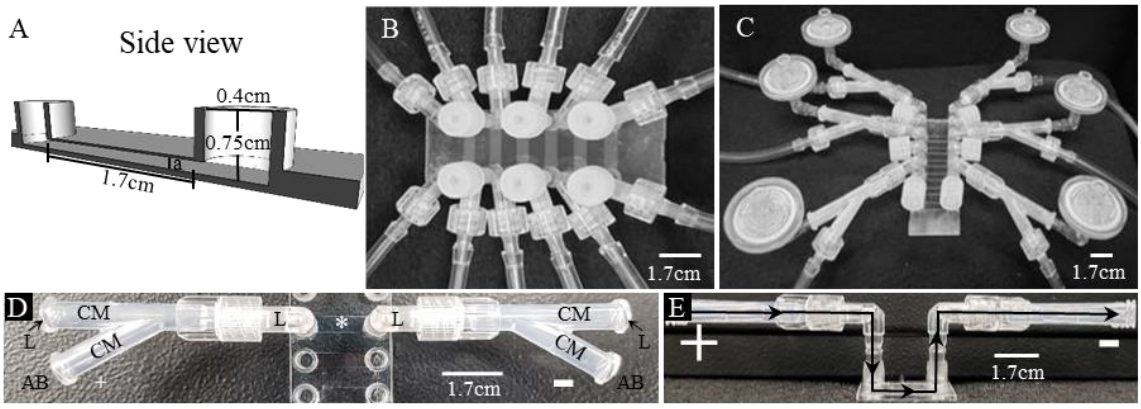

Figure 14. IBIDI chambers were used to induce interstitial flow through 3D cultures in Matrigel. A. Illustration of a single IBIDI channel with dimensions of 0.04 cm deep (a), 0.38 cm wide (b) and 1.7 cm long. B. Top view of PDP slide. PDP was generated through the channels by programmed compression of syringes connected to the channels using T-connectors and silicone tubing. Channels were drained using similar connectors and tubing. C. Top view of EKP slide. EKP was applied to the channels using power supplies and Ag/AgCl electrodes connected to the channels by low EEO agarose bridges. Microbe removing filters (0.2 μm) were connected to the ends of culture media containing connectors to allow gas exchange and maintain aseptic conditions. D. Top view of partial EKP channel. Culture media (CM) is present in the L-connectors (L) and both branches of the Y-connector. Low EEO agarose bridges (AB) are connected to the angled branch. The asterisk marks the channel containing cells and Matrigel, and the plus and minus symbols indicate electrical polarity. E. Side view of a magnified EKP channel. Black arrows show direction of fluid movement induced by an applied EF. Net fluid movement in the straight branches did not change height, preventing formation of pressure gradients.

μm/s, respectively, Fig. 14C. The arrangement of connectors shown in Fig. 14D+E prevented a change of net fluid height and buildup of back pressure. The 300 mV/mm field strength across the Matrigel filled channel was generated using an applied voltage difference of 5.1 V and 0.7 mA, equivalent to only 3.6 mJ/s. We conclude that the temperature of the chamber was dominated by its surroundings and not the low amount of current through the gel. Neither PDP nor EKP directed mass cell migration in Matrigel, consistent with earlier reports using higher rates of pressure driven interstitial flow (Ng and Swartz, 2003; Ng and Swartz, 2006).

Cell mortality was assessed within 1.5 mm of both ends of the 17 mm long channel and in a region near the center. Mortality was assessed immediately after Matrigel crosslinking was completed (0 hr.) and used as the baseline to determine changes to cell mortality in other channels, 48 hours later, Fig. 15. Average mortality associated with cell handling (Grilo and Mantalaris, 2019) accounted for cells covering 5.4 ± 0.5 % of the sampled regions (Fig. 16, black). After 48

hours in the CO_2 incubator (Fig. 16, gray) or on a 37° C heating block (Fig. 16, white), PI-stained cells increased on average to 26.8 ± 1.7% and 24.0 ± 2%, respectively.

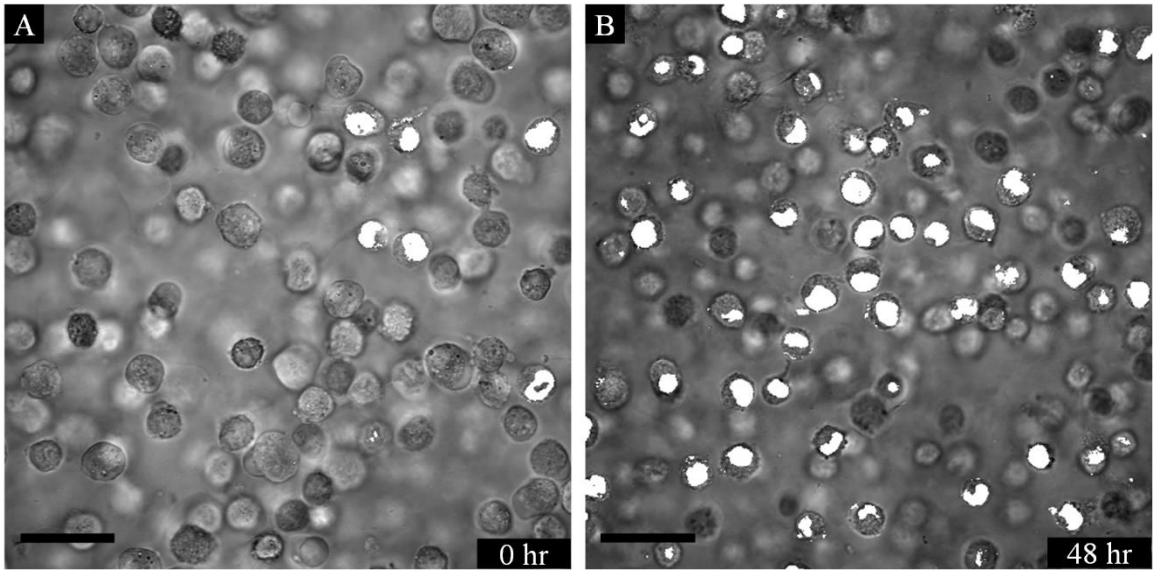

Figure 15. Propidium iodide stain of control cells in Matrigel filled channels. Images display overlays of PI fluorescence (pseudo-colored white) on the transmitted light images. A. After Matrigel crosslinking (0 hr.) a small fraction of cells show membrane disruption that allows PI staining. B. After 48 hr. in the absence of flow a significantly higher density of cells shows PI staining. Scale bar – 60 µm.

Two perfusion rates for PDP and EKP were performed in the presence and absence of serum containing growth factors, Fig. 17. Relative mortality was assessed as the ratio of PI-stained cells of the perfused channels to the same regions of the nonperfused, control channels and compared using one-tailed t-tests, Fig. 17. The dotted line highlights normalized mortality in the absence of perfusion. PDP of serum containing DMEM at the high rate (2.3 µm/s) was the only perfusion experiment that showed differences in mortality between the 3 regions of the chamber. Mortality was significantly

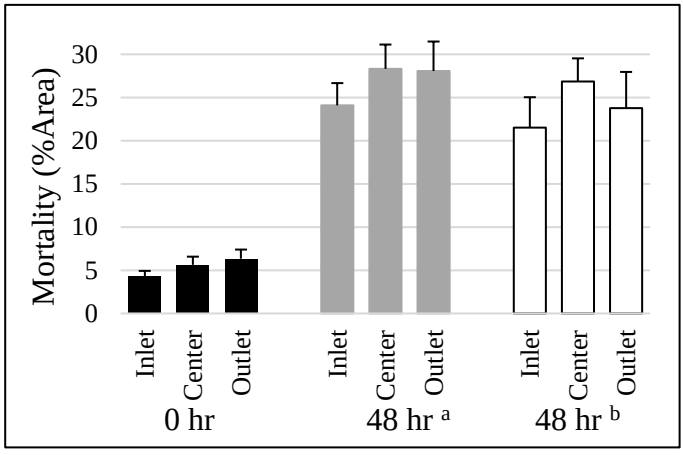

Figure 16. Cell mortality in 3D culture in the absence of interstitial flow. Propidium iodide staining was used to assess cell viability immediately after 3D culture of CHO cells and 48 hours later. [a]cultured in CO_2 incubator. [b]cultured on 37° C heating block and sealed from the atmosphere. Inlet and outlet for the nonperfused channels refer to the direction of perfusion during removal of transglutaminase and loading of PI.

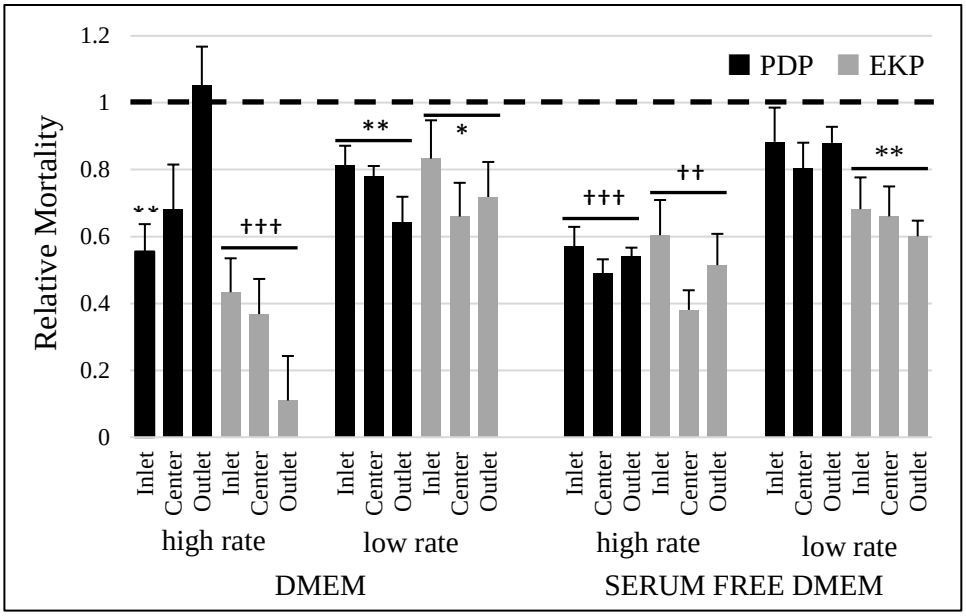

Figure 17. Perfusion most commonly reduces cell mortality in 3D culture. Relative mortality for PDP (black) and EKP (gray) were collected after 48 hr. at two different flow rates in DMEM culture media in the presence and absence of 10% serum containing growth factors. Symbols indicate p-values for the comparison between perfused conditions and nonperfused controls. * $p < 0.05$, ** $p < 0.005$, †† $p < 0.001$, ††† $p < 0.0001$.

reduced at the inlet ($p < 0.005$) that was supported by agarose, but not at the center ($p > 0.1$) or outlet ($p > 0.4$) of the channel, Fig. 17. As none of the other experiments showed statistically different mortality between the 3 regions of the chambers, the results from the three regions were combined before further analysis.

In the absence of serum, the high rate of PDP significantly reduced mortality to 0.53 ± 0.02. Under similar conditions the higher EKP (300 mV/mm) significantly reduced mortality to 0.3 ± 0.1 and 0.50 ± 0.04 using serum-containing DMEM and serum-free DMEM, respectively. This difference in mortality supports the fact that common CHO cells are dependent on growth factors (Pak et al., 1996; Rasmussen et al., 1998). Reduced mortality between PDP and EKP at the high rates in the absence of serum is not different ($p > 0.5$, two-tailed t-test).

At the lower rate of PDP (0.5 μm/s), mortality was reduced significantly to 0.74 ± 0.03 ($p < 0.005$) in the presence of serum but was not significantly reduced compared to controls in the absence of serum ($p > 0.05$). In contrast, cell mortality at the lower EKP (60 mV/mm) reduced

mortality to 0.74 ± 0.09 ($p < 0.05$) in the presence of serum and to 0.65 ± 0.06 ($p < 0.005$) in the absence of serum and are not statistically different from each other ($p > 0.4$, two tailed t-test).

To test whether the increase in cell mortality was due to starvation-induced autophagy we replaced the high basal glucose level in the serum-free DMEM (25 mM) with lower glucose (5 mM). Relative mortality in serum-free high glucose conditions was not significantly different for PDP ($p > 0.05$) or EKP ($p > 0.7$) when compared with lower glucose levels (two-tailed t-test for both). Mortality for PDP and EKP in serum-free DMEM are displayed for comparison, Fig. 18. We conclude that depletion of glucose in the dense 3D cell culture was not increasing mortality through starvation-induced autophagy.

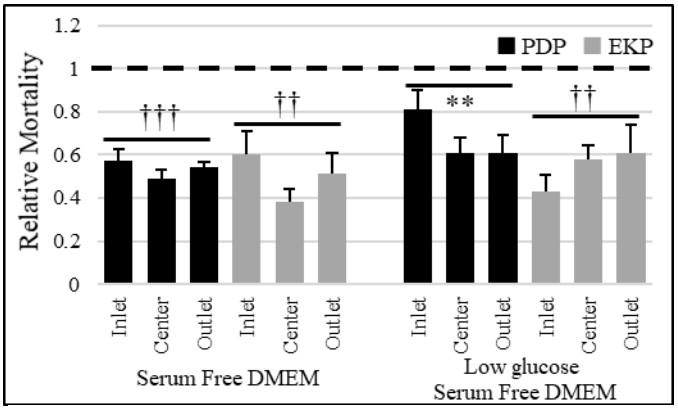

Figure 18. Lowered glucose does not significantly change viability in serum-free DMEM. Glucose reduction from 25mM to 5mM did not increase cell death in these 3D cultures. Symbols indicate p-values for the comparison between perfused conditions and nonperfused controls. ** $p < 0.005$, †† $p < 0.001$, ††† $p < 0.0001$.

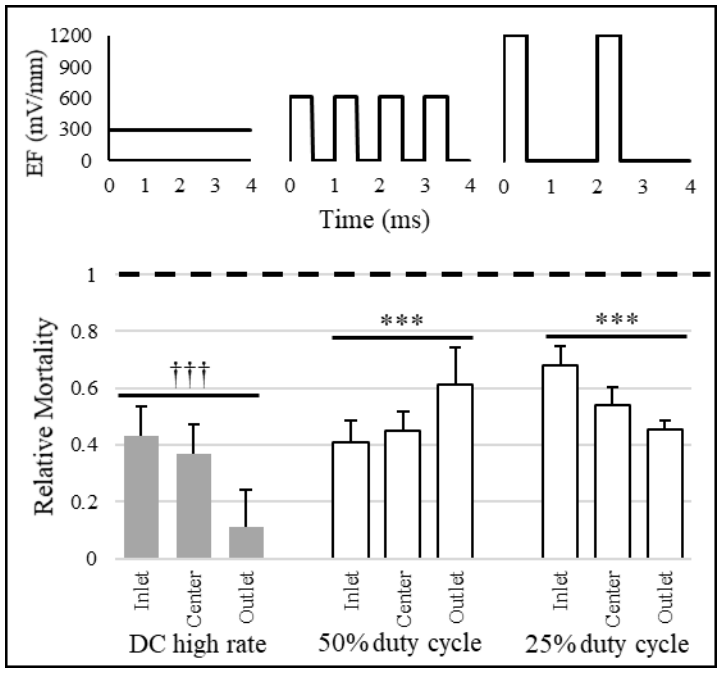

Figure 19. Time averaged EKP reduces mortality. Time averaged electric fields were maintained at 300 mV/mm for DC, and pulsed waveforms with 50% and 25% duty cycles. Waveform profiles are displayed above their relative mortality results. Reduction of mortality between DC and pulsed waveforms is not significantly different ($p > 0.5$ for both comparisons). Symbols indicate p-values for the comparison between perfused conditions and nonperfused controls. *** $p < 0.0005$, ††† $p < 0.0001$.

Repeated electrical pulses of short duration are applied for long periods of time to promote healing of nonexcitable soft tissues (Gardner et al., 1999; Kloth, 2014; Messerli and Graham, 2011). We

hypothesize that these intermittent EFs would generate a time averaged EKP to reduce mortality. Cell mortality from continuous EFs at 300 mV/mm was compared to intermittent EFs with 50% and 25% duty cycles using a 0.5 ms pulse duration. The electrical waveforms associated with each condition are illustrated at the top of Fig. 19. The time averaged field strength was kept constant between the DC high rate and pulsed waveforms. The 50% and 25% duty cycles significantly reduced mortality on average to 0.49 ± 0.07 and 0.56 ± 0.05, respectively, and are not significantly different from the high rate, continuous EKP, $p > 0.9$ and $p > 0.5$, respectively.

DISCUSSION

We report that electrokinetic perfusion through porous tissue promotes mass transfer, Fig. 12, and reduces cell mortality with significant advantages over pressure driven perfusion, Fig. 17. We hypothesize that perfusion reduced apoptosis of CHO cells by preventing hypoxia and stabilizing the culture pH (Grilo and Mantalaris, 2019). However, the high rate of PDP with serum significantly reduced mortality only on the inlet side of the chamber, while the high rate of EKP with serum reduced mortality to a significantly greater extent throughout the channel, Fig. 17. At the lower perfusion rate in the presence of serum or at the higher perfusion rate in the absence of serum, PDP and EKP showed similar reduction of mortality in these low-density matrices, Fig. 17. We conclude that the combination of greater flow velocity and serum proteins inhibited PDP from reducing mortality throughout the channel. PDP through porous materials favors the wider pathways through Matrigel, Fig. 20. However, through isotropic charged gels, EKP generates more uniform EOF over a larger range of pathway width,(Soderman and Jonsson, 1996) Fig. 20.

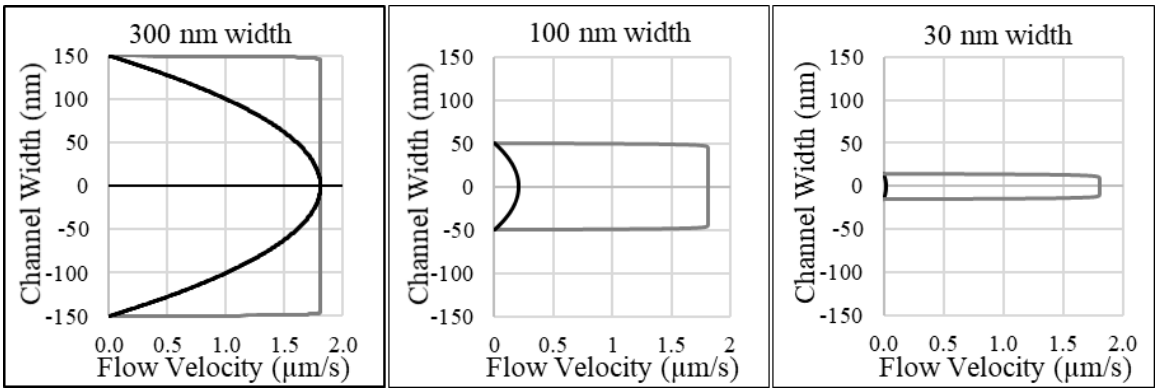

Figure 20. Modelled comparison of pressure driven flow and electro-osmotic flow through narrow planar channels. An applied pressure gradient of 1.2 mmHg/mm generates a parabolic flow profile (black) with peak flow of 1.8 µm/s in the 300 nm channel, that decreases with distance between the two planes according to plane Poiseuille flow, i.e. 0.2 and 0.02 µm/s for 100 and 30 nm distances. An applied EF of only 100 mV/mm through a channel with a -10 mV zeta potential, generates a plug profile (gray) in physiological saline with peak flow of 1.8 µm/s for a range in distance between the walls (Soderman and Jonsson, 1996).

We hypothesize that the larger pathways favored by PDP, became blocked with the larger hydrophobic serum proteins. Matrigel pores range from 6 nm to ≤ 1 µm for 100-50% Matrigel (McCarty and Johnson, 2007; McCarty et al., 2008; Zaman et al., 2006). Low density lipoprotein (~22nm diameter) is known to aggregate within Matrigel and reduce hydraulic conductivity

(McCarty et al., 2008). Other hydrophobic proteins may have the same effect. For example, serum albumin (triangular configuration with 8 nm edges (Leggio et al., 2008)) is the most abundant protein in plasma and serum, and is normally absent from interstitial fluid between cells. Albumin is known to be 'sticky', adhering to both hydrophobic and charged moieties including collagen and albumin itself (Dorh et al., 2015; Krajewski et al., 1996; Meltzer and Silberberg, 1988). Even though the flow pathways could become blocked with these proteins during EKP, i.e. anodal migration of BSA (Fig. 13), we hypothesize that the narrower pathways continued to allow sufficient perfusion to reduce mortality. In addition, we hypothesize that while PDP is known to cause compaction at the inlet side, it also may have caused increased stretch toward the outlet side due to an increase in blocked pathways. This effect would increase deformation of the gel and subject the cells to greater strain induced damage. Therefore porous supports may be required at both the inlet and outlet sides during PDP (Ng and Swartz, 2003). These constraints make it very challenging to apply PDP through tissues *in vivo*. However, careful placement of electrodes *in vivo* promotes EKP through even dense brain tissue (Rupert et al., 2013b). Additional experiments will be needed to test the efficacy of EKP *in vivo* where extracellular matrix density and net negative charge vary.

We hypothesize that electrical therapies with a time-averaged DC component,(Frykberg and Banks, 2015; Gardner et al., 1999; Isseroff and Dahle, 2012; Kloth, 2014; Messerli and Graham, 2011) may promote interstitial flow to promote healing and recovery of soft tissues. We tested whether short duration, monophasic pulses, commonly used during these electrical therapies, were sufficient to reduce mortality. Both pulsed waveforms, significantly reduced mortality and were not different than 300 mV/mm DC EF, consistent with a time averaged EKP. This hypothesis might be questioned for electrical therapies when electrodes are placed on top of high resistance skin. However, it is dry skin that has high electrical resistance while resistance across wet skin is an order of magnitude lower (Tagami et al., 1980). Moreover, the resistance of electrically stimulated skin decreases by 2-3 orders of magnitude within milliseconds of stimulation

(Chizmadzhev et al., 1998; Denet et al., 2004). Therefore, monophasic electrical pulses, commonly applied to heal chronic epidermal wounds or promote healing of skin grafts, (Gomes et al., 2018; Politis et al., 1989) lower the electrical resistance of skin and may generate time averaged interstitial flow through tissues.

EKP rescued cell viability in an EF dependent manner but we did not explore the upper limit of this phenomenon due to limitations with the current system. Addition of blood vessels has supported construction and transplantation of 2 dimensional cardiac patches ≥ 1 mm thick (Noor et al., 2019; Su et al., 2020). However, in the absence of blood flow, diffusion limits tissue construction to about 0.2-0.4 mm diameter (Lovett et al., 2009; Novosel et al., 2011). We show that EKP reduced cell mortality over a distance 50 times greater and its limit has not yet been reached. We hypothesize that nutrients will be depleted in longer channels before they reach the opposite end of the chamber and that higher flow rates may extend this above-mentioned limit. We hypothesize that EOF could be increased 10-fold greater than used in these studies. An upper limit for artificial interstitial flow appears to be ~13 μm/s, when pressure driven flow began to increase cell rounding and death of fibroblasts in 3D cultures (Ng and Swartz, 2003; Ng and Swartz, 2006). With respect to the upper limit for applied EFs, increased mortality of electrically excitable cells was identified in brain slices exposed to DC EFs ≥ 2800 mV/mm for 5 min., while lower voltages did not increase mortality (Hamsher et al., 2010; Rupert et al., 2013a). This indicates that the DC EKP may be increased by nearly 10-fold before voltage-dependent mortality is expected. Greater charge density of native extracellular matrices will enable higher EKP at lower applied EFs.

Intermittent EKP requires further investigation near excitable and nonexcitable cells. Brief, monophasic pulses require much greater amplitude to charge membrane capacitance and depolarize cell membranes. While this varies with cells and their plasma membrane time constant, our results indicate that EKP can be induced at a higher frequency that is below sensory threshold for excitable cells (Tung et al., 1991). Therefore, EKP may be useful for sustaining viability during construction of electrically excitable tissues as well as nonexcitable tissues.

CONCLUSION

We conclude that electrokinetic perfusion through negatively charged extracellular matrices promotes interstitial flow and reduces cell mortality by preventing apoptosis. This form of perfusion has significant advantages over pressure driven perfusion especially in the narrow spaces that exist between cells *in vivo* and in 3D tissue culture. In the absence of sufficient flow through blood or lymphatic vessels, electrical therapies may stimulate healing of soft tissues by promoting interstitial flow.

APPENDIX A

1.a. Methods for Time Course of Keratocyte Galvanotaxis

Galvanotaxis of zebrafish keratocytes was performed in accordance with IACUC protocol #15-022A. Adult zebrafish were anesthetized in 0.4% Tricaine methanesulphonate, and scales were plucked, cultured with the superficial side facing up and incubated in L15 media with 20% FBS and 1% Pen-Strep at 28°C. Overnight, sheets of cells migrated off the scale. The next day, cells were rinsed with Ca^{2+}-free Fish Ringer's (FR) before incubating in Ca^{2+}-free FR for 8 minutes, to separate cells and loosen overlying mucus. Brief pulses of Ca^{2+}-free FR were used to remove the mucus and weakly attached cells. Additional treatment with 0.025% Trypsin-EDTA enhanced cell separation. Cells were rinsed three times with glucose-free FR, before adding a final volume of glucose containing FR. Cells were incubated for an additional 15 minutes at 28°C to allow cells to recover and spread out before experimentation.

An image of the migrating keratocytes was acquired each minute using a Zeiss Axiovert S100TV inverted microscope. EF application of 125 mV/mm was applied between the two ends of the chamber using a Lambda power supply (Lambda Electronics Inc., Melville, N.Y), and coiled Ag/AgCl electrodes immersed in FR containing agarose bridges. An ammeter was connected in series to monitor the current density in the chamber and the current was adjusted to maintain a relatively constant EF during the course of the experiments. Timelapse images were acquired every minute at ambient temperature, 21°C. Migration was captured in the absence of applied EFs for the first 5 min. and was followed for 60 min. of migration in an applied EF of 125 mV/mm.

ImageJ analysis software (Rasband, 1997-2018) was used to track migration of single cells that did not contact other cells or debris and remained in the field of view during the length of the experiment. Directed migration for the population of cells was determined using the average cosine θ (Kobylkevich et al., 2018), and was calculated between single frames in order to identify the time

course of cathodal migration. The average cosine θ ± S.E. is plotted for 5 dishes, including 111 cells.

1.b. Results of Keratocyte Galvanotaxis

In order to assess the time course for electromigration of zebrafish keratocytes we performed timelapse imaging of the turning of zebrafish keratocytes and analyzed directionality on a minute by minute basis. Fig. 10 shows the average response for 111 cells from 5 different dishes in EF of 125 mV/mm. A steady state is reached for the population with a 90% response time of 20 min.

2. Plasma Membrane Protein Identification

Surface exposed proteins of zebrafish keratocytes and estimates of their physical properties were obtained using the zebrafish proteome downloaded from the National Center for Biotechnology Information (NCBI), 'GCF_000002035.5_GRCz10_protein'. Multiple programs and database manipulations were performed and are shown in a flow chart in Fig. 21. Plasma membrane surface proteins were organized into three categories including transmembrane, integral, and GPI-anchored. Transmembrane (TM) proteins were identified using Consensus prediction of membrane Topology and peptides (TOPCONS) (Tsirigos et al., 2015). Twenty-seven peptide sequences were not accepted by

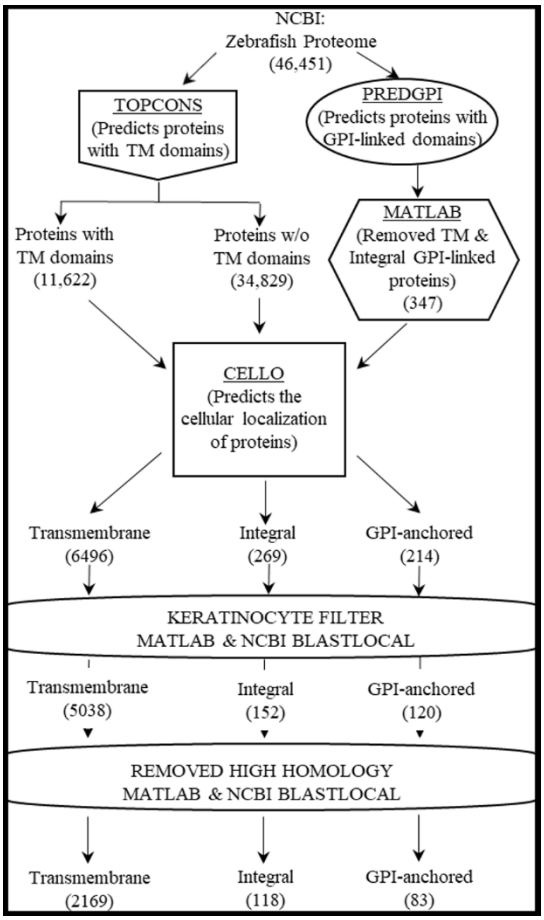

Figure 21. Flow diagram for identification of nonredundant plasma membrane surface proteins from zebrafish epidermal keratocytes.

TOPCONS due to their extreme length >10,000 amino acids. These proteins were later identified as cytoplasmic titin and eleven of its isoforms, eleven uncharacterized proteins and their isoforms, and four sequences of cytoplasmic nesprin-1 and its isoforms. TOPCONS uses sequence alignment to separate transmembrane proteins from globular proteins and signal peptides based on local composition of hydrophobic amino acids. A MATLAB script was used to sort the sequences into two datasets, with and without transmembrane domains, with the help of the topology files generated by TOPCONS for each protein sequence.

Cellular localization of the transmembrane proteins was performed using the online, Subcellular Localization Predictor, CELLO, version 2.5 (Yu et al., 2006). CELLO predicts location of proteins to 12 different subcellular regions by assessing amino acid composition and position based on their physicochemical properties and similarity to proteins from two benchmark datasets of protein sequences, one from prokaryotes and the other from eukaryotes. Short lists of zebrafish transmembrane proteins were submitted to CELLO to accommodate its input limit. These protein sequences with the highest probability of plasma membrane localization, were identified by CELLO, extracted from CELLO output lists using a MATLAB script, and designated as transmembrane proteins.

Protein sequences without transmembrane domains, originally identified by TOPCONS, were also submitted to CELLO, to identify their subcellular localization. Many of these proteins were identified as plasma membrane-bound and extracellular. These proteins were extracted from the CELLO output lists using a MATLAB script and designated as external, integral membrane proteins.

GPI-anchored proteins were identified using Predictor GPI (PredGPI) (Pierleoni et al., 2008), a program that determines the localization of the glycosylphosphatidylinositol anchor at the c-terminus of queried proteins based on a consensus sequence of the cleavage site, known as the ω-site. Predictions labelled as ‘highly probable’ (specificity: 99.9-100%) and ‘probable’ (specificity: 99.5-99.8%) were used to identify GPI-anchored proteins. These GPI-anchored

sequences were compared with the two other groups of proteins, to remove duplicates between the lists. Transmembrane proteins and integral membrane proteins with GPI anchors remained in their original categories and were removed from the GPI-anchored protein list. The remaining GPI-anchored proteins were screened using CELLO, to identify proteins that were localized to the extracellular region of cells. Proteins with the highest prediction scores were identified by CELLO, extracted from the CELLO output lists using a MATLAB script and were designated as extracellular, GPI-anchored proteins.

At this stage of the screen, the three data sets include predicted plasma membrane surface proteins from all cells in the zebrafish. In order to restrict the protein population to epidermal keratocytes we compared the three datasets to a human keratinocyte transcriptome (Reemann et al., 2014) and kept proteins with high homology. Human keratinocyte transcripts, with a Reads Per Kilobase of transcript, per Million mapped reads (RPKM) value ≥1, were used to perform the comparison, resulting in 8937/22582 total human sequences (Hebenstreit et al., 2011; Wagner et al., 2013). Protein sequences for the keratinocyte transcripts were obtained using Biomart-Ensemble (https://www.ensembl.org/biomart) and compared to the zebrafish protein sequences using NCBI's "Blastlocal", nested within a MATLAB script. The e-score threshold was set at 10^{-4} to avoid loss of diverging sequences. After screening, 5310 zebrafish sequences remained.

One final reduction in list size involved removal of homologous protein sequences, so that fewer representative proteins remained. Proteins within each of the three datasets were compared to each other and proteins with an e-score of $\leq 10^{-100}$ and percent identity above 80 were removed.

Physical properties of proteins in the three groups were determined, including molecular weight (total, intracellular and extracellular), estimated molecular weight with glycosylation, number of transmembrane domains, and extracellular net charge based on amino acid composition and pKas of amino acids. We used MATLAB scripts and topology files from TOPCONS to determine the amino acids in the extracellular domains of the transmembrane proteins, and then summed the molecular weights of those amino acids. The net charge of each of the amino acids

was determined at pH 7 and summed to obtain a prediction of the extracellular net charge, and then rounded to the closest integer. For integral membrane proteins and GPI-linked proteins, we used the entire length of the protein for calculating size and net charge.

Glycosylation of proteins can have significant impact on both size and charge of proteins. N-linked and O-linked glycosylation sites were identified using different methods. N-linked glycosylation sites were determined by identifying the established signal motif (Zielinska et al., 2010) in the protein sequences using a MATLAB script. O-linked sites were determined for the three groups of proteins by submitting sequences to both NetOGlyc version 4.0.0.13 server (Steentoft et al., 2013), and OGTSite version 1.0 (Kao et al., 2015), to determine their O-linked glycosylation sites rich in N-acetylgalactosamine and N-acetylglucosamine, respectively. O-linked sites were compared using a MATLAB script to remove duplications in glycosylation sites as predicted by the two different algorithms.

Physical properties of the sugars were based on estimates of the average molecular weights and net charge for the different sugars. The average molecular weight of N-linked oligosaccharides was estimated to be 2.5 kD and O-linked oligosaccharides was estimated to be 1.2 kD (An and Lebrilla, 2011; Imperiali and O'Connor, 1999). Both N-linked and O-linked sugars may contain a variable amount of terminal sialic acid residues. The impact of charge on the proteins due to glycosylation was estimated by considering, on average, 3 sialic acids on each N-linked oligosaccharide and on average, 1 sialic acid molecule on each O-linked oligosaccharide (An and Lebrilla, 2011).

Table 4. Summary Table of Variables and Constants for Equations 7-16.

Symbol	Definition	SI Units
C	Concentration of a macromolecule at a specific position and time	$mols/m^3$
ΔC	Concentration gradient at a specific position and time	$mols/m^3$
$\in_r$	Dielectric constant or relative permittivity (in saline)	n.a.
D	Diffusion coefficient of macromolecule in plasma membrane	m^2/s
Δx	Distance between two discrete points	m
E	Electric Field; electric force experienced by a charge	V/m
$\in_0$	Electric permittivity of free space	F/m
EOF	Electro-osmotic flow; velocity of a fluid near a charged surface, induced by an applied electric field	m/s
μ_{eo}	Electro-osmotic mobility; velocity of a macromolecule generated by electrically induced water flow	m/s/V/m
μ_{ep}	Electrophoretic mobility; velocity of a charged macromolecule by a local electric field	m/s/V/m
F	Faraday's constant	C/mol
F_1, F_2, F_3	Forces acting on external domain (1), transmembrane domain (2) and the cytosolic domain (3) of a macromolecule	N
J	Flux; net flow rate of a surface macromolecule per unit area	$mols/m^2s$
R	Ideal gas constant	J/mol●K
α_1, α_2, α_3	Radii (equivalent) of the external domain (1), transmembrane domain (2) and the cytosolic domain (3) of a macromolecule	m
T	Temperature	K
v_1, v_2, v_3	Velocities of the external domain (1), transmembrane domain (2) and the cytosolic domain (3) of a macromolecule	m/s
η_1, η_2, η_3	Viscosities of the extracellular fluid (1), plasma membrane (2) and the cytosolic fluid (3)	Pa●s
z	Extracellular surface exposed charge of the macromolecule	n.a.
ζ	Zeta potential; surface charge of the cell due to the combined exposed charges of surface macromolecules	V

APPENDIX B

1. Experimental setup for electro-osmotic flow measurements

EOF through Matrigel was measured by casting Matrigel mixed with transglutaminase into IBIDI lanes. Texas Red dextrans, 3 or 10 or 70 kDa, mixed with culture media was added to the anode well at a final concentration of 20 μM while the other well was filled with an equal volume of culture media. Ag/AgCl electrodes were immersed in modified Ringer's (MR) and connected to the IBIDI wells with 2% low EEO agarose bridges (Fisher Scientific, Waltham, MA) containing MR. The electrodes were connected to a power supply and the average current density was maintained by monitoring current with an ammeter in series and adjusting the applied voltage. Time-lapse images of the dye front were recorded at 4, 2 and 1 frame(s)/min for EFs of 1000, 300 and 100 mV/mm, respectively, until the dye had travelled ~750 μm. Images were also collected between EOF experiments in the absence of EFs to track EOF independent migration.

2. Experimental setup for 3D viability assays

CHO cells were cultured in crosslinked Matrigel by allowing cells to settle to the bottom of a sterile tube in MR before collecting a volume of the concentrated cells and mixing with

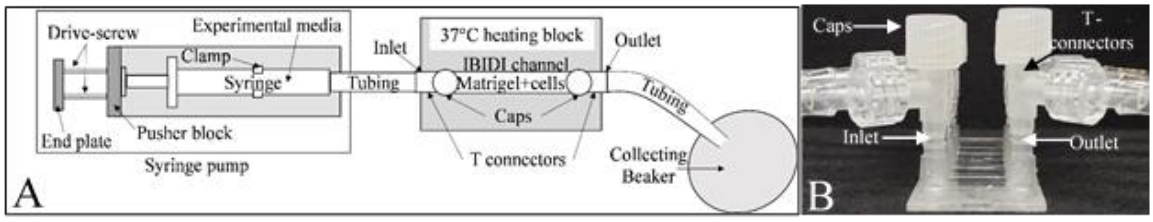

Figure 22. Experimental setup of perfused lanes for PDP. A. Illustration shows the top view of an IBIDI channel fitted to a programmable syringe pump to deliver PDP. B. Side view of a magnified PDP channel. T-connectors on both sides are sealed with caps after filling them with experimental media.

Matrigel stock to make their final volumes in the mixture as 40% and 50%, respectively. Microbial transglutaminase was added to make up the final 10% volume of the mixture. This mixture was then loaded into IBIDI channel slides and allowed to gel as described previously. PDP was applied using syringe pumps connected to IBIDI slides with T-connectors or L-connectors and silicone

tubing, Fig. 22A. A protective 1% agarose gel was added to the inlet well of both perfused and control lanes to prevent the gel from being dislodged from the IBIDI lane during application of fluid pressure. T or L-connectors were added to the inlet side of the lanes after the agarose had gelled. Syringe pumps were fitted with 3mL syringes filled with CO_2-equilibrated sterile culture media. T-shaped connectors, Fig. 22B, were fitted on both wells of the perfused lanes and L-shaped connectors were fitted to the control lanes. After the T-shaped connectors were joined to the syringe by tubing they were filled with media and capped. The L-shaped connectors were filled and fitted to the control syringes. IBIDI channel outlets were drained into a collecting beaker via tubing, Fig. 22A. Cells and IBIDI chambers were maintained at 37°C using a temperature-controlled heating block. The 37°C heating block was used during PDP to protect the syringe pumps from the heat and humidity of the CO_2 incubator while keeping the silicone tubes short.

EKP was generated using power supplies connected to IBIDI channels using Y-connectors in-line with L-connectors, Fig. 23. The straight branch of the Y-Connectors supplied culture media. Air exchange occurred through 0.2 µm syringe filters to maintain aseptic conditions. EFs were

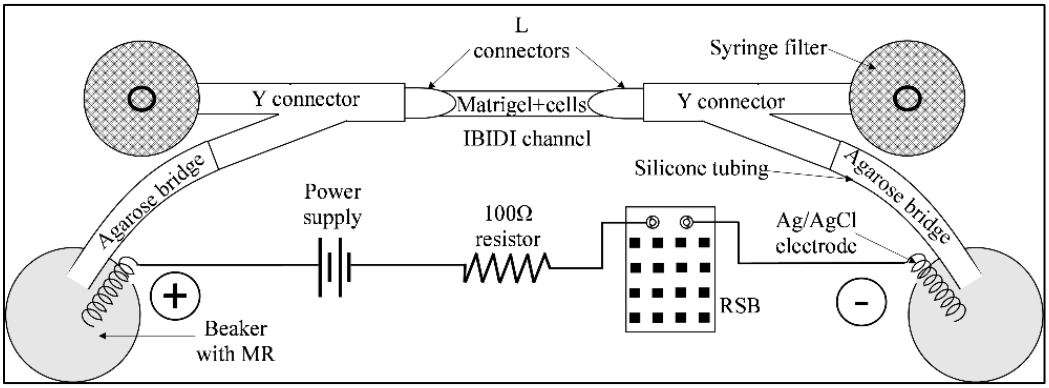

Figure 23. Top view of the experimental setup for an EKP channel. RSB: Resistance Substitution Box. MR: Modified Ringer's

applied through 2% low EEO agarose bridges connected to the angled branch of the Y-adapter, Fig. 23. This arrangement of connectors prevented a change of net fluid height and buildup of back pressure. The low EEO agarose bridges in culture media were formed in silicone tubing (9 cm long) that joined the Y-connectors to the power supplies through Ag/AgCl electrodes immersed in

MR contained in small beakers. Electrodes were connected to power supplies using a resistance substitution box in series for each circuit. The EF across the circuit was maintained by repeatedly checking the voltage drop across a known 100-ohm resistor connected in series between the power supply and the resistance substitution box. In the absence of EFs, channels were sealed on both ends with ~650 µL of media in wells and L-connectors, i.e. greater than 21 times the volume of the cell loaded channel, on both sides. Chambers were kept in a 37ºC CO_2 incubator for the duration of the experiment and media was replaced on each side of the perfused channels and in the Ag/AgCl electrode baths every 12 hours.

LITERATURE CITED

Allen, G. M., Mogilner, A., Theriot, J. A., 2013. Electrophoresis of cellular membrane components creates the directional cue guiding keratocyte galvanotaxis. Current Biology 23, 560-568.

Almen, M. S., Nordstrom, K. J. V., Fredriksson, R., Schioth, H. B., 2009. Mapping the human membrane proteome: a majority of the human membrane proteins can be classified according to function and evolutionary origin. BMC Biology 7, doi:10.1186/1741-7007-7-50.

Amsden, B., 1998. Solute diffusion within hydrogels. Mechanisms and Models. Macromolecules 31, 8382-8395.

An, H. J., Lebrilla, C. B., 2011. Structure elucidation of native N-and O-linked glycans by tandem mass spectrometry (tutorial). Mass spectrometry reviews 30, 560-578.

Barker, A. T., Jaffe, L. F., Vanable, J. W. J., 1982. The glabrous epidermis of cavies contains a powerful battery. American Journal of Physiology Regulatory Integrative and Comparative Physiology 242, 358-366.

Bezanilla, F., 2000. The voltage sensor in voltage-dependent ion channels. Physiological Reviews 80, 555-592.

Bicknese, S., Periasamy, N., Shohet, S. B., Verkman, A. S., 1993. Cytoplasmic viscosity near the cell plasma membrane: Measurement by evanescent field frequency-domain microfluorimetry. Biophysical Journal 65, 1272-1282.

Bocquet, L., Charlaix, E., 2010. Nanofluidics, from bulk to interfaces. Chemical Society Reviers 39, 1073-1095.

Brown, M. J., Loew, L. M., 1994. Electric field-directed fibroblast locomotion involves cell surface molecular reorganization and is calcium independent. Journal of Cell Biology 127, 117-128.

Bystriansky, J. S., Kaplan, J. H., 2007. Sodium pump localization in epithelia. Journal of Bioenergetics and Biomembranes 39, 373-378.

Cao, L., McCaig, C. D., Scott, R. H., Zhao, S., Milne, G., Clevers, H., Zhao, M., Pu, J., 2014. Polarizing intestinal epithelial cells electrically through Ror2. Journal of Cell Science 127, 3233-3239.

Chen, Y., Azad, M. B., Gibson, S. B., 2010. Methods for detecting autophagy and determining autophagy-induced cell death. Canadian Journal of Physiology and Pharmacology 88, 285-295.

Chernyavsky, A. I., Arredondo, J., Karlsson, E., Wessler, I., Grando, S. A., 2005. The Ras/Raf-1/MEK1/ERK signaling pathway coupled to integrin expression mediates cholinergic regulation of keratinocyte directional migration. Journal of Biological Chemistry 280, 39220-39228.

Chizmadzhev, Y. A., Indenbom, A. V., Kuzmin, P. I., Galichenko, S. V., Weaver, J. C., Potts, R. O., 1998. Electrical properties of skin at moderate voltages: contribution of appendageal macropores. Biophysical Journal 74, 843-856.

Cohen, D. J., Nelson, W. J., Maharbiz, M. M., 2014. Galvanotactic control of collective cell migration in epithelial monolayers. Nature Materials 13, 409-417.

Cummings, R. D., Soderquist, A. M., Carpenter, G., 1985. The oligosaccharide moieties of the epidermal growth factor receptor in A-431 cells. Journal of Biological Chemistry 260, 11944-11952.

Deen, W. M., 1987. Hindered transport of large molecules in liquid-filled pores. AIChE Journal 33, 1409-1425.

Denet, A.-R., Vanbever, R., Préat, V., 2004. Skin electroporation for transdermal and topical delivery. Advanced Drug Delivery Reviews 56, 659-674.

Di Rienzo, C., Piazza, V., Gratton, E., Beltram, F., Cardarelli, F., 2014. Probing short-range protein Brownian motion in the cytoplasm of living cells. Nature Communications 5, 5891.

Djamgoz, M. B. A., Mycielska, M., Madeja, Z., Fraser, S. P., Kohorada, W., 2001. Directional movement of rat prostate cancer cells in direct-current electric field: involvement of voltage-gated Na+ channel activity. Journal of Cell Science 114, 2697-2705.

Dorh, N., Zhu, S., Dhungana, K. B., Pati, R., Luo, F.-T., Liu, H., Tiwari, A., 2015. BODIPY-based fluorescent probes for sensing protein surface-hydrophobicity. Scientific Reports 5, 18337.

Elmore, S., 2007. Apoptosis: A review of programmed cell death. Toxicologic Pathology 35, 495-516.

Fang, K. S., Farboud, B., Nuccitelli, R., Isseroff, R. R., 1998. Migration of human keratinocytes in electric fields requires growth factors and extracellular calcium. The Journal of Investigative Biology 111, 751-756.

Fang, K. S., Ionides, E., Oster, G., Niccitelli, R., Isseroff, R. R., 1999. Epidermal growth factor receptor relocalization and kinase activity are necessary for directional migration of keratinocytes in DC electric fields. Journal of Cell Science 112, 1967-1978.

Faraji, A. H., Cui, J. J., Guy, Y., Li, L., Weber, S. G., 2011. Synthesis and characterization of a hydrogel with controllable electroosmosis: A potential brain tissue surrogate for electrokinetic transport. Langmuir 27, 13635-13642.

Fox, R. W., McDonald, A. T., 1992. Introduction to Fluid Mechanics. John Wiley & Sons Inc., New York.

Frick, M., Schmidt, K., Nichols, B. J., 2007. Modulation of lateral diffusion in the plasma membrane by protein density. Current Biology 17, 462-467.

Frykberg, R. G., Banks, J., 2015. Challenges in the treatment of chronic wounds. Advances in Wound Care 4, 560-582.

Funk, R. H. W., 2015. Endogenous electric fields as guiding cue for cell migration. Frontiers in Physiology 6:143.

Gao, R., Zhao, S., Jiang, X., Sun, Y., Zhao, S., Gao, J., Borleis, J., Willard, S., Tang, M., Cai, H., Kamimura, Y., Huang, Y., Jiang, J., Huang, Z., Mogilner, A., Pan, T., Devreotes, P. N.,

Zhao, M., 2015. A large scale screen reveals genes that mediate electrotaxis in Dictyostelium discoideum. Science Signaling 8, ra50.

Garcia, A. M., Frank, E. H., Grimshaw, P. E., Grodzinsky, A. J., 1996. Contributions of fluid convection and electrical migration to transport in cartilage: relevance to loading. Archives of Biochemistry and Biophysics 333, 317-325.

Garcia, A. M., Szasz, N., Trippel, S. B., Morales, T. I., Grodzinsky, A. J., Frank, E. H., 2003. Transport and binding of insulin-like growth factor I through articular cartilage. Archives of Biochemistry and Biophysics 415, 69-79.

Gardner, S. E., Frantz, R. A., Schmidt, F. L., 1999. Effect of electrical stimulation on chronic wound healing: a meta-analysis. Wound Repair and Regeneration 7, 495-503.

Giugni, T. D., Braslau, D. L., Haigler, H. T., 1987. Electric field induced redistribution and postfield relaxation of epidermal growth factor receptors on A431 cells. Journal of Cell Biology 104, 1291-1297.

Goins, B., Masserini, M., Barisas, B. G., Freire, E., 1986. Lateral diffusion of ganglioside G_{M1} in phospholipid bilayer membranes. Biophysical Journal 49, 849-856.

Gomes, R. C., Guirro, E. C., Goncalves, A. C., Junior, J. A. F., Junior, L. O. M., Guirro, R. R., 2018. High-voltage electric stimulation of the donor site of skin grafts accelerates the healing process. A randomized blinded clinical trial. Burns 44, 636-645.

Gosak, M., Stožer, A., Markovič, R., Dolenšek, J., Perc, M., Rupnik, M. S., Marhl, M., 2017. Critical and Supercritical Spatiotemporal Calcium Dynamics in Beta Cells. Frontiers in Physiology 8, doi:10.3389/fphys.2017.01106.

Graham, D. M., Huang, L., Robinson, K. R., Messerli, M. A., 2013. Epidermal keratinocyte polarity and motility require Ca^{2+} influx through TRPV1. Journal of Cell Science 126, 4602-4613.

Grilo, A. L., Mantalaris, A., 2019. Apoptosis: A mammalian cell bioprocessing perspective. Biotechnology Advances 37, 459-475.

Grimshaw, P. E., Grodzinsky, A. J., Yarmush, M. L., Yarmush, D. M., 1989. Dynamic membranes for protein transport: chemical and electrical control. Chemical Engineering Science 44, 827-840.

Grossman, P. D., 1992. Factors affecting the performance of capillary electrophoresis separations: joule heating, electroosmosis and zone dispersion. In: Grossman, P. D., Colburn, J. C., Eds.), Capillary Electrophoresis Theory and Practice. Academic Press Inc., San Diego, pp. 3-43.

Grossman, P. D., Soane, D. S., 1991. Experimental and theoretical studies of DNA separations by capillary electrophoresis in entangled polymer solutions. Biopolymers 31, 1221-1228.

Groves, J. T., Boxer, S. G., 1995. Electric field-induced concentration gradients in planar supported bilayers. Biophysical Journal 69, 1972-1975.

Guigas, G., Weiss, M., 2015. Membrane protein mobility depends on the length of extra-membrane domains and on the protein concentration. Soft Matter 11, 33-37.

Guigni, T., Braslau, D. L., Haigler, H. T., 1987. Electric field-induced redistribution and postfield relaxation of epidermal growth factor receptors on A431 cells. The Journal of Cell Biology 104, 1291-1297.

Guo, L., Xu, C., Li, D., Zheng, X., Tang, J., Bu, J., Sun, H., Yang, Z., Sun, W., Yu, X., 2015. Calcium ion flow permeates cells through SOCs to promote cathode-directed galvanotaxis. PloS One 10, e0139865.

Hamsher, A. E., Xu, H., Guy, Y., Sandberg, M., Weber, S. G., 2010. Minimizing tissue damage in electroosmotic sampling. Analytical Chemistry 82, 6370-6376.

Han, X., Cheetham, M. R., Sheikh, K., Olmsted, P. D., Bushby, R. J., Evans, S. D., 2009. Manipulation and charge determination of proteins in photopatterned solid supported bilayers. Integrative Biology 1, 205-211.

Han, Y., Liu, X.-M., Liu, H., Li, S.-C., Wu, B.-C., Ye, L.-L., Wang, Q.-W., Chen, Z.-L., 2006. Cultivation of recombinant Chinese hamster ovary cells grown as suspended aggregates in stirred vessels. Journal of Bioscience and Bioengeineering 102, 430-435.

Hanukoglu, I., Hanukoglu, A., 2016. Epithelial sodium channel (ENaC) family: Phylogeny, structure-function, tissue distribution, and associated inherited diseases. Gene 579, 95-132.

Hart, F. X., Laird, M., Riding, A., Pullar, C. E., 2013. Keratinoctye galvanotaxis in combined DC and AC electric fields supports an electromechanical transduction sensing mechanism. Bioelectromagnetics 34, 85-94.

Hebenstreit, D., Fang, M., Gu, M., Charoensawan, V., van Oudenaarden, A., Teichmann, S. A., 2011. RNA sequencing reveals two major classes of gene expression levels in metazoan cells. Molecular Systems Biology 7, 497.

Hinkle, L., McCaig, C. D., Robinson, K. R., 1981. The direction of growth of differentiating neurones and myoblasts from frog embryos in an applied electric field. Journal of Physiology 314, 121-135.

Hölzer, A., Sommerfeld, M., 2008. New simple correlation formula for the drag coefficient of non-spherical particles. Powder Technology 814, 362-365.

Hotary, K. B., Robinson, K. R., 1994. Endogenous electrical currents and voltage gradients in *Xenopus* embryos and the consequences of their disruption. Developmental Biology 166, 789-800.

Howe, K., Clark, M. D., Torroja, C. F., Torrance, J., Berthelot, C., Maffato, M., Collins, J. E., Humphray, S., McLaren, K., Matthews, L., McLaren, S., Sealy, I., Caccamo, M., 2013. The zebrafish reference genome sequence and its relationship to the human genome. Nature 496, 498-503.

Huang, L., Cormie, P., Messerli, M. A., Robinson, K. R., 2009a. The involvement of Ca^{2+} and integrins in directional responses of zebrafish keratocytes to electric fields. Journal of Cellular Physiology 219, 162-172.

Huang, L., Cormie, P., Messerli, M. A., Robinson, K. R., 2009b. The involvement of Ca^{2+} and integrins in directional repsonses of zebrafish keratocytes to electric fields. Journal of Cellular Physiology 219, 162-172.

Huang, Y.-J., Hoffman, G., Wheeler, B., Schiapparelli, P., Quinones-Hinojosa, A., Searson, P., 2016. Cellular microenvironment modulates the galvanotaxis of brain tumor initiating cells. Scientific Reports 6, 21583.

Huang, Y.-J., Schiapparelli, P., Kozielski, K., Green, J., Lavell, E., Guerrero-Cazares, H., Quinones-Hinojosa, A., Searson, P., 2017. Electrophoresis of cell membrane heparan sulfate regulates galvanotaxis in glial cells. Journal of Cell Science 130, 2459-2467.

Hughey, R. P., Mueller, G. M., Bruns, J. B., Kinlough, C. L., Poland, P. A., Harkleroad, K. L., Carattino, M. D., Kleyman, T. R., 2003. Maturation of the epithelial Na^{+} channel involves proteolytic processing of the α- and γ-subunits. Journal of Biological Chemistry 278, 37073-37082.

Imperiali, B., O'Connor, S. E., 1999. Effect of N-linked glycosylation on glycopeptide and glycoprotein structure. Current Opinion in Chemical Biology 3, 643-649.

Isseroff, R. R., Dahle, S. E., 2012. Electrical stimulation therapy and wound healing: Where are we now? Advances in Wound Care 1, 238-243.

Jaffe, L. F., Poo, M.-M., 1979. Neurites grow faster towards the cathode than the anode in a steady field. Journal of Experimental Zoology 209, 115-128.

Jee, A.-Y., Curtis-Fisk, J. L., Granick, S., 2014. Nanoparticle diffusion in methylcellulose thermoreversible association polymer. Macromolecules 47, 5793-5797.

Johnson, E. M., Berk, D. A., Jain, R. K., Deen, W. M., 1996. Hindered diffusion in agarose gels: test of effective medium model. Biophysical Journal 70, 1017-1026.

Johnson, H. E., King, S. J., Asokan, S. B., Rotty, J. D., Bear, J. E., Haugh, J. M., 2015. F-actin bundles direct the initiation and orientation of lamellipodia through adhesion-based signaling. Journal of Cell Biology 208, 443-455.

Kao, H.-J., Huang, C.-H., Bretaña, N. A., Lu, C.-T., Huang, K.-Y., Weng, S.-L., Lee, T.-Y., 2015. A two-layered machine learning method to identify protein O-GlcNAcylation sites with O-GlcNAc transferase substrate motifs. BMC Bioinformatics 16, S10.

Keary, C. M., 2001. Characterization of METHOCEL cellulose ethers by aqueous SEC with multiple detectors. Carbohydrate Polymers 45, 293-303.

Kihara, T., Ito, J., Miyake, J., 2013. Measurement of biomolecular diffusion in extracellular matrix condensed by fibroblasts using fluorescence correlation spectroscopy. PLOS ONE 8, e82382.

Kim, Y., Morris, M. D., 1994. Pulse field capillary electrophoresis of multikilobase length nucleic acids in dilute methyl cellulose solutions. Analytical Chemistry 66, 3081-3085.

Kinraide, T. B., Yermiyahu, U., Rytwo, G., 1998. Computation of surface electrical potentials of plant cell membranes. Plant Physiology 118, 505-512.

Klausen, M. S., Jespersen, M. C., Nielsen, H., Jensen, K. K., Jurtz, V. I., Soenderby, C. K., Sommer, M. O. A., Winther, O., Nielsen, M., Petersen, B., Marcatili, P., 2018. NetSurfP-2.0: improved prediction of protein structural features by integrated deep learning. bioRxiV, doi:https://doi.org/10.1101/311209

Kloth, L. C., 2014. Electrical stimulation technologies for wound healing. Advances in Wound Care 3, 81-90.

Kloth, L. C., Zhao, M., 2010. Endogenous and exogenous electrical fields for wound healing. In: McCulloch, J. M., Kloth, L. C., Eds.), Wound healing: Evidence-based management, Vol. F.A. Davis, Philadelphia, pp. 450-513.

Kobayashi, K., Huang, C.-i., Lodge, T. P., 1999. Thermoreversible gelation of aqueous methylcelluose solutions. Macromolecules 32, 7070-7077.

Kobylkevich, B. M., Sarkar, A., Carlberg, B. R., Huang, L., Ranjit, S., Graham, D. M., Messerli, M. A., 2018. Reversing the direction of galvanotaxis with controlled increases in boundary layer viscosity. Physical biology 15, 036005.

Kozlowski, L. P., 2016. IPC- Isoelectric point calculator. Biology Direct 11, 55, doi:10.1186/s13062-016-0159-9.

Krajewski, A., Malavolti, R., Piancastelli, A., 1996. Albumin adhesion on some biological and non-biological glasses and connection with their Z-potentials. Biomaterials 17, 53-60.

Kroemer, G., Levine, B., 2008. Autophagic cell death: the story of a misnomer. Nature Reviews Molecular Cell Biology 9, 1004-1010.

Kuang, C., Yang, F., Zhao, W., Wang, G., 2009. Study of the rise time in electroosmotic flow within a microcapillary. Analytical Chemistry 81, 6590-6595.

Kucerka, N., Tristram-Nagle, S., Nagle, J. F., 2006. Closer look at structure of fully hydrated fluid phase DPPC bilayers. Biophysical Journal 90, L83-L85.

Lawrence, M. S., Phillips, K. J., Liu, D. R., 2007. Supercharging proteins can impart unusual resilience. Journal of the American Chemical Society 129, 10110-10112.

Le Bras, S., Le Borgne, R., 2014. Epithelial cell division - multiplying without losing touch. Journal of Cell Science 127, 5127-5137.

Leggio, C., Galantini, L., Pavel, N. V., 2008. About the albumin structure in solution: cigar Expanded form versus heart Normal shape. Physical Chemistry Chemical Physics 10, 6741-6750.

Levin, M., Stevenson, C. G., 2012. Regulation of cell behavior and tissue patterning by bioelectrical signals: Challenges and opportunities for biomedical engineering. Annual Review of Biomedical Engineering 14, 295-323.

Li, Y., Gu, Y., Wang, H., Liu, Z., Song, B., Yin, T., 2018. Electric pulses can influence galvanotaxis of *Dictyostelium discoideum*. BioMed Research International 2018, 1-15.

Lin, B.-j., Tsao, S.-h., Chen, A., Hu, S.-K., Chao, L., Chao, P.-h. G., 2017. Lipid rafts sense and direct electric field-inducded migration. Proceedings of the National Academy of Sciences of the United States of America 114, 8568-8573.

Lindstrom, J., Merlie, J., Yogeeswaran, G., 1979. Biochemical properties of acetylcholine receptor subunits from *Torpedo californica*. Biochemistry 18, 4465-4470.

Liu, C., Monson, C. F., Yang, T., Pace, H., Cremer, P. S., 2011. Protein separation by electrophoretic-electroosmotic focusing on supported lipid bilayers. Analytical Chemistry (Washington) 83, 7876-7880.

Lopez-Duarte, I., Vu, T. T., Izquierdo, A., Bull, J. A., Kuimova, M. K., 2013. A molecular rotor for measuring viscosity in plasma membranes of live cells. Chemical Communications (1) 50, 5282-5284.

Lovett, M., Lee, K., Edwards, A., Kaplan, D. L., 2009. Vascularization strategies for tissue engineering. Tissue Engineering Part B, Reviews 15, 353-370.

Ma, X., Ahmed, S., Wohland, T., 2011. EGFR activation monitored by SW-FCCS in live cells. Frontiers in Bioscience E3, 22-32.

Mattern, K. J., Nakornchai, C., Deen, W. M., 2008. Darcy permeability of agarose-glycosaminoglycan gels analyzed using fiber-mixture and donnan models. Biophysical Journal 95, 648-656.

Maul, G. G., Deaven, L., 1977. Quantitative determination of nuclear pore complexes in cycling cells with differing DNA content. Journal of Cell Biology 73, 748-760.

Mazzochi, C., Benos, D. J., Smith, P. R., 2006. Interaction of epithelial ion channels with the actin-based cytoskeleton. American Journal of Physiology: Renal Physiology 291, F1113-F1122.

McCaig, C. D., 1989. On the mechanism of nerve galvanotropism. Biological Bulletin 176S, 136-139.

McCaig, C. D., Song, B., Rajnicek, A. M., 2009. Electrical dimensions in cell science. Journal of Cell Science 122, 4267-4276.

McCaig, C. D., Rajnicek, A. M., Song, B., Zhao, M., 2005. Controlling cell behavior electrically: Current views and future potential. Physiological Reviews 85, 943-978.

McCarty, W. J., Johnson, M., 2007. The hydraulic conductivity of Matrigel™. Biorheology 44, 303-317.

McCarty, W. J., Chimento, M. F., Curcio, C. A., Johnson, M., 2008. Effects of particulates and lipids on the hydraulic conductivity of Matrigel. Journal of Applied Physiology 105, 621-628.

McLaughlin, S. M., Poo, M.-M., 1981. The role of electro-osmosis in the electric-field-induced movement of charged macromolecules on the surfaces of cells. Biophysical Journal 34, 85-93.

Mehrishi, J. N., Johann, B., 2002. Electrophoresis of cells and the biological relevance of surface charge. Electrophoresis 23, 1984-1994.

Meltzer, H., Silberberg, A., 1988. Adsorption of collagen, serum albumin, and fibronectin to glass and to each other. Journal of Colloid and Interface Science 126, 292-303.

Messerli, M. A., Graham, D. M., 2011. Extracellular electrical fields direct wound healing and regeneration. Biological Bulletin 221, 79-92.

Minc, N., Chang, F., 2010. Electrical control of cell polarization in the fission yeast *Schizosaccharomyces pombe*. Current Biology 20, 710-716.

Miura, T., Tanaka, R., 2009. *In vitro* vasculogenesis models revisited - measurement of VEGF diffusion in Matrigel. Mathematical Modelling of Natural Phenomena 4, 118-130.

Miyagi, H., Maruyama, I. N., 2010. Analysis of ligand-receptor interaction on the surface of living cells by fluorescence correlation spectroscopy. The Open Spectroscopy Journal 4, 28-31.

Mudunuri, U., Che, A., Yi, M., Stephens, R. M., 2009. bioDBnet: the biological database network. Bioinformatics 25, 555-556.

Munakata, H., Schmid, K., 1982. The α and β subunits of lamb kidney Na,K-ATPase are both glycoproteins. Biochemical and Biophysical Research Communications 107, 229-231.

Murata, Y., Iwasaki, H., Sasaki, M., Inaba, K., Okamura, Y., 2005. Phosphoinositide phosphatase activity coupled to an intrinsic voltage sensor. Nature 435, 1239-1243.

Nakajima, K.-i., Zhu, K. Y., Sun, Y.-H., Hegyi, B., Zeng, Q., Murphy, C. J., Small, J. V., Chen-Izu, Y., Izumiya, Y., Penninger, J. M., Zhao, M., 2015. KCNJ15/Kir4.2 couples with polyamines to sense weak extracellular electric fields in galvanotaxis. Nature Communications 6, 8532.

Nelson, D. L., Cox, M. M., 2008. Lehninger Principles of Biochemistry 5th Edition. W.H. Freeman.

Ng, C. P., Swartz, M. A., 2003. Fibroblast alignment under interstitial fluid flow using a novel 3-D tissue culture model. Americal Journal of Physiology-Heart and Circulatory Physiology 284, H1771-H1777.

Ng, C. P., Swartz, M. A., 2006. Mechanisms of interstital flow-induced remodeling of fibroblast-collagen cultures. Annals of Biomedical Engineering 34, 446-454.

Nishimura, K. Y., Isseroff, R. R., Nuccitelli, R., 1996. Human keratinocytes migrate to the negative pole in direct current electrical fields comparable to those measured in mammalian wounds. Journal of Cell Science 109, 199-207.

Noor, N., Shapira, A., Edri, R., Gal, I., Wertheim, L., Dvir, T., 2019. 3D printing of personalized thick and perfusable cardiac patches and hearts. Advanced Science 6, 1900344.

Novosel, E. C., Kleinhans, C., Kluger, P. J., 2011. Vascularization is the key challenge in tissue engineering. Advanced Drug Delivery Reviews 63, 300-311.

Nuccitelli, R., 2004. A role for endogenous electric fields in wound healing. In: Schatten, E. D., (Ed.), Current Topics in Developmental Biology, Vol. 58. Academic Press, San Diego, CA, pp. 1-26.

Nuccitelli, R., Smart, T., 1989. Calcium levels strongly influence neural crest cell galvanotaxis. Biological Bulletin 176, 130-135.

Ohshima, H., 1995. Electrophoretic mobility of soft particles. Colloids and Surfaces A: Physiochemical and Engineering Aspects 103, 249-255.

Omori, K., Takemura, S., Omori, K., Mega, T., Tashiro, Y., 1983. Isolation of the α and β subunits of canine (Na^+,K^+)ATPase. Journal of Biochemistry (Tokyo) 94, 1857-1866.

Orida, N., Poo, M.-M., 1978. Electrophoretic movement and localisation of acetycholine receptors in the embryonic muscle cell membrane. Nature 275, 31-35.

Ou, Y., Wu, J., Sandberg, M., Weber, S. G., 2014. Electroosmotic perfusion of tissue: sampling the extracellular space and quantitative assessment of membrane-bound enzyme activity in organotypic hippocampal slice cultures. Analytical and Bioanalytical Chemistry 406, 6455-6468.

Pak, S. C., Hung, S. M., Bridges, M. W., Sleigh, M. J., Gray, P. P., 1996. Super-CHO-A cell line capable of autocrine growth under fully defined protein-free conditions. Cytotechnology 22, 139-146.

Palmer, A. M., Messerli, M. A., Robinson, K. R., 2000. Neuronal galvanotropism is independent of external Ca^{2+} entry or internal Ca^{2+} gradients. Journal of Neurobiology 45, 30-38.

Park, J. Y., White, J. B., Walker, N., Kuo, C.-H., Cha, W., Meyerhoff, M. E., Takayama, S., 2011. Responses of endothelial cells to extremely slow flows. Biomicrofluidics 5, 022211.

Patel, N. B., Poo, M.-M., 1982. Orientation of neurite growth by extracellular electric fields. Journal of Neuroscience (1) 2, 483-496.

Patel, N. B., Poo, M.-M., 1984. Perturbation of the direction of neurite growth by pulsed and focal electric fields. Journal of Neuroscience (1) 4, 2939-2947.

Paulick, M. G., Forstner, M. B., Groves, J. T., Bertozzi, C. R., 2007. A chemical approach to unraveling the biological function of the glycosylphosphatidylinositol anchor. Proceedings of the National Academy of Sciences of the United States of America 104, 20332-20337.

Peters, R., Cherry, R. J., 1982. Lateral and rotational diffusion of bacteriorhodopsin in lipid bilayers: Experimental test of the Saffman-Delbrück equations. Proceedings of the National Academy of Sciences of the United States of America 79, 4317-4321.

Petrasek, Z., Schwille, P., 2008. Precise measurement of diffusion coefficients using scanning fluorescence correlation spectroscopy. Biophysical Journal 94, 1437-1448.

Pierleoni, A., Martelli, P. L., Casadio, R., 2008. PredGPI: a GPI-anchor predictor. BMC Bioinformatics 9, 392, doi:10.1186/1471-2105-9-392.

Politis, M. J., Zanakis, M. F., Miller, J. E., 1989. Enhanced survival of full-thickness skin grafts following the application of DC electrical fields. Plastic and Reconstructive Surgery 84, 267-272.

Poo, M.-M., 1981. *In situ* electrophoresis of membrane components. Annual Review of Biophysics and Bioengineering 10, 245-276.

Poo, M.-M., Cone, R. A., 1974. Lateral diffusion of rhodopsin in the photoreceptor membrane. Nature (London) 247, 438-441.

Poo, M.-M., Robinson, K. R., 1977. Electrophoresis of concanavalin A receptors along embryonic muscle cell membrane. Nature 265, 602-605.

Poo, M.-M., Lam, J. W., Orida, N., Chao, A. W., 1979. Electrophoresis and diffusion in the plane of the cell membrane. Biophysical Journal 26, 1-22.

Pu, J., Zhao, M., 2005. Golgi polarization in a strong electric field. Journal of Cell Science 118, 1117-1128.

Pu, J., Cao, L., McCaig, C. D., 2015. Physiological extracellular electrical signals guide and orient the polarity of gut epithelial cells. Tissue Barriers 3, e1037417.

Pullar, C. E., Isseroff, R. R., 2005. Cyclic AMP mediates keratinocyte directional migration in an electric field. Journal of Cell Science 118, 2023-2034.

Rajnicek, A. M., Robinson, K. R., McCaig, C. D., 1998. The direction of neurite growth in a weak DC electric field depends on the substratum: contributions of adhesivity and net surface charge. Developmental Biology 203, 412-423.

Rasband, W. S., 1997-2012. US National Institutes of Health, Bethesda, Maryland, USA, http://imagej.nih.gov/ij/.

Rasband, W. S., 1997-2018. ImageJ. [Online]. U.S. National Institutes of Health, Bethesda, MD, Available: https://imagej.nih.gov/ij/ [2018, Sept. 1].

Rasmussen, B., Davis, R., Thomas, J., Reddy, P., 1998. Isolation, characterization and recombinant protein expression in Veggie-CHO: A serum-free CHO host cell line. Cytotechnology 28, 31-42.

Reemann, P., Reimann, E., Ilmjärv, S., Porosaar, O., Silm, H., Jaks, V., Vasar, E., Kingo, K., Kõks, S., 2014. Melanocytes in the skin–comparative whole transcriptome analysis of main skin cell types. PloS One 9, e115717.

Riding, A., Pullar, C. E., 2016. ATP release and P2Y receptor signaling are essential for keratinocyte galvanotaxis. Journal of Cellular Physiology 213, 181-191.

Robinson, K. R., 1985. The responses of cells to electrical fields: A review. Journal of Cell Biology 101, 2023-2027.

Robinson, K. R., Messerli, M. A., 2003a. Left/right, up/down: the role of edogenous electrical fields as directional signals in development, repair and invasion. BioEssays 25, 759-766.

Robinson, K. R., Messerli, M. A., 2003b. Left/right, up/down: the role of endogenous electrical fields as directional signals in development, repair and invasion. BioEssays 25, 759-766.

Rupert, A. E., Ou, Y., Sandberg, M., Weber, S. G., 2013a. Assessment of tissue viability following electroosmotic push-pull perfusion from organotypic hippocampal slice culture. ACS Chemical Neuroscience 4, 849-857.

Rupert, A. E., Ou, Y., Sandberg, M., Weber, S. G., 2013b. Electroosmotic push-pull perfusion: Description and application to qualitative analysis of the hydrolysis of exogenous galanin in organotypic hippocampal slice cultures. ACS Chemical Neuroscience 4, 838-848.

Saffman, P. G., Delbrück, M., 1975. Brownian motion in biological membranes. Proceedings of the National Academy of Sciences of the United States of America 72, 3111-3113.

Saha, S., Lee, I.-H., Polley, A., Groves, J. T., Rao, M., Mayor, S., 2015. Diffusion of GPI-anchored proteins is influenced by the activity of dynamic cortical actin. Molecular Biology of the Cell 26, 4033-4045.

Saltukoglu, D., Gruewald, J., Strohmeyer, N., Bensch, R., Ulbrich, M. H., Ronneberger, O., Simon, M., 2015. Spontaneous and electric field-controlled front-rear polarization of human keratinocytes. Molecular Biology of the Cell 26, 4373-4386.

Sarkar, A., Kobylkevich, B. M., Graham, D. M., Messerli, M. A., 2019. Electromigration of cell surface macromolecules in DC electric fields during cell polarization and galvanotaxis. Journal of Theoretical Biology 478, 58-73.

Sarkar, N., 1979. Thermal gelation properties of methyl and hydroxypropyl methylcellulose. Journal of Applied Polymer Science 24, 1073-1087.

Sarrazin, S., Lamanna, W. C., Esko, J. D., 2011. Heparan Sulfate Proteoglycans. Cold Spring Harbor Perspectives in Biology a004952.

Sasaki, M., Takagi, M., Okamura, Y., 2006. A voltage sensor-domain protein is a voltage-gated proton channel. Science 312, 589-592.

Sato, M. J., Kuwayama, H., van Egmond, W. N., Takayama, A. L. K., Takagi, H., van Haastert, P. J. M., Tanagida, T., Ueda, M., 2009a. Switching direction in electric-signal-induced cell migration by cyclic guanosine monophosphate and phosphatidylinositol signaling. Proceedings of the National Academy of Sciences U.S.A. 106, 6667-6672.

Sato, M. J., Kuwayama, H., van Egmond, W. N., Takayama, A. L. K., Takagi, H., van Haastert, P. J. M., Tanagida, T., Ueda, M., 2009b. Switching direction in electric-signal-induced cell migration by cyclic guanosine monophosphate and phosphatidylinositol signaling. Proceedings of the National Academy of Sciences of the United States of America 106, 6667-6672.

Schneider, F., Waithe, D., Lagerholm, B. C., Shrestha, D., Sezgin, E., Eggeling, C., Fritzsche, M., 2018. Statistical Analysis of Scanning Fluorescence Correlation Spectroscopy Data Differentiates Free from Hindered Diffusion. ACS Nano 12, 8540-8546, doi:10.1021/acsnano.8b04080.

Shaner, N. C., Campbell, R. E., Steinbach, P. A., Giepmans, B. N. G., Palmer, A. E., Tsien, R. Y., 2004. Improved monomeric red, orange and yellow fluorescent proteins derived from Discosoma sp. red fluorescent protein. Nature Biotechnology 22, 1567-1572.

Sherin, P. S., Lopez-Duarte, I., Dent, M. R., Kubankova, M., Vysniauskas, A., Bull, J. A., Reshetnikova, E. S., Klymchenko, A. S., Tsentalovich, Y. P., Kuimova, M. K., 2017. Visualising the membrane viscosity of porcine eye lens cells using molecular rotors. Chemical Science (Royal Society of Chemistry: 2010) 8, 3523-3528.

Shi, Z.-D., Ji, X.-Y., Qazi, H., Tarbell, J. M., 2009. Interstital flow promotes vascular fibroblast, myofibroblast, and smooth muscle cell motility in 3-D collagen I via upregulation of MMP-1. American Journal of Physiology-Heart and Circulatory Physiology 297, H1225-H1234.

Siemionow, M., Arslan, E., 2004. Ischemia/Reperfusion injury: A review in relation to free tissue transfers. Microsurgery 24, 468-475.

Sigma-Aldrich, 1997. Product Information: Methyl Cellulose.

Slivinsky, G. G., Hymer, W. C., Bauer, J., Morrison, D. R., 1997. Cellular electrophoretic mobility data: A first approach to a database. Electrophoresis 18, 1109-1119.

Soderman, O., Jonsson, B., 1996. Electro-osmosis: Velocity profiles in different geometries with both temporal and spatial resolution. Journal of Chemical Physics 105, 10300-10311.

Steentoft, C., Vakhrushev, S. Y., Joshi, H. J., Kong, Y., Vester-Christensen, M. B., Katrine, T., Schjoldager, B., Lavrsen, K., Dabelsteen, S., Pedersen, N. B., 2013. Precision mapping of the human O-GalNAc glycoproteome through SimpleCell technology. The EMBO Journal 32, 1478-1488.

Stollberg, J., Fraser, S. E., 1988. Acetylcholine receptors and concanavalin-A-binding sites on cultured Xenopus muscle cells - electrophoresis, diffusion and aggregation. Journal of Cell Biology 107, 1397-1408.

Stollberg, J., Fraser, S. E., 1990. Local accumulation of acetylcholine receptors is neither necessary nor sufficient to induce cluster formation. Journal of Neuroscience (1) 10, 247-255.

Stump, R. F., Robinson, K. R., 1983. Xenopus neural crest cell migration in an applied electrical field. Journal of Cell Biology 97, 1226-1233.

Su, T., Huang, K., Mathews, K. G., Scharf, V. F., Hu, S., Li, Z., Frame, B. N., Cores, J., Dinh, P.-U., Daniele, M. A., Ligler, F. S., Cheng, K., 2020. Cardiac stromal cell patch integrated with engineered microvessels improves recovery from myocardial infarction in rats and pigs. ACS Biomaterials Science and Engineering 6, 6309-6320.

Sun, Y., Do, H., Gao, J., Zhao, R., Zhao, M., Mogilner, A., 2013. Keratocyte fragments and cells utilize competing pathways to move in opposite directions in an electric field. Current Biology 23, 569-574.

Swartz, M. A., Fleury, M. E., 2007. Interstitial flow and its effects in soft tissues. Annual Review of Biomedical Engineering 9, 229-256.

Tagami, H., Ohi, M., Iwatsuki, K., Kanamaru, Y., Yamada, M., Ichijo, B., 1980. Evaluation of the skin surface hydration in vivo by electrical measurement. Journal of Investigative Dermatology 75, 500-507.

Tank, D. W., Fredericks, W. J., Barak, L. S., Webb, W. W., 1985. Electric-field induced redistribution and post-field relaxation of low-density lipoprotein receptors on cultured human fibroblasts. Journal of Cell Biology 101, 148-157.

Thompson, D. B., Cronican, J. J., Liu, D. R., 2012. Engineering and identifying supercharged proteins for macromolecule delivery into mammalian cells. Methods in Enzymology 503, 293-319.

Trollinger, D. R., Isseroff, R. R., Nuccitelli, R., 2002. Calcium channel blockers inhibit galvanotaxis in human keratinocytes. Journal of Cellular Physiology 193, 1-9.

Tsirigos, K. D., Peters, C., Shu, N., Käll, L., Elofsson, A., 2015. The TOPCONS web server for consensus prediction of membrane protein topology and signal peptides. Nucleic Acids Research 43, W401-W407.

Tung, L., Sliz, N., Mulligan, M. R., 1991. Influence of electrical axis of stimulation on excitation of cardiac muscle cells. Circulation Research 69, 722-730.

Van den Steen, P., Rudd, P. M., Dwek, R. A., Opdenakker, G., 1998. Concepts and principles of O-linked glycosylation. Critical Reviews in Biochemistry and Molecular Biology 33, 151-208.

Wagner, G. P., Kin, K., Lynch, V. J., 2013. A model based criterion for gene expression calls using RNA-seq data. Theory in Biosciences 132, 159-164.

Walsh, G. M., Dewson, G., Wardlaw, A. J., Levi-Schaffer, F., Moqbel, R., 1998. A comparative study of different methods for the assessment of apoptosis and necrosis in human eosinophils. Journal of Immunological Methods 217, 153-163.

Wang, C., Rathore, K. S., Robinson, K. R., 1989. The responses of pollen to applied electrical fields. Developmental Biology 136, 405-410.

Weaver, J. C., Astumian, R. D., 1990. The response of living cells to very weak electric fields: The thermal noise limit. Science 247, 459-462.

WeiB, K., Neef, A., Van, Q., Kramer, S., Gregor, I., Enderlein, J., 2013. Quantifying the diffusion of membrane proteins and peptides in black lipid membranes with 2-focus fluorescence correlation spectroscopy. Biophysical Journal 105, 455-462.

Yahara, I., Edelman, G. M., 1975. Modulatioin of lymphocyte receptor mobility by locally bound concanavalin A. Proceeding of the National Academy of Sciences U.S.A. 72, 1579-1583.

Yan, X., Han, J., Zhang, Z., Wang, J., Cheng, Q., Gao, K., Ni, Y., Wang, Y., 2009. Lung cancer A549 cells migrate directionally in DC electric fields with polarized and activated EGFRs. Bioelectromagnetics 30, 29-35.

Yang, H.-y., Charles, R.-P., Hummler, E., Baines, D. L., Isseroff, R. R., 2013. The epithelial sodium channel mediates the directionality of galvanotaxis in human keratinocytes. Journal of Cell Science 126, 1942-1951.

Yu, C. S., Chen, Y. C., Lu, C. H., Hwang, J. K., 2006. Prediction of protein subcellular localization. Proteins: Structure, Function, and Bioinformatics 64, 643-651.

Zaman, E., Jalali, P., 2010. On hydraulic permeability of random packs of monodisperse spheres: direct flow simulations versus correlations. Physica A 389, 205-214.

Zaman, M. H., Trapani, L. M., Sieminski, A. L., MacKellar, D., Gong, H., Kamm, R. D., Wells, A., Lauffenburger, D. A., Matsudaira, P., 2006. Migration of tumor cells in 3D matrices is govered by matrix stiffness along with cell-matrix adhesion and proteolysis. Proceeding of the National Academy of Sciences U.S.A. 103, 10889-10894.

Zhang, F., Crise, B., Su, B., Hou, Y., Rose, J. K., Bothwell, A., Jacobson, K., 1991. Lateral diffusion of membrane-spanning and glycosylphosphatidylinositol-linked proteins: Toward establishing rules governing the lateral mobility of membrane proteins. Journal of Cell Biology 115, 75-84.

Zhao, M., 2009. Electrical fields in wound healing-An overriding signal that directs cell migration. Seminars in Cell & Developmental Biology 20, 674-682.

Zhao, M., Agius-Fernandez, A., Forrester, J. V., McCaig, C. D., 1996. Orientation and directed migration of cultured corneal epithelial cells in small electric fields are serum dependent. Journal of Cell Science 109, 1405-1414.

Zhao, M., Dick, A., Forrester, J. V., McCaig, C. D., 1999a. Electric field-directed cell motility involves up-regulated expression and asymmetric redistribution of the epidermal growth factor receptors and is enhanced by fibronectin and laminin. Molecular Biology of the Cell 10, 1259-1276.

Zhao, M., Dick, A., Forrester, J. V., McCaig, C. D., 1999b. Electric field-directed cell motility involves up-regulated expression and asymmetric redistribution of the epidermal growth factor receptors and is enhanced by fibronectin and laminin. Molecular Biology of the Cell 10, 1259-1276.

Zhao, M., Pu, J., Forrester, J. V., McCaig, C. D., 2002a. Membrane lipids, EGF receptors, and intracellular signals colocalize and are polarized in epithelial cells moving directionally in a physiological electric field. The FASEB Journal 16, 857-859.

Zhao, M., Jin, T., McCaig, C. D., Forrester, J. V., Devreotes, P. N., 2002b. Genetic analysis of the role of G protein-coupled receptor signaling in electrotaxis. Journal of Cell Biology 157, 921-927.

Zhao, M., Song, B., Pu, J., Wada, T., Reid, B., Tai, G., Wang, F., Guo, A., Walczysko, P., Gu, Y., Sasaki, T., Suzuki, A., Forrester, J. V., Bourne, H. R., Devreotes, P. N., McCaig, C. D., Penninger, J. M., 2006. Electrical signals control wound healing through phosphatidylinositol-3-OH kinase-γ and PTEN. Nature 442, 457-460.

Zhen, Y., Caprioli, R. M., Staros, J. V., 2003. Characterization of glycosylation sites of the epidermal growth factor receptor. Biochemistry 42, 5478-5492.

Zhu, K., Sun, Y., Miu, A., Yen, M., Liu, B., Zeng, Q., Mogilner, A., Zhao, M., 2015. cAMP and cGMP play an essential role in galvanotaxis of cell fragments. Journal of Cellular Physiology 231, 1291-1300.

Zielinska, D. F., Gnad, F., Wiśniewski, J. R., Mann, M., 2010. Precision mapping of an in vivo N-glycoproteome reveals rigid topological and sequence constraints. Cell 141, 897-907.